

AD\_\_\_\_\_

Award Number: W81XWH-06-1-0042

TITLE: Molecular Imaging of Ovarian Carcinoma Angiogenesis

PRINCIPAL INVESTIGATOR: Xiaoyuan Chen, Ph.D.

CONTRACTING ORGANIZATION: Stanford University  
Stanford, CA 94305

REPORT DATE: March 2007

TYPE OF REPORT: Annual

PREPARED FOR: U.S. Army Medical Research and Materiel Command  
Fort Detrick, Maryland 21702-5012

DISTRIBUTION STATEMENT: Approved for Public Release;  
Distribution Unlimited

The views, opinions and/or findings contained in this report are those of the author(s) and should not be construed as an official Department of the Army position, policy or decision unless so designated by other documentation.

# REPORT DOCUMENTATION PAGE

*Form Approved  
OMB No. 0704-0188*

Public reporting burden for this collection of information is estimated to average 1 hour per response, including the time for reviewing instructions, searching existing data sources, gathering and maintaining the data needed, and completing and reviewing this collection of information. Send comments regarding this burden estimate or any other aspect of this collection of information, including suggestions for reducing this burden to Department of Defense, Washington Headquarters Services, Directorate for Information Operations and Reports (0704-0188), 1215 Jefferson Davis Highway, Suite 1204, Arlington, VA 22202-4302. Respondents should be aware that notwithstanding any other provision of law, no person shall be subject to any penalty for failing to comply with a collection of information if it does not display a currently valid OMB control number. PLEASE DO NOT RETURN YOUR FORM TO THE ABOVE ADDRESS.

<b>1. REPORT DATE</b> 01-03-2007			<b>2. REPORT TYPE</b> Annual		<b>3. DATES COVERED</b> 1 Feb 2006 – 31 Jan 2007	
<b>4. TITLE AND SUBTITLE</b>  Molecular Imaging of Ovarian Carcinoma Angiogenesis			<b>5a. CONTRACT NUMBER</b>			
			<b>5b. GRANT NUMBER</b> W81XWH-06-1-0042			
			<b>5c. PROGRAM ELEMENT NUMBER</b>			
<b>6. AUTHOR(S)</b>  Xiaoyuan Chen, Ph.D.  Email: shawchen@stanford.edu			<b>5d. PROJECT NUMBER</b>			
			<b>5e. TASK NUMBER</b>			
			<b>5f. WORK UNIT NUMBER</b>			
<b>7. PERFORMING ORGANIZATION NAME(S) AND ADDRESS(ES)</b>  Stanford University Stanford, CA 94305			<b>8. PERFORMING ORGANIZATION REPORT NUMBER</b>			
			<b>10. SPONSOR/MONITOR'S ACRONYM(S)</b>			
<b>9. SPONSORING / MONITORING AGENCY NAME(S) AND ADDRESS(ES)</b> U.S. Army Medical Research and Materiel Command Fort Detrick, Maryland 21702-5012			<b>11. SPONSOR/MONITOR'S REPORT NUMBER(S)</b>			
			<b>12. DISTRIBUTION / AVAILABILITY STATEMENT</b> Approved for Public Release; Distribution Unlimited			
<b>13. SUPPLEMENTARY NOTES</b> Original contains colored plates: ALL DTIC reproductions will be in black and white.						
<b>14. ABSTRACT</b> This purpose of this proposal is to use high resolution microPET technology to image ovarian cancer integrin av $\beta$ 3 expression in vivo. Ovarian cancer is angiogenesis dependent. Integrin av $\beta$ 3, a key player in tumor angiogenesis and metastasis, has been identified as a target for diagnostic and therapeutic interventions for several highly proliferative and metastatic tumor types. The interaction between vitronectin and integrin av $\beta$ 3 is essential for ovarian cancer cell survival and invasion. The integrin expression has been identified as a marker of poor prognosis in advanced-stage ovarian cancer. Its role in ovarian cancer development and as treatment target is under-developed. Specific Aim 1: To develop and optimize 18F-labeled RGD peptides for ovarian carcinoma targeting. Specific Aim 2: To test 18F-RGD peptide tracers in ovarian carcinoma models of different tumor integrin av $\beta$ 3 expression levels in order to correlate the magnitude of tumor uptake with receptor density. Major Findings: In year 1, we have synthesized a series of multimeric RGD peptides with high integrin av $\beta$ 3 affinity/specificity and labeled these peptides with F-18 for PET imaging of integrin expression in vivo (Aim 1). We have also established several ovarian cancer models with differentiated integrin levels (Aim 2). Further test of the optimal radiotracer in different ovarian cancer models to correlate the tracer uptake with tumor integrin expression is currently underway (Aim 2).						
<b>15. SUBJECT TERMS</b> Ovarian Carcinoma Angiogenesis						
<b>16. SECURITY CLASSIFICATION OF:</b>			<b>17. LIMITATION OF ABSTRACT</b> UU	<b>18. NUMBER OF PAGES</b> 69	<b>19a. NAME OF RESPONSIBLE PERSON</b> USAMRMC	
<b>a. REPORT</b> U					<b>19b. TELEPHONE NUMBER</b> (include area code)	
<b>Standard Form 298 (Rev. 8-98)</b> Prescribed by ANSI Std. Z39.18						

## **Table of Contents**

<b>Introduction.....</b>	<b>3</b>
<b>Body.....</b>	<b>4</b>
<b>Key Research Accomplishments.....</b>	<b>14</b>
<b>Reportable Outcomes.....</b>	<b>15</b>
<b>Conclusions.....</b>	<b>17</b>
<b>References.....</b>	<b>18</b>
<b>Appendices.....</b>	<b>21</b>

## INTRODUCTION

Ovarian epithelial carcinomas are characterized by local proliferation and invasion of ovarian surface epithelium (OSE)-derived tumor cells, followed frequently by dissemination in the peritoneal cavity and formation of ascites containing clusters of tumor cells. This cancer is therefore characterized by the presence of two forms of cell populations, some growing as solid tumors and others in suspension (1). At each step of malignant progression, adhesive mechanisms plays an important role, and integrins are likely to participate in these events (2-8). In most ovarian cancer cells, integrin  $\alpha_v\beta_3$  is expressed and its ligand vitronectin is synthesized as a primary adhesion substrate. In fact, integrin  $\alpha_v\beta_3$  is found at a significantly higher rate in primary ovarian cancer than in ovarian tumors of low malignant potential, a fact which points to a role of  $\alpha_v\beta_3$  during ovarian cancer progression. Although the precise mechanism of tumor progression promoted via  $\alpha_v\beta_3$  is still rather inconclusive, various studies support a potential role of  $\alpha_v\beta_3$  in selective invasion and the generation of growth and survival signals (9-12). A recent study evidenced the correlation between  $\alpha_v$ -integrin expression and poor survival in ovarian carcinoma (11).

The ability to non-invasively visualize and quantify  $\alpha_v\beta_3$  integrin expression level will provide new opportunities to document tumor (tumor cells and sprouting tumor vasculature) receptor expression, more appropriately select patients considered for anti-integrin treatment and monitor treatment efficacy in integrin-positive patients (13, 14). In the past few years, we have developed a series of peptide and antibody based probes for multimodality imaging of integrin expression in vivo. This annual report will only summarize the progress highly relevant to this OCRP pilot proposal. We hypothesize that ovarian cancer integrin expression can be visualized and quantified with suitably labeled RGD peptide antagonist of integrin  $\alpha_v\beta_3$  and that the magnitude of tumor uptake from non-invasive molecular imaging may be well-correlated with tumor integrin expression levels.

## BODY

### Chemistry and Radiochemistry

Simultaneous interactions of multiple ligands and multiple receptors (multivalent molecular recognition) are common in biological systems (15, 16). Fibronectin, a native ligand for integrin receptors, possesses multiple RGD moieties for multivalent interactions with integrin receptors in epithelial cells (16). We and others found that multimeric RGD peptides could also significantly enhance the affinity of the receptor-ligand interaction through the polyvalency effect (17-20). Recent reports on the use of multimeric RGD peptides for ligand endocytosis, imaging angiogenesis, and tumor targeting have demonstrated that polyvalency is an efficient strategy for discovering (19) and developing novel RGD-based compounds with better targeting capability and higher cellular uptake due to the increased integrin recognition ability (21-23). Moreover, the apparent increase in molecular size may also prolong the circulation time of the multimers and consequently reduce tumor washout rate. The structures of c(RGDyK) (monomer), E[c(RGDyK)]<sub>2</sub> (dimer) and E{E[c(RGDyK)]<sub>2</sub>}<sub>2</sub> (tetramer) are shown in Figure 1.

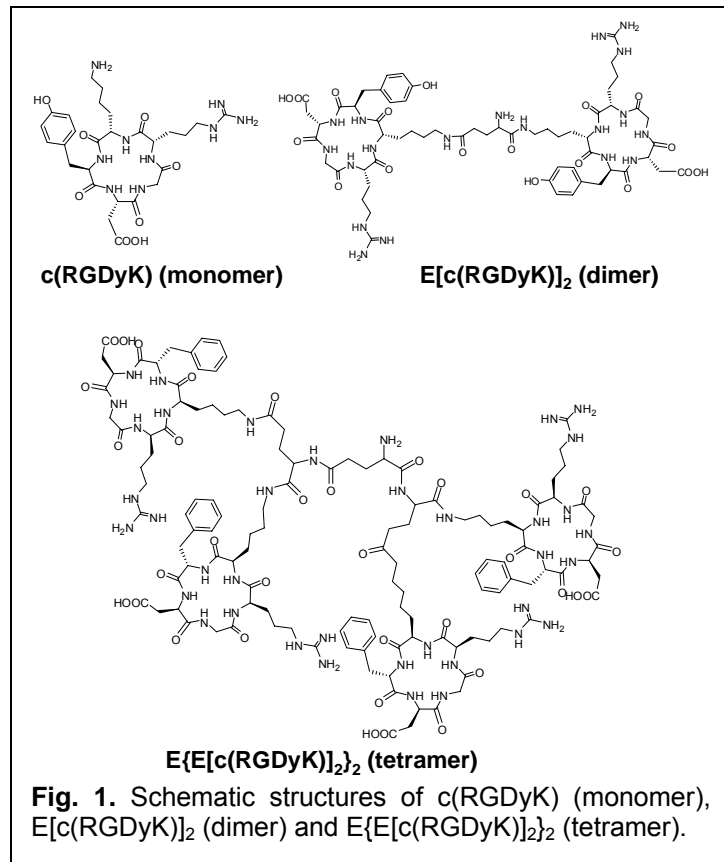


**Fig. 1.** Schematic structures of c(RGDyK) (monomer), E[c(RGDyK)]<sub>2</sub> (dimer) and E{E[c(RGDyK)]<sub>2</sub>}<sub>2</sub> (tetramer).

All three peptides shown in Figure 1 have been labeled with positron emitting radionuclide <sup>18</sup>F ( $t_{1/2} = 109.7$  min) via prosthetic labeling group *N*-succinimidyl-4-<sup>18</sup>F-fluorobenzoate (<sup>18</sup>F-SFB). The labeling yield is significantly decreased from monomer, to dimer, and to tetramer. Two reasons might be responsible for this phenomenon: first, the glutamate  $\alpha$ -amino group in the dimeric and tetrameric RGD peptides is less reactive than the lysine  $\epsilon$ -amino group in the monomeric RGD peptide. Second, the glutamate  $\alpha$ -amino group is buried in the bulk of multiple cyclic pentapeptides, which is not as easy accessible to <sup>18</sup>F-SFB as the monomeric RGD peptide. In order to improve the labeling yield, we thus inserted a mini-PEG spacer, 11-amino-3,6,9-trioxaundecanoic acid, with three ethylene oxide units, onto the glutamate  $\alpha$ -amino group of the dimeric RGD peptide E[c(RGDyK)]<sub>2</sub> (denoted as RGD2) and tetrameric RGD peptide E{E[c(RGDyK)]<sub>2</sub>}<sub>2</sub>. The mini-PEG increased the overall hydrophilicity and alleviated the steric hindrance thereby

increased the  $^{18}\text{F}$ -labeling yield. Since the spacer is quite short, such modification did not significantly alternate the receptor binding affinity and the *in vivo* kinetics of the tracer.

The total time for  $^{18}\text{F}$ -SFB synthesis was about 100 min and the decay-corrected yield was  $67\% \pm 11\%$  ( $n = 10$ ). The yield of  $^{18}\text{F}$ -SFB coupling with miniPEG-E[c(RGDyK)]<sub>2</sub> (denoted as PRGD2) is about 60% and miniPEG-E{E[c(RGDyK)]<sub>2</sub>}<sub>2</sub> (denoted as PRGD4) is over 20% (decay-corrected, based on  $^{18}\text{F}$ -SFB). If no miniPEG spacer was added to the RGD peptides, the radiolabeling yield under the same condition for RGD dimer is about 4-5% and that for RGD tetramer is almost undetectable.

### *In Vitro Characterization of RGD Tracers*

In vitro integrin  $\alpha_v\beta_3$ -binding affinities and specificities of RGD4, PRGD4 and FPRGD4 were assessed via displacement cell binding assays using  $^{125}\text{I}$ -echistatin as the integrin-specific radioligand. Experiments were performed on U87MG human glioblastoma cells by the method previously described (17, 24). The best-fit 50% inhibitory concentration ( $\text{IC}_{50}$ ) values for the U87MG cells were calculated by fitting the data with nonlinear regression using Graph-Pad Prism (GraphPad Software, Inc.). Experiments were performed with triplicate samples.

The receptor-binding affinity of RGD2, PRGD2, FPRGD2, RGD4, PRGD4 and FPRGD4 was determined by performing competitive displacement studies with  $^{125}\text{I}$ -echistatin. All peptides inhibited the binding of  $^{125}\text{I}$ -echistatin (integrin  $\alpha_v\beta_3$  specific) to U87MG cells in a concentration dependent manner. The tetramers showed significantly higher receptor affinity than the dimer (e.g.  $\text{IC}_{50}$  value for RGD2 is about  $26.1 \pm 3.2 \text{ nM}$  and that for RGD4 is about  $6.9 \pm 0.5 \text{ nM}$ ). The presence of the mini-PEG linker and/or the prosthetic group (FB) had minimal effect on the receptor avidity.

### *Metabolic Stability*

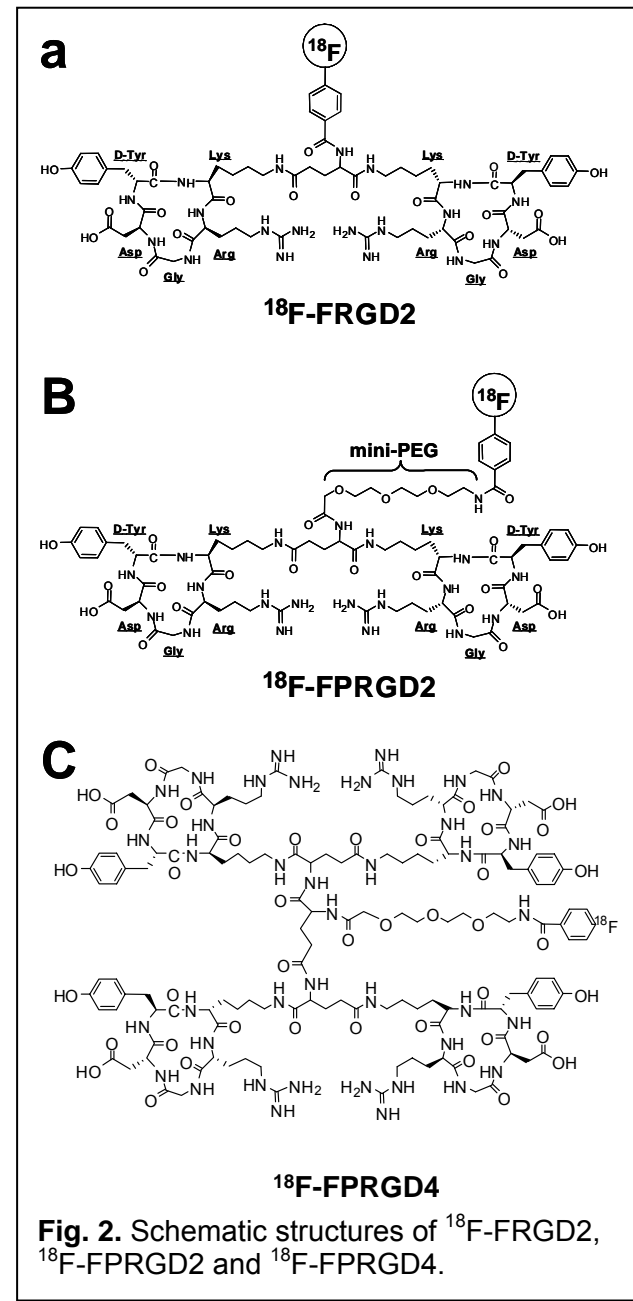


**Fig. 2.** Schematic structures of  $^{18}\text{F}$ -FRGD2,  $^{18}\text{F}$ -FPRGD2 and  $^{18}\text{F}$ -FPRGD4.

The metabolic stability of  $^{18}\text{F}$ -FPRGD2 was determined in mouse blood and urine samples and in the liver, kidneys, and U87MG tumor homogenates at 1 h p.i. (Table 1). After centrifugation of the tissue homogenates, the majority of the injected radioactivity (75-95%) was in the supernatant (denoted as “extraction efficiency”), indicating successful recovery of the radiotracer from the mouse tissue. After passing the supernatant through C<sub>18</sub> Sep-Pak cartridges, most of the radioactivity was trapped and the non-retained fraction was less than 30%. After ACN elution, the radioactivity of each sample was injected onto an analytical HPLC and the HPLC chromatograms are shown in Figure 3. The fraction of intact tracer ( $R_t$ : 15.8 min) was between 68 % and 100 % (Table 1). A minor metabolite peak was found at about 13~14 min for the blood and liver samples. No defluoridation was observed throughout the study. The metabolic stability of  $^{18}\text{F}$ -FPRGD2 was similar to  $^{18}\text{F}$ -FRGD2 (percentage of intact tracer was between 79% and 96%), demonstrating the incorporation of the mini-PEG spacer did not change the stability of the tracer *in vivo*.  $^{18}\text{F}$ -FPRGD4 is also rather stable *in vivo* (data not shown).

**Table 1.** Extraction efficiency, elution efficiency, and HPLC analysis of soluble fractions of tissue homogenates at 1 h post-injection of  $^{18}\text{F}$ -FPRGD2 (“ND” denotes “not determined”).

Fraction	Blood	Urine	Liver	Kidney	U87MG
Extraction efficiency (%)					
Unsoluble fraction	5.2	ND	23.3	21.8	24.4
Soluble fraction	94.8	ND	76.7	78.2	75.6
Elution efficiency (%)					
Nonretained fraction	2.4	1.2	23.7	12.6	28.4
Wash water	1.2	0.2	4.3	2.0	4.3
Acetonitrile eluent	96.4	98.6	72.0	85.4	67.4
HPLC analysis (%)					
Intact tracer	74.2	99.6	68.8	97.1	96.6

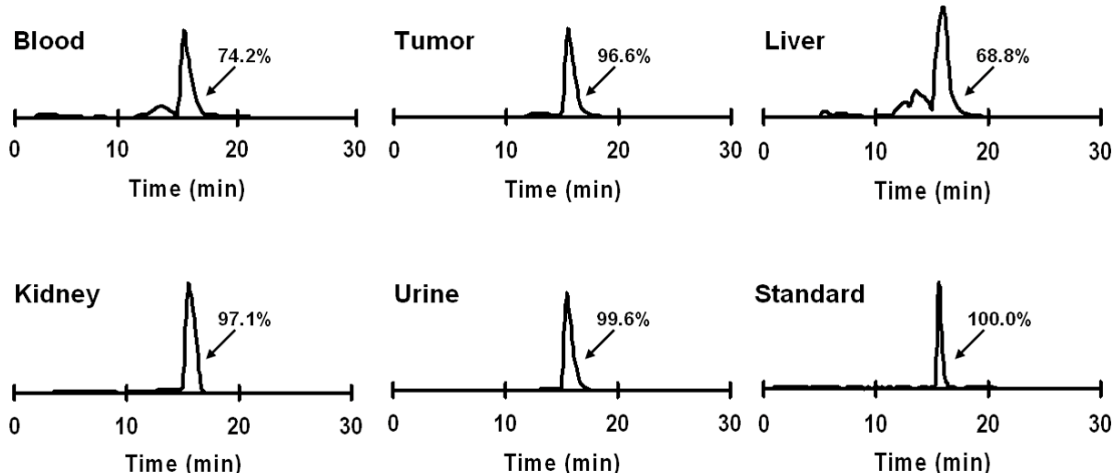


**Fig. 3.** Metabolic stability of  $^{18}\text{F}$ -FPRGD2 in mouse blood and urine samples and in liver, kidneys, and U87MG tumor homogenates at 1 h after injection. The HPLC profile of pure  $^{18}\text{F}$ -FPRGD2 (Standard) is also shown.

### Quantitative MicroPET Imaging with $^{18}\text{F}$ -FPRGD2

Dynamic microPET scans were performed on U87MG xenograft model and selected coronal images at different time points after injecting  $^{18}\text{F}$ -FPRGD2 were shown in Figure 4a. High tumor uptake was observed as early as 5 min after injection. The U87MG tumor uptake was  $4.9 \pm 0.1$ ,  $3.4 \pm 0.3$ , and  $2.7 \pm 0.1$  %ID/g at 30 min, 1 h, and 2 h p.i. respectively ( $n = 3$ ). Most activity in the non-targeted tissues and organs had been cleared by 1 h p.i. For example, the uptake values in the kidneys, liver, and lung were as low as  $2.0 \pm 0.6$ ,  $1.1 \pm 0.3$ , and  $0.5 \pm 0.2$  %ID/g, respectively at 1 h p.i. For direct visual comparison, representative serial microPET images of U87MG tumor mice after injection of  $^{18}\text{F}$ -FRGD2 were also shown (Fig. 4b). It can be seen that both tracers gave comparable imaging quality, indicating that the mini-PEG spacer did not significantly alter the tumor targeting efficacy *in vivo*. Because of the very low tracer uptake in most organs especially in the abdominal region,  $^{18}\text{F}$ -FPRGD2 is suitable for imaging integrin positive lesions in most areas except for

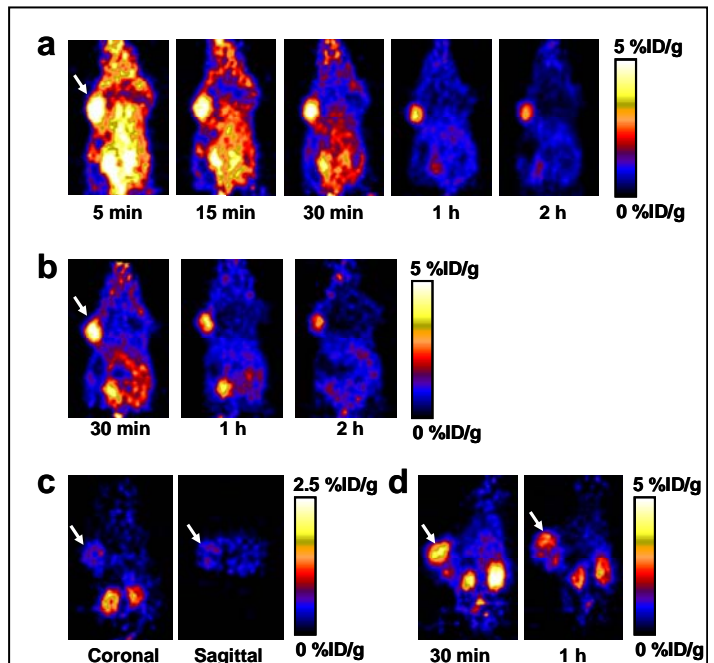


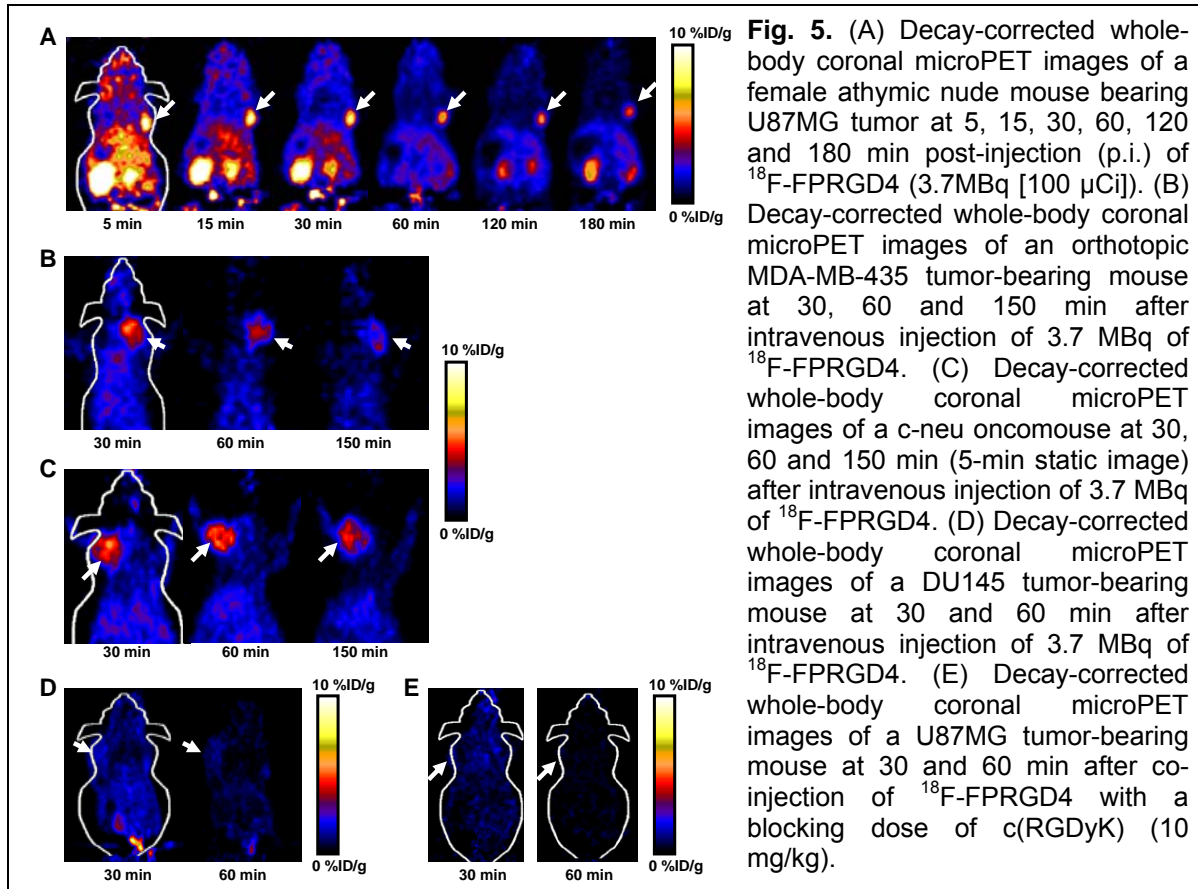
**Fig. 4.** (a) Serial microPET images of U87MG tumor-bearing mice after intravenous injection of  $^{18}\text{F}$ -FPRGD2. (b) For direct visual comparison, serial microPET images of U87MG tumor-bearing mice after intravenous injection of  $^{18}\text{F}$ -FRGD2 are also shown. (c) Coronal and sagittal microPET images of a U87MG tumor-bearing mouse 1 h after co-injection of  $^{18}\text{F}$ -FPRGD2 and a blocking dose of c(RGDyK). Note that the scale (0-2.5 %ID/g) is different from those in (a) and (b) (0-5 %ID/g). (d) MicroPET images of a c-neu oncomouse after intravenous injection of  $^{18}\text{F}$ -FPRGD2. Arrows indicate tumors in all cases.

the kidneys and the urinary bladder. Time-activity curves showed that this tracer excreted predominantly through the renal route (data not shown).

The integrin  $\alpha_v\beta_3$  specificity of  $^{18}\text{F}$ -FPRGD2 in vivo was confirmed by a blocking experiment where the tracer was co-injected with c(RGDyK) (10 mg/kg). As can be seen from Figure 2c, the U87MG tumor uptake in the presence of non-radiolabeled RGD peptide ( $0.5 \pm 0.2 \text{ \%ID/g}$ ) is significantly lower than that without RGD blocking ( $3.4 \pm 0.3 \text{ \%ID/g}$ ) ( $P < 0.001$ ). Similar as previously reported (24), the tracer cleared from the body significantly faster and the uptake in most organs (e.g. kidneys and liver) were also lower than those without c(RGDyK) blocking. Western blot and immunohistochemical staining also confirmed that these organs express low levels of integrin  $\alpha_v\beta_3$  (data not shown).

### *Quantitative MicroPET Imaging with $^{18}\text{F}$ -FPRGD4*

Dynamic microPET scans were performed on U87MG xenograft model and selected coronal images at different time points after injection of  $^{18}\text{F}$ -FPRGD4 were shown in Figure 5A. The tumor was clearly visible with high contrast to contralateral background as early as 5 min p.i. Quantitation of tumor and major organ activity accumulation in microPET scans was realized by measuring ROIs encompassing the entire organ in the



coronal orientation. The U87MG tumor uptake of  $^{18}\text{F}$ -FPRGD4 was calculated to be  $9.87 \pm 0.10$ ,  $7.80 \pm 0.14$ ,  $6.40 \pm 0.27$ ,  $5.39 \pm 0.14$ , and  $4.82 \pm 0.22$  %ID/g at 5, 30, 60, 120 and 180 min p.i., respectively ( $n = 3$ ).  $^{18}\text{F}$ -FPRGD4 was cleared mainly through the kidneys. Some hepatic clearance was also observed.

Representative coronal microPET images of MDA-MB-435 tumor-bearing mice ( $n = 3$ ) at different times after tracer injection were showed in Figure 5B. As the integrin expression level in MDA-MB-435 tumor is lower than U87MG, the tumor uptake of  $^{18}\text{F}$ -FPRGD4 in MDA-MB-435 tumor ( $5.07 \pm 0.18$ ,  $4.53 \pm 0.36$ ,  $3.38 \pm 0.48$  %ID/g at 30, 60, and 150 min p.i.) was also lower than that in U87MG tumor. No significant difference in normal organs and tissues was found between these two tumor models.

$^{18}\text{F}$ -FPRGD4 was also successful in visualizing a spontaneous murine mammary carcinoma model grown in c-neu oncomice (Fig. 5C) {Harris, 2003 #20; Harris, 2006 #51; Onthank, 2004 #10; Mousa, 2005 #12; Onthank, 2004 #53}. The tumor uptakes were found to be  $4.22 \pm 0.18$ ,  $3.56 \pm 0.34$ , and  $2.36 \pm 0.40$  %ID/g at 30, 60, and 150 min, respectively ( $n = 3$ ). These values are slightly lower than those in MDA-MB-435 human breast cancer tumors grown in nude mice. No significant difference was found in major organs and tissues between the spontaneous tumor model of Balb/C strain and the xenograft models of nude mice stain.

We also tested  $^{18}\text{F}$ -FPRGD4 in an integrin negative DU145 tumor model ( $n = 3$ ). As can be seen from Figure 5D, only slightly higher than contralateral muscle background signal was detected in DU145 tumor ( $1.44 \pm 0.34$  and  $0.93 \pm 0.13$  %ID/g at 30 and 60 min p.i.). These values were significantly lower than in all other three integrin-expressing tumor models ( $P < 0.001$ ). The tumor uptake followed the trend of U87MG > MDA-MB-435 > c-neu > DU145, which is consistent with the integrin  $\alpha_v\beta_3$  expression pattern (quantified by SDS-

PAGE/autoradiography)  
(18) in these tumor models (data not shown).

The integrin  $\alpha_v\beta_3$  specificity of  $^{18}\text{F}$ -FPRGD4 in vivo was also confirmed by a blocking experiment. Representative coronal images of U87MG tumor mice after injection of  $^{18}\text{F}$ -FPRGD4 in the presence of blocking dose of c(RGDyK) (10 mg/kg of mouse body weight) were illustrated in Figure 5E. More than 80% of the

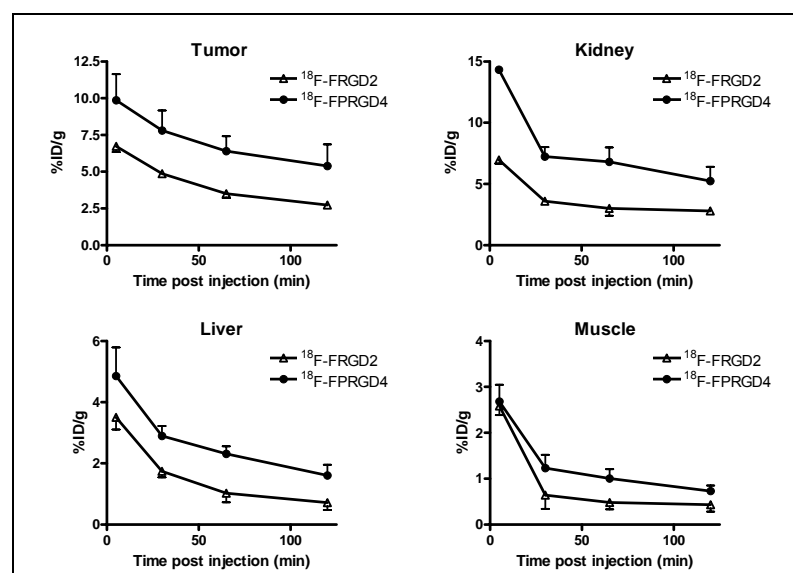


**Fig. 6.** Comparison between the uptake of  $^{18}\text{F}$ -FRGD2 and  $^{18}\text{F}$ -FPRGD4 in the U87MG tumor, kidneys, liver, and muscle over time. Data were derived from multiple time-point microPET study. ROIs are shown as the %ID/g  $\pm$  SD ( $n=3$ ).

uptake in the tumor was inhibited as compared with that in the tumor without blocking (Fig. 5A). Radioactivity accumulation in most other major organs and tissues was also significantly reduced in the presence of non-radioactive RGD peptide.

The tumor uptake and biodistribution of  $^{18}\text{F}$ -FPRGD4 derived from quantitative microPET imaging was compared with that of  $^{18}\text{F}$ -FRGD2 in the same U87MG tumor model. As shown in Figure 6, the uptake of  $^{18}\text{F}$ -FPRGD4 in U87MG tumor was significantly higher than that of  $^{18}\text{F}$ -FRGD2 at all time points examined ( $P < 0.001$ ).  $^{18}\text{F}$ -FPRGD4 also showed higher uptake than  $^{18}\text{F}$ -FRGD2 in the liver, kidneys ( $P < 0.05$ ). The initial muscle uptake of  $^{18}\text{F}$ -FPRGD4 was higher than  $^{18}\text{F}$ -FRGD2 ( $P < 0.05$ ), but the difference was diminished at late time points ( $P > 0.05$ ).

### *Correlation between PET Imaging and Integrin Expression In Vivo*

We have tested six xenograft models: U87MG glioma, C6 rat glioma, MDA-MB-435 breast cancer, PC-3 prostate cancer, NCI-H1975 and A549 non-small cell lung cancers. The dynamic microPET studies were performed by tail-vein injection of 100  $\mu\text{Ci}$  of [ $^{18}\text{F}$ ]FRGD2 under isoflurane anesthesia. The 60 min dynamic (5×60 s, 5×120 s, 5×180 s, 6×300 s) microPET data acquisition (total of 21 frames) was started 3 min after radiotracer injection. Static images at 2 h and 3 h time points were also acquired as 10 min static images. Time-activity curves showed that this tracer excreted predominantly through the renal route (Fig. 7A). Diversified tumor uptake patterns of [ $^{18}\text{F}$ ]FRGD2 were found in different xenograft models (Fig. 7B). The U87MG tumor had the highest tumor tissue integrin and tumor cell integrin levels and also had highest initial tumor uptake but also had the most rapid tumor washout, reaching a plateau after 50 min p.i. The tumors with low magnitude of tumor uptake had minimal tumor washout, providing reasonably high tumor contrast at late time points when non-specific activity accumulation in the normal organs had been mostly cleared.

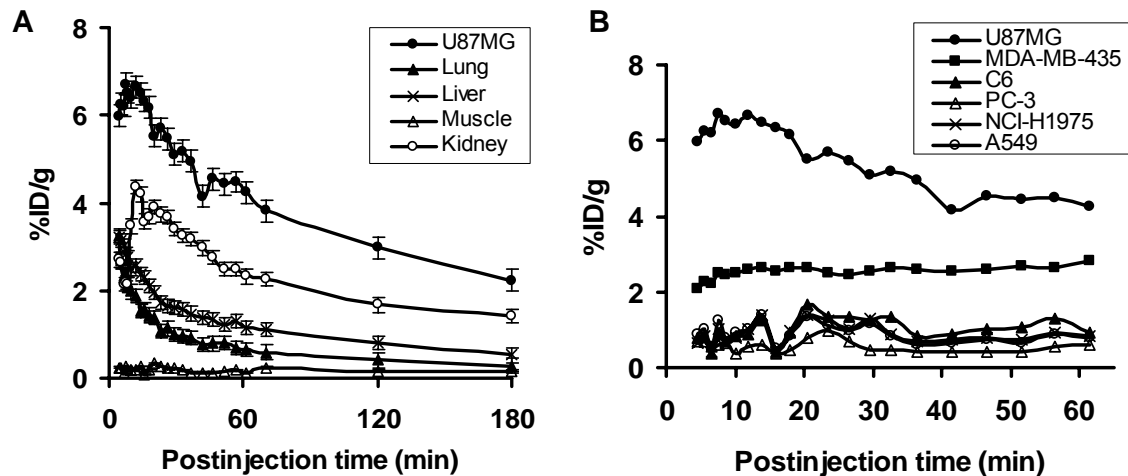


**Fig. 7** (A) Time activity curves derived from the 60 min dynamic and 70 min, 120 min, 180 min static microPET imaging study. The regions of interests (ROIs) are shown as mean % ID/g  $\pm$  SD ( $n = 3$ ). (B) Comparison of tumor uptake in nude mice derived from the 60 min dynamic microPET scans.

Logan plot is a graphical method of analysis, applicable to ligands that bind reversibly to receptors or enzymes (25). This method can calculate the distribution volume (DV) for dynamic PET data before steady state is actually reached. Patlak analysis (26) is another graphical method that is good for irreversible radioligand binding. We thus applied both Logan plot and Patlak analysis for all dynamic PET data to determine which method is more suitable for  $[^{18}\text{F}]$ FRGD2 tracer kinetics. We found that Patlak curves deflected downward for the later time points, which is probably a good indication that the tracer is actually reversible.

Logan plot analysis (25) of the PET data used normalized integrated activity in the tumor vs. the normalized integrated activity in the muscle (Eq. 1). The ratio of integrated tumor uptake divided by tumor uptake was set as the y-axis. The ratio of integrated reference tissue uptake divided tumor uptake was set as the x-axis of Logan plot (here we select muscle as reference tissue because of its low integrin expression). The slope of the linear portion of Logan plot was distribution volume ratio (DVR). The binding potential (BP) = DVR – 1. This method can calculate the distribution volume (DV) for dynamic PET data before steady state is actually reached. We used 26.5 min as starting point for linear regression of the dynamic microPET studies since all graphs became linear after that point with the slope being DVR (Fig. 8).

The calculated binding potentials ( $B_{\max}/K_d$ ) for  $[^{18}\text{F}]$ FRGD2 in the U87MG, MDA-MB-435, C6, PC-3, NCI-H1975, and A549 tumors using muscle as reference tissue were found to be 29.5, 17.5, 5.8, 1.9, 4.1 and 3.8, respectively.

$$\frac{\int_0^T C_t(t)dt}{C_t(T)} = \text{DVR} \times \frac{\int_0^T C_r(t)dt}{C_r(T)} + C \quad \text{Eq. 1}$$

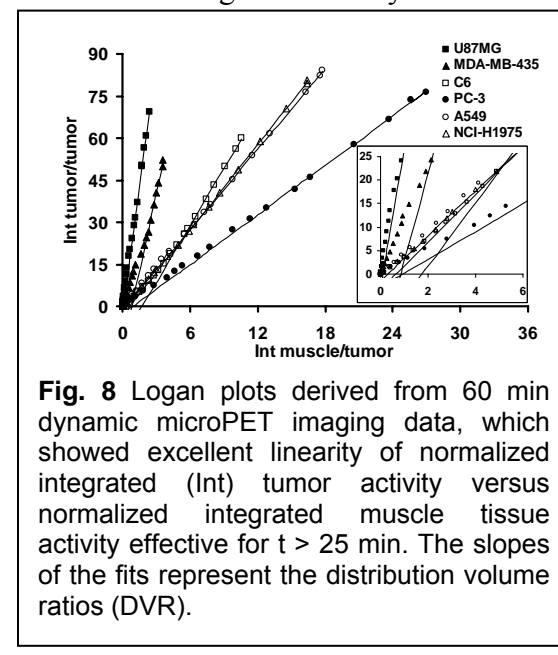


**Fig. 8** Logan plots derived from 60 min dynamic microPET imaging data, which showed excellent linearity of normalized integrated (Int) tumor activity versus normalized integrated muscle tissue activity effective for  $t > 25$  min. The slopes of the fits represent the distribution volume ratios (DVR).

Quantification of cell or tissue integrin  $\alpha_v\beta_3$  expression by immunoblotting is technically challenging due to the heterodimeric feature of this G-protein receptor. Both anti- $\alpha_v$  and anti- $\beta_3$  antibodies are thus needed to confirm the presence of integrin  $\alpha_v\beta_3$  and yet it is difficult to be quantitative (27). It was recently reported that SDS-polyacrylamide gel electrophoresis and autoradiograms and revealed that  $^{125}\text{I}$ -echistatin forms SDS-stable complex with certain integrins (resistant to 0.6% SDS) in the absence of chemical cross-linkers, reducing conditions and heating (28). Tumor-bearing mice were sacrificed 24 h after dynamic microPET imaging. The quantitation of tumor tissue integrin level was performed by incubating NP-40 solubilized tumor tissue lysate with  $^{125}\text{I}$ -echistatin in the presence of increasing concentrations of non-radiolabeled echistatin (28). Tumor tissues

integrin expressions were then quantified by SDS-PAGE and autoradiography. Briefly, solubilized tumor tissues were obtained by addition of 0.1 mL/cm<sup>2</sup> of lysis buffer (0.05 M HEPES, pH 7.4, 1% Nonidet P-40 (NP-40), 1 mM CaCl<sub>2</sub>, and 1 mM MgCl<sub>2</sub>). After incubating on ice for 10-20 min, the samples were collected and centrifuged at 15,000 rpm for 3 min. The resulting solution was then analyzed for total protein content by MicroBCA protein assay. Samples were assayed in triplicate. Twenty µg of proteins were incubated in a final volume

of 25 µL in binding buffer in the presence of 1.85 KBq of <sup>125</sup>I-echistatin and various amount of echistatin (1 to 100 nM). After 2 h incubation at room temperature, the mixtures were loaded onto 4%-10% SDS-PAGE gels. After electrophoresis, the gels were dried and subjected to autoradiography overnight. Radioactive bands were developed and quantified in Cyclone Phosphoimager system (Perkin-Elmer Inc., Boston, MA). The same dose of <sup>125</sup>I-echistatin without forming complex with integrin was used as a standard and 15 ng of purified integrin α<sub>v</sub>β<sub>3</sub> (Chemicon, Temecula, CA) was used as a positive control and molecular marker. Each competition curve was then fitted by the Hill equation (GraphPad). A representative autoradiogram of a competition experiment for A549 tumor is shown in **Fig. 9A**. The linear portion of the sigmoid curve (**Fig. 9B**) was used to generate the Scatchard transformation and the B<sub>max</sub> (**Fig. 9C**).

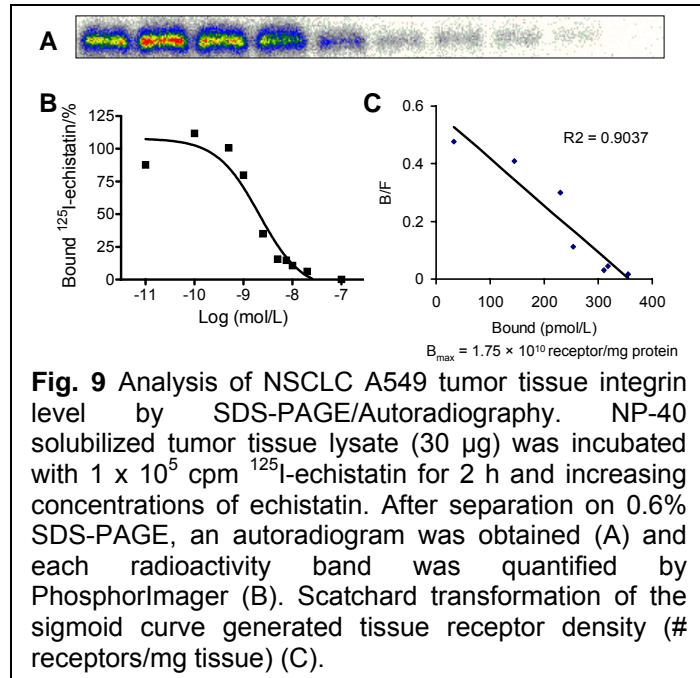


**Fig. 9** Analysis of NSCLC A549 tumor tissue integrin level by SDS-PAGE/Autoradiography. NP-40 solubilized tumor tissue lysate (30 µg) was incubated with 1 × 10<sup>5</sup> cpm <sup>125</sup>I-echistatin for 2 h and increasing concentrations of echistatin. After separation on 0.6% SDS-PAGE, an autoradiogram was obtained (A) and each radioactivity band was quantified by PhosphorImager (B). Scatchard transformation of the sigmoid curve generated tissue receptor density (# receptors/mg tissue) (C).

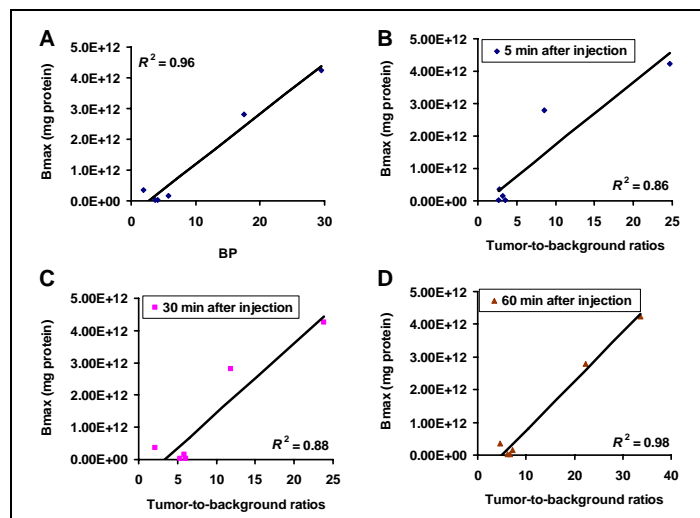


**Fig. 10** (A) Correlation analysis between tumor tissue receptor density (Bmax/mg protein measured from SDS-PAGE/autoradiography using <sup>125</sup>I-echistatin as radioligand) vs. binding potential (BP) (calculated from Logan plot transformation of dynamic microPET imaging data). (B-D) Tumor tissue receptor density vs. tumor/background ratio at 5 min (B), 30 min (C) and 1 h (D) post-injection of [<sup>18</sup>F]FRGD2.

A representative autoradiogram of a competition experiment for A549 tumor is shown in **Fig. 9A**. The linear portion of the sigmoid curve (**Fig. 9B**) was used to generate the Scatchard transformation and the B<sub>max</sub> (**Fig. 9C**).

A linear relationship was found between the BP values calculated from graphical analysis of dynamic microPET imaging and the  $B_{max}$  values measured from SDS-PAGE/autoradiograms ( $R^2 = 0.96$ ,  $P = 0.005$ ) (Fig. 10). The tumor to contralateral background ratios did not provide the same level of correlation with the tumor tissue integrin density at early time points (e.g. Pearson's correlation coefficient  $R^2$  was 0.86 at 5 min and 0.88 at 30 min p.i.). At 1 h p.i., a good linear relationship was found between tumor/background ratio and tumor integrin level, thus making it possible to quantify tumor integrin expression level *in vivo* with static PET scans and [<sup>18</sup>F]FRGD2.

### Ovarian Cancer Model Study

We have tested three ovarian cancer cell lines: SKOV-3, OVCAR-3, and 2008. RT-PCR (Fig. 11) showed that SKOV-3 cells express high levels of  $\alpha v \beta 3$ , OVCAR-3 cells express high level of  $\alpha v$  but low level of  $\beta 3$ , and 2008 cells express low level of  $\alpha v$  and is almost negative for  $\beta 3$ . We are currently in the process of transfecting OVCAR3 cell line with integrin  $\beta 3$  to render the cell line integrin positive. We are also trying to knock down integrin  $\beta 3$ . The integrin expression levels *in vivo* in both subcutaneous and orthotopic tumors will be assessed by quantitative PET imaging with <sup>18</sup>F-labeled dimeric and tetrameric RGD peptides, which will be the major effort for the 2<sup>nd</sup> year of the pilot grant funding.

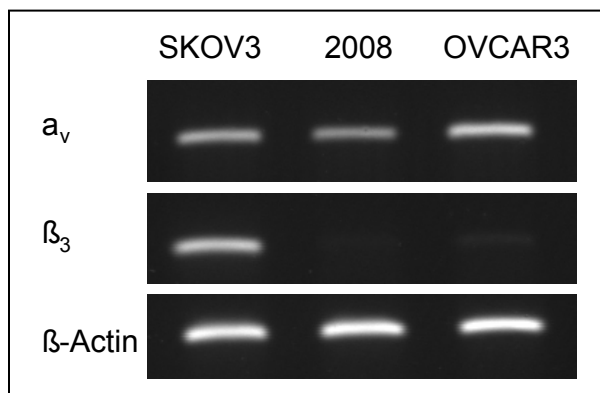


**Fig. 11.** The mRNA levels of integrin  $\alpha v$  and  $\beta 3$  in SKOV-3, OVCAR-3, and 2008 were determined by reverse transcriptase PCR.

## **KEY ACCOMPLISHMENTS**

- Developed a series of RGD peptide ligands for integrin  $\alpha v\beta 3$  based on polyvalency effect;
- Successfully labeled mono, di, and tetarmeric RGD peptides with F-18 through  $^{18}\text{F}$ -SFB prosthetic group;
- Assess the in vitro receptor affinity and in vivo tumor targeting efficacy of different RGD peptide tracers;
- Correlated the quantitative PET imaging results with tumor integrin expression level in multiple xenograft models;
- Established several ovarian cancer models for test the optimal RGD peptide tracers.

## REPORTABLE OUTCOMES

### Publications:

Cai W, Rao J, Gambhir SS, Chen X

Molecular Imaging in Anti-Angiogenic Drug Development  
*Mol Cancer Ther.* 2006;5(11): 2624-33.

Chen X

Multimodality Imaging of Tumor Integrin alpha(v)beta(3) Expression.  
*Mini Rev Med Chem.* 2006;6(2):227-34.

Cai W, Zhang X, Wu Y, Chen X.

A thiol-reactive <sup>18</sup>F-labeling agent, N-[2-(4-<sup>18</sup>F-fluorobenzamido)ethyl]maleimide, and synthesis of RGD peptide-based tracer for PET imaging of  $\alpha_v\beta_3$  integrin expression.

*J Nucl Med.* 2006;47(7):1172-1180.

Cai W, Gambhir SS, Chen X.

Multimodality Tumor Imaging Targeting Integrin  $\alpha_v\beta_3$   
*Biotechniques.* 2005;39:S6-S17 (Review).

Zhang X, Xiong Z, Wu Y, Tseng JR, Gambhir SS, Chen X.

Quantitative PET Imaging of Tumor Integrin  $\alpha_v\beta_3$  Expression with [<sup>18</sup>F]FRGD2.  
*J Nucl Med.* 2006;47:113-121.

### Conference Abstracts:

Li Z-B, Wu Z, He L, Chin FT, Chen X

“Click” labeling of RGD peptide with <sup>18</sup>F and microPET imaging of  $\alpha_v\beta_3$  integrin expression

54<sup>th</sup> SNM Annual meeting, Washington, DC June 2007

Wu Z, Li Z-B, Cai W, He L, Chin FT, Li F, Chen X

microPET Imaging of Tumor  $\alpha_v\beta_3$  Integrin Expression Using <sup>18</sup>F-labeled PEGylated Tetrameric RGD Peptide (<sup>18</sup>F-FPRGD4)

54<sup>th</sup> SNM Annual meeting, Washington, DC June 2007

Wu Z, Li Z-B, Cai W, He L, Chin FT, Li F, Chen X

<sup>18</sup>F-labeled mini-PEG spaced RGD dimer (<sup>18</sup>F-FPRGD2): synthesis and microPET imaging of  $\alpha_v\beta_3$  integrin expression

54<sup>th</sup> SNM Annual meeting, Washington, DC June 2007

Chen X

Multimodality imaging of tumor angiogenesis  
232nd ACS National Meeting, San Francisco, CA, September, 2006

Zhang X, Cai W, Wu Y, Chen X

Positron Emission Tomography Imaging of  $\alpha_v\beta_3$  Integrin Expression using RGD Peptide-Based Tracer Synthesized via a Novel Thiol-Reactive  $^{18}\text{F}$ -Labeling Agent *N*-[2-(Aminoethyl)maleimide]-4-[ $^{18}\text{F}$ ]Fluorobenzamide ( $[^{18}\text{F}]AMFB$ )  
53<sup>rd</sup> SNM Annual meeting, San Diego, CA, June 2006

Zhang X, Xiong Z, Wu Y, Cai W, Tseng JR, Gambhir SS, Chen X.

Quantitative PET Imaging of Tumor Integrin  $\alpha_v\beta_3$  Expression with  $[^{18}\text{F}]FRGD2$   
AMI International Conference 2005, Orlando, FL, March, 2006.

## **CONCLUSIONS**

In conclusion, we have successfully accomplished all the tasks proposed in Specific Aim 1. We have also started to tackle Aim 2 by establishing the analytical methods to quantify integrin expression *in vivo*. We are also establishing ovarian cancer models with titratable integrin levels so we can correlate the quantitative PET imaging *in vivo* with integrin level measured *ex vivo*.

## REFERENCES

1. Hamilton TC. Ovarian cancer, Part I: Biology. *Curr Probl Cancer*. Jan-Feb 1992;16(1):1-57.
2. Moser TL, Pizzo SV, Bafetti LM, Fishman DA, Stack MS. Evidence for preferential adhesion of ovarian epithelial carcinoma cells to type I collagen mediated by the alpha2beta1 integrin. *Int J Cancer*. Sep 4 1996;67(5):695-701.
3. Cruet S, Salamanca C, Mitchell GW, Auersperg N. alphavbeta3 and vitronectin expression by normal ovarian surface epithelial cells: role in cell adhesion and cell proliferation. *Gynecol Oncol*. Nov 1999;75(2):254-260.
4. Carreiras F, Denoux Y, Staedel C, Lehmann M, Sichel F, Gauduchon P. Expression and localization of alpha v integrins and their ligand vitronectin in normal ovarian epithelium and in ovarian carcinoma. *Gynecol Oncol*. Aug 1996;62(2):260-267.
5. Cannistra SA, Ottensmeier C, Niloff J, Orta B, DiCarlo J. Expression and function of beta 1 and alpha v beta 3 integrins in ovarian cancer. *Gynecol Oncol*. Aug 1995;58(2):216-225.
6. Bartolazzi A, Cerboni C, Flamini G, Bigotti A, Lauriola L, Natali PG. Expression of alpha 3 beta 1 integrin receptor and its ligands in human lung tumors. *Int J Cancer*. Aug 22 1995;64(4):248-252.
7. Liapis H, Adler LM, Wick MR, Rader JS. Expression of alpha(v)beta3 integrin is less frequent in ovarian epithelial tumors of low malignant potential in contrast to ovarian carcinomas. *Hum Pathol*. Apr 1997;28(4):443-449.
8. Goldberg I, Davidson B, Reich R, et al. Alphav integrin expression is a novel marker of poor prognosis in advanced-stage ovarian carcinoma. *Clin Cancer Res*. Dec 2001;7(12):4073-4079.
9. van der Flier A, Sonnenberg A. Function and interactions of integrins. *Cell Tissue Res*. Sep 2001;305(3):285-298.
10. Hapke S, Kessler H, Luber B, et al. Ovarian cancer cell proliferation and motility is induced by engagement of integrin alpha(v)beta3/Vitronectin interaction. *Biol Chem*. Jul 2003;384(7):1073-1083.
11. Davidson B, Goldberg I, Reich R, et al. AlphaV- and beta1-integrin subunits are commonly expressed in malignant effusions from ovarian carcinoma patients. *Gynecol Oncol*. Aug 2003;90(2):248-257.

12. Cruet-Hennequart S, Maubant S, Luis J, Gauduchon P, Staedel C, Dedhar S. alpha(v) integrins regulate cell proliferation through integrin-linked kinase (ILK) in ovarian cancer cells. *Oncogene*. Mar 20 2003;22(11):1688-1702.
13. Chen X. Multimodality imaging of tumor integrin alphavbeta3 expression. *Mini Rev Med Chem*. Feb 2006;6(2):227-234.
14. Cai W, Gambhir SS, Chen X. Multimodality tumor imaging targeting integrin  $\alpha_v\beta_3$ . *Biotechniques*. 2005;39:S6-S17.
15. Sharma V, Luker Gary D, Piwnica-Worms D. Molecular imaging of gene expression and protein function *in vivo* with PET and SPECT. *J Magn Reson Imaging*. Oct 2002;16(4):336-351.
16. Mammen M, Chio S, Whitesides GM. Polyvalent interactions in biological systems: implications for design and use of multivalent ligands and inhibitors. *Angew Chem Int Ed Engl*. 1998;37(20):2755-2794.
17. Wu Y, Zhang X, Xiong Z, et al. MicroPET imaging of glioma  $\alpha_v$ -integrin expression using  $^{64}\text{Cu}$ -labeled tetrameric RGD peptide. *J Nucl Med*. 2005;46:1707-1718.
18. Zhang X, Xiong Z, Wu X, et al. Quantitative PET imaging of tumor integrin  $\alpha_v\beta_3$  expression with  $^{18}\text{F}$ -FRGD2. *J Nucl Med*. 2006;47(1):113-121.
19. Liu S. Radiolabeled multimeric cyclic RGD peptides as integrin alphavbeta3 targeted radiotracers for tumor imaging. *Mol Pharm*. Sep-Oct 2006;3(5):472-487.
20. Ye Y, Bloch S, Xu B, Achilefu S. Design, synthesis, and evaluation of near infrared fluorescent multimeric RGD peptides for targeting tumors. *J Med Chem*. Apr 6 2006;49(7):2268-2275.
21. Boturyn D, Coll JL, Garanger E, Favrot MC, Dumy P. Template assembled cyclopeptides as multimeric system for integrin targeting and endocytosis. *J Am Chem Soc*. May 12 2004;126(18):5730-5739.
22. Montet X, Ntziachristos V, Grimm J, Weissleder R. Tomographic fluorescence mapping of tumor targets. *Cancer Res*. 2005;65(14):6330-6336.
23. Thumshirn G, Hersel U, Goodman SL, Kessler H. Multimeric cyclic RGD peptides as potential tools for tumor targeting: solid-phase peptide synthesis and chemoselective oxime ligation. *Chemistry*. Jun 16 2003;9(12):2717-2725.
24. Cai W, Zhang X, Wu Y, Chen X. A thiol-reactive  $^{18}\text{F}$ -labeling agent  $N$ -[2-(4- $^{18}\text{F}$ -fluorobenzamido)ethyl]maleimide ( $^{18}\text{F}$ -FBEM) and the synthesis of RGD peptide-

- based tracer for PET imaging of  $\alpha_v\beta_3$  integrin expression. *J Nucl Med.* 2006;47(7):1172-1180.
25. Logan J. Graphical analysis of PET data applied to reversible and irreversible tracers. *Nucl Med Biol.* Oct 2000;27(7):661-670.
  26. Patlak CS, Blasberg RG. Graphical evaluation of blood-to-brain transfer constants from multiple-time uptake data. Generalizations. *J Cereb Blood Flow Metab.* Dec 1985;5(4):584-590.
  27. Wong NC, Mueller BM, Barbas CF, et al.  $\alpha_v$  Integrins mediate adhesion and migration of breast carcinoma cell lines. *Clin Exp Metastasis.* 1998;16(1):50-61.
  28. Thibault G. Sodium dodecyl sulfate-stable complexes of echistatin and RGD-dependent integrins: a novel approach to study integrins. *Mol Pharmacol.* Nov 2000;58(5):1137-1145.

## APPENDICES

Cai W, Rao J, Gambhir SS, Chen X  
Molecular Imaging in Anti-Angiogenic Drug Development  
*Mol Cancer Ther.* 2006;5(11): 2624-33.

### Chen X

Multimodality Imaging of Tumor Integrin alpha(v)beta(3) Expression.  
*Mini Rev Med Chem.* 2006;6(2):227-34.

Cai W, Zhang X, Wu Y, Chen X.  
A thiol-reactive  $^{18}\text{F}$ -labeling agent, N-[2-(4- $^{18}\text{F}$ -fluorobenzamido)ethyl]maleimide, and synthesis of RGD peptide-based tracer for PET imaging of  $\alpha_v\beta_3$  integrin expression.  
*J Nucl Med.* 2006;47(7):1172-1180.

Cai W, Gambhir SS, Chen X.  
Multimodality Tumor Imaging Targeting Integrin  $\alpha_v\beta_3$   
*Biotechniques.* 2005;39:S6-S17 (Review).

Zhang X, Xiong Z, Wu Y, Tseng JR, Gambhir SS, Chen X.  
Quantitative PET Imaging of Tumor Integrin  $\alpha_v\beta_3$  Expression with  $[^{18}\text{F}]$ FRGD2.  
*J Nucl Med.* 2006;47:113-121.

## Drug Development Series: Review

# How molecular imaging is speeding up antiangiogenic drug development

Weibo Cai,<sup>1</sup> Jianghong Rao,<sup>1</sup> Sanjiv S. Gambhir,<sup>1,2</sup> and Xiaoyuan Chen<sup>1</sup>

<sup>1</sup>The Molecular Imaging Program at Stanford, Department of Radiology and Bio-X Program and <sup>2</sup>Department of Bioengineering, Stanford University School of Medicine, Stanford, California

### Abstract

Drug development is a long process that generally spans about 10 to 15 years. The shift in recent drug discovery to novel agents against specific molecular targets highlights the need for more robust molecular imaging platforms. Using molecular probes, molecular imaging can aid in many steps of the drug development process, such as providing whole body readout in an intact system, decreasing the workload and speeding up drug development/validation, and facilitating individualized anticancer treatment monitoring and dose optimization. The main focus of this review is the recent advances in tumor angiogenesis imaging, and the targets include vascular endothelial growth factor and vascular endothelial growth factor receptor, integrin  $\alpha_v\beta_3$ , matrix metalloproteinase, endoglin (CD105), and E-selectin. Through tumor angiogenesis imaging, it is expected that a robust platform for understanding the mechanisms of tumor angiogenesis and evaluating the efficacy of novel antiangiogenic therapies will be developed, which can help antiangiogenic drug development in both the preclinical stage and the clinical settings. Molecular imaging has enormous potential in improving the efficiency of the drug development process, including the specific area of antiangiogenic drugs. [Mol Cancer Ther 2006;5(11):2624–33]

Received 7/10/06; revised 8/29/06; accepted 9/12/06.

**Grant support:** National Institute of Biomedical Imaging and Bioengineering grant R21 EB001785; National Cancer Institute grants R21 CA102123, P50 CA114747, U54 CA119367, and R24 CA93862; Department of Defense grant W81XWH-04-1-0697, W81XWH-06-1-0665, W81XWH-06-1-0042, and DAMD17-03-1-0143; and Benedict Cassen Postdoctoral Fellowship from the Education and Research Foundation of the Society of Nuclear Medicine (W. Cai).

**Requests for reprints:** Xiaoyuan Chen, The Molecular Imaging Program at Stanford, Department of Radiology and Bio-X Program, Stanford University School of Medicine, 1201 Welch Road, PO95, Stanford, CA 94305-5484. Phone: 650-725-0950; Fax: 650-736-7925. E-mail: shawchen@stanford.edu

Copyright © 2006 American Association for Cancer Research.  
doi:10.1158/1535-7163.MCT-06-0395

### Introduction

Cancer drug discovery is a relatively long process. Rational predefined steps have been streamlined for drug development in recent years, thanks to the development of many new technologies (Fig. 1). Many imaging techniques have been routinely used in the drug discovery process to directly monitor the drug in blood, normal, and tumor tissues and to evaluate the effects of the drug in the context of tumor (1, 2). Anatomic/functional imaging modalities, such as computed tomography, magnetic resonance imaging, and ultrasound, have been used to assess tumor size and structure. They can also provide valuable information on tumor perfusion, integrity of the blood-brain barrier, vessel density, vessel permeability, blood oxygenation, blood volume, blood flow, blood velocity, and flow resistance. However, with the recent shift in drug discovery from conventional cytotoxic drugs to novel agents against specific molecular targets, these conventional imaging modalities are usually no longer adequate. Cytostatic therapies are much less toxic, and disease stabilization may not lead to shrinkage of tumors in a short period of time. Molecular imaging recently emerges with increasing popularity as it can be used to monitor the changes at the molecular level *in vivo*, and it can help in evaluating treatment efficacy much earlier.

Molecular imaging refers to the characterization and measurement of biological processes at the molecular level (3). For a representative comprehensive review, the readers are referred to ref. 3. Molecular imaging techniques include positron emission tomography (PET), single-photon emission computed tomography (SPECT), molecular magnetic resonance imaging, magnetic resonance spectroscopy, optical bioluminescence, optical fluorescence, and targeted ultrasound (3). Molecular imaging can give whole body readout in an intact system, help to decrease the workload and speed up the drug development process, provide more statistically relevant results because longitudinal studies can be done in the same animals, aid in lesion detection and patient stratification, and help in individualized anticancer treatment monitoring and dose optimization.

Several excellent review articles have been published on the general role of molecular imaging on drug development (2, 4–6). For the remaining of this review article, we will mainly focus on expounding the role of molecular imaging in antiangiogenic drug development and briefly summarize the recent advances in tumor angiogenesis imaging.

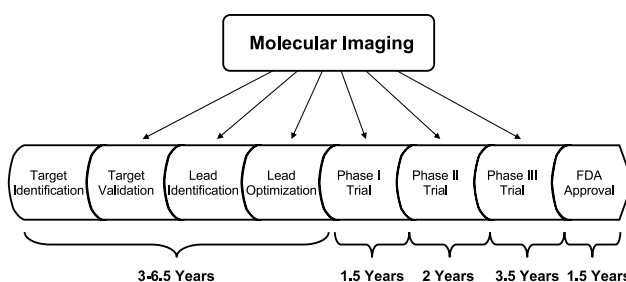


**Figure 1.** Drug development is a relatively long process, which usually spans 10 to 15 years. Molecular imaging can help in many steps of the process.

## Tumor Angiogenesis

Angiogenesis, the formation of new blood vessels from preexisting blood vessels, is a fundamental process occurring during tumor progression (7). Tumor growth depends on the balance between proangiogenic and antiangiogenic molecules. Molecules regulating angiogenesis include, but are not limited to, growth factor receptors, tyrosine kinase receptors, G-protein-coupled receptors for angiogenesis modulating proteins, integrins, and matrix metalloproteinases (MMP; ref. 8). Here, we will focus on three of the most intensively studied angiogenesis-related molecular targets: vascular endothelial growth factor (VEGF) and VEGF receptors (VEGFR), integrin  $\alpha_v\beta_3$ , and MMPs (Fig. 2). During tumor angiogenesis, these molecules interact closely with each other. Integrin  $\alpha_v\beta_3$  can recruit and activate MMP-2, which degrades components of the basement membrane and interstitial matrix to facilitate tumor progression (9). It can also regulate the production of VEGF in certain tumor cells (10). Several other molecular targets that are also involved in tumor angiogenesis are thus far understudied and will only be briefly mentioned, such as endoglin (CD105) and E-selectin (Fig. 2).

## Imaging VEGF and VEGFR Expression

VEGF is a potent mitogen in embryonic and somatic angiogenesis. It plays a central role in both normal vascular tissue development and tumor neovascularization (8). The VEGF family is comprised of seven members with a common VEGF homology domain: VEGF-A, VEGF-B, VEGF-C, VEGF-D, VEGF-E, VEGF-F, and placental growth factor. VEGF-A is a dimeric, disulfide-bound glycoprotein that exists in at least seven homodimeric isoforms, consisting of 121, 145, 148, 165, 183, 189, or 206 amino acids (11). These isoforms differ not only in their molecular weight but also in biological properties, such as the ability to bind to cell surface heparin sulfate proteoglycans.

The angiogenic actions of VEGF are mainly mediated via two closely related endothelium-specific receptor tyrosine kinases: Flt-1 (VEGFR-1) and Flk-1/KDR (VEGFR-2; ref. 12). Both are largely restricted to vascular endothelial cells and are overexpressed on the endothelium of tumor

vasculature, whereas they are almost undetectable in the vascular endothelium of adjacent normal tissues. All of the VEGF-A isoforms bind to both VEGFR-1 and VEGFR-2. It is generally agreed that VEGFR-1 is critical for physiologic and developmental angiogenesis, and the function of VEGFR-1 differs with the stages of development, the states of physiologic and pathologic conditions, and the cell types in which it is expressed (12). VEGFR-2 is the major mediator of the mitogenic, angiogenic, and permeability-enhancing effects of VEGF. Overexpression of VEGFR or VEGF-A has been implicated as poor prognostic markers in various clinical studies of cancer (13). Agents that prevent VEGF-A binding to its receptors, antibodies that directly block VEGFR-2, and small molecules that inhibit the kinase activity of VEGFR-2 thereby blocking VEGF/VEGFR signaling are all under active development (14–16). The critical role of VEGF-A in cancer progression has been highlighted by the recent approval of the humanized anti-VEGF monoclonal antibody bevacizumab (Avastin; Genentech, South San Francisco, CA) for first-line treatment (17). Successful development of VEGF- or VEGFR-targeted molecular imaging could serve as a paradigm for the assessment of cancer therapeutics targeting tumor angiogenesis.

Recombinant human VEGF<sub>121</sub> has been labeled with <sup>111</sup>In for identification of ischemic tissue in a rabbit model, where unilateral hind limb ischemia was created by femoral artery excision (18). However, virtually no difference was observed between the ischemic hind limb and the contralateral hind limb. VEGF<sub>121</sub> has also been labeled with <sup>99m</sup>Tc through an "Adapter/Docking" strategy (19). The tracer was used to image 4T1 murine mammary carcinoma, and very low tumor signal (<3 %ID/g) was observed. Recently, this tracer was also tested for the imaging of tumor vasculature before and after different types of chemotherapy (20). [<sup>123</sup>I]VEGF<sub>165</sub> has also been reported as a potential tumor marker (21). Despite the high receptor affinity of this tracer, biodistribution in A2508 melanoma tumor-bearing mice indicated poor tumor-to-background ratio, most likely due to the low metabolic stability of the compound. Nonetheless, biodistribution, safety, and absorbed dose of [<sup>123</sup>I]VEGF<sub>165</sub> was studied in patients with pancreatic carcinoma (22). Following i.v. administration, sequential images were

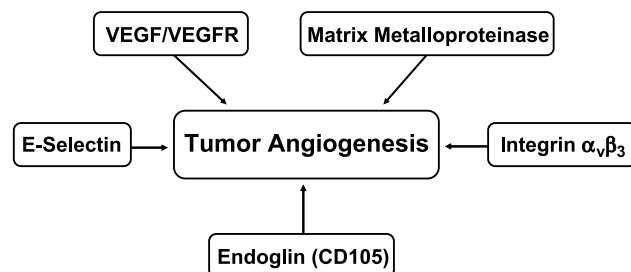


**Figure 2.** Representative molecular targets involved in tumor angiogenesis.

recorded during the initial 30 minutes after injection. Although a majority of primary pancreatic tumors and their metastases were visualized by [<sup>123</sup>I]VEGF<sub>165</sub> scan, the organ with the highest absorbed doses was the thyroid, indicating severe deiodination of the probe. A recombinant protein composed of VEGF<sub>165</sub> fused through a flexible polypeptide linker (GGGGS)<sub>3</sub> to the n-lobe of human transferrin was also reported for imaging angiogenesis, and the tumor contrast was modest (23). In all the above reports, radiolabeled VEGF isoforms were used for SPECT imaging. PET has several advantages over SPECT, including 1 to 2 orders of magnitude greater sensitivity, and the increasing implementation of clinical PET and PET/CT (computed tomography) scanners can facilitate the translation of novel PET tracers to the clinic.

A few radiolabeled anti-VEGF antibodies have been reported for PET imaging applications. VG76e, an IgG1 monoclonal antibody that binds to human VEGF, was labeled with <sup>124</sup>I for PET imaging of solid tumor xenografts in immunodeficient mice (24). Whole-animal PET imaging studies revealed a high tumor-to-background contrast (Fig. 3A). Although VEGF specificity *in vivo* was shown in this report, the poor immunoreactivity (<35%) of the radiolabeled antibody limits the potential use of this tracer. HuMV833, a humanized version of a mouse monoclonal anti-VEGF antibody MV833, was also labeled with <sup>124</sup>I, and the distribution and biological effects of HuMV833 in phase I trial cancer patients were investigated (25). Patients with progressive solid tumors were treated with various doses of HuMV833, and PET imaging using [<sup>124</sup>I]HuMV833 was carried out to measure the antibody distribution. It was found that antibody distribution and clearance were quite heterogeneous not only between patients but also between individual tumors of the same patient, suggesting that intra-patient dose escalation approaches or more precisely defined patient cohorts would be preferred in the design of phase I studies with antiangiogenic antibodies such as HuMV833.

We have recently labeled VEGF<sub>121</sub> with <sup>64</sup>Cu ( $t_{1/2} = 12.7$  hours) for PET imaging of tumor angiogenesis and VEGFR expression (26). DOTA-VEGF<sub>121</sub> (where DOTA denotes 1,4,7,10-tetraazacyclododecane-1,4,7,10-tetraacetic acid) exhibits nanomolar receptor binding affinity *in vitro*. MicroPET imaging revealed rapid, specific, and prominent uptake of [<sup>64</sup>Cu]DOTA-VEGF<sub>121</sub> in highly vascularized small U87MG tumor (high VEGFR-2 expression) but significantly lower and sporadic uptake in large U87MG tumor (low VEGFR-2 expression; Fig. 3B). Western blot of tumor tissue lysate, immunofluorescence staining, and blocking studies with unlabeled VEGF<sub>121</sub> confirmed that the *in vivo* tumor uptake is VEGFR specific. Substantial tracer uptake in the kidneys was also observed, most likely due to the high VEGFR-1 expression in this organ. Successful demonstration of the ability of [<sup>64</sup>Cu]DOTA-VEGF<sub>121</sub> to visualize VEGFR expression *in vivo* should allow for clinical translation of this tracer to image tumor angiogenesis and to guide antiangiogenic treatment, especially VEGFR-targeted cancer therapy. Based on the *in vivo* pharmacokinetics of [<sup>64</sup>Cu]DOTA-VEGF<sub>121</sub>, VEGF<sub>121</sub> may also be labeled with <sup>18</sup>F for PET imaging applications as good tumor-to-background ratio was achieved as early as 1 to 2 hours after injection.

The abovementioned examples showed that molecular imaging of tumor angiogenesis can play a role in target validation, lead optimization, monitoring therapeutic response, and in clinical trials during the drug development process. Despite the critical role of VEGF and VEGFR in tumor angiogenesis, molecular imaging of VEGF or VEGFR has not been well studied. In the clinical setting, the right timing can be critical for VEGFR-targeted cancer therapy, and PET imaging of VEGF/VEGFR can play a very important role in determining whether to start and when to start the VEGFR-targeted treatment. Clinical translation will be critical for the maximum benefit of VEGF-based cancer imaging agents. Much research remains to be done in the near future to optimize VEGF- or VEGFR-targeted

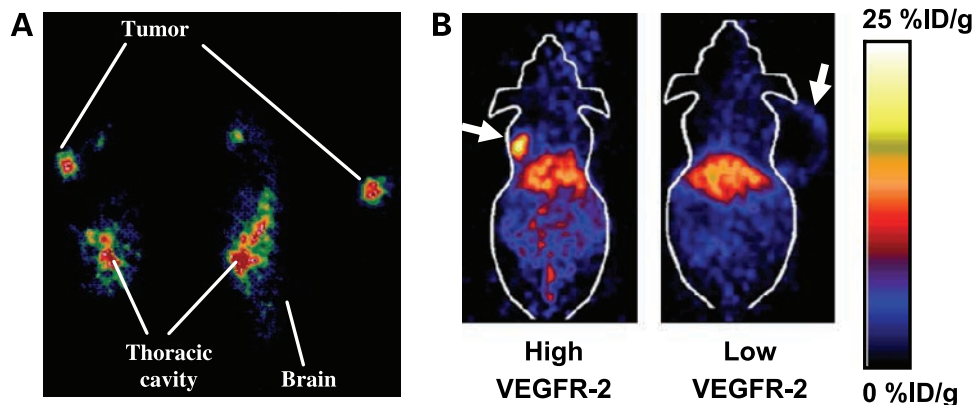


**Figure 3.** **A**, PET images of a tumor-bearing mouse at 24 h after injection of <sup>124</sup>I-labeled VG76e. Left to right, coronal, sagittal, and transverse views. **B**, microPET images of U87MG tumor-bearing mice 16 h after injection of [<sup>64</sup>Cu]DOTA-VEGF<sub>121</sub>. The small tumor has high VEGFR-2 expression, whereas the large tumor has low VEGFR-2 expression. %ID/g, percent injected dose per gram of tissue (adapted from refs. 24, 26).

molecular imaging. Site-specific labeling via a Cys-tag may offer advantage over direct labeling on the amino group of the lysine side chain for new tracer development or tracer optimization. A VEGFR-2-specific ligand can also be developed, which may be superior to VEGF-A-based tracer, as experimental evidence has shown that VEGFR-2 is more involved in tumor angiogenesis, whereas VEGF-A binds to both VEGFR-1 and VEGFR-2. Peptidic VEGFR antagonists, which can be labeled with  $^{11}\text{C}$  or  $^{18}\text{F}$  (more readily available than  $^{64}\text{Cu}$  or  $^{124}\text{I}$ ), may also be tested (27). Peptide-based tracers may allow for higher throughput than antibody- or protein-based radiotracers, as 1-hour after injection is usually sufficient for a peptide-based tracer to clear from the non-targeted organs and give high-contrast PET images. In contrast, it may take several hours and even days before high-contrast PET images can be obtained for protein- or antibody-based tracer. Transgenic mouse models where either the VEGF or VEGFR-2 promoter drives reporter gene expression will also likely play a useful role in understanding VEGF biology and drug optimization (28).

As VEGF/VEGFR signaling is one of the most important pathways during tumor angiogenesis, the ability to image and quantify VEGF and/or VEGFR expression level during tumor growth and upon antiangiogenic treatment will be of critical importance. It has been shown that the therapeutic window of VEGF/VEGFR-targeted delivery does not depend on the total dose given but rather on the microenvironmental levels of VEGF/VEGFR expression. Visualizing and quantifying VEGF/VEGFR expression *in vivo* will allow for personalized treatment by choosing the right timing during which the treatment is most effective. *In vivo* imaging of VEGF/VEGFR expression will also be able to determine the effective dose of VEGF/VEGFR-based treatment, so that therapeutically efficacious dose levels can be given safely.

### Imaging Integrin $\alpha_v\beta_3$ Expression

Integrins are a family of cell adhesion molecules consisting of two noncovalently bound transmembrane subunits ( $\alpha$  and  $\beta$ ), both type I membrane proteins with large extracellular segments that pair to create heterodimers with distinct adhesive capabilities (29). In mammals, 18  $\alpha$  and 8  $\beta$  subunits assemble into 24 different receptors. Integrin signaling plays a key role in tumor angiogenesis and metastasis (30). Integrins expressed on endothelial cells modulate cell migration and survival during angiogenesis, whereas integrins expressed on carcinoma cells potentiate metastasis by facilitating invasion and movement across blood vessels. The  $\alpha_v\beta_3$  integrin, which binds to arginine-glycine-aspartic acid (RGD)-containing components of the interstitial matrix, is significantly up-regulated on endothelium during angiogenesis but not on quiescent endothelium (30, 31). Inhibition of  $\alpha_v\beta_3$  integrin activity by monoclonal antibodies, cyclic RGD peptide antagonists, and peptidomimetics has been shown to induce endothelial cell apoptosis, to inhibit angiogenesis, and to increase endothelial monolayer permeability (32).

Crystal structure of the extracellular portion of integrin  $\alpha_v\beta_3$  in complex with c(RGDf(NMe)V) has been reported (31, 33). The cyclic RGD peptide binds at the major interface between the  $\alpha_v$  and  $\beta_3$  subunits and makes extensive contacts with both in a transition metal (e.g.,  $\text{Mn}^{2+}$ )-dependent mode. Preclinical studies indicated that many integrins other than  $\alpha_v\beta_3$  also play important roles in regulating angiogenesis, such as  $\alpha_1\beta_1$ ,  $\alpha_2\beta_1$ ,  $\alpha_4\beta_1$ ,  $\alpha_5\beta_1$ ,  $\alpha_6\beta_4$ ,  $\alpha_{IIb}\beta_3$ , and  $\alpha_v\beta_5$  (32). Among all 24 integrins discovered to date, integrin  $\alpha_v\beta_3$  is the most intensively studied, and an extensive review on multimodality molecular imaging of integrin  $\alpha_v\beta_3$  has recently been published (34).

### Non-Radionuclide-Based Imaging of Integrin $\alpha_v\beta_3$ Expression

Antibody-coated paramagnetic liposomes (35), Gd-perfluorocarbon nanoparticles conjugated to anti-integrin  $\alpha_v\beta_3$  monoclonal antibody (36), and integrin  $\alpha_v\beta_3$ -targeted paramagnetic nanoparticles (37) have been reported for magnetic resonance imaging of integrin  $\alpha_v\beta_3$  expression (Fig. 4A). In these studies, the targeted paramagnetic nanoparticles are coated with either antibodies or small peptidic/peptidomimetic integrin  $\alpha_v\beta_3$  antagonists. Because of the relatively large size of the probes (200–700 nm), these agents target the integrin  $\alpha_v\beta_3$  expressed on the tumor vasculature rather than the tumor cells. Ultrasound imaging using integrin  $\alpha_v\beta_3$ -targeted microbubbles has also been reported (Fig. 4B; ref. 38). Because acoustic destruction of "payload-bearing" microbubbles can be used to deliver drugs or to augment gene transfection (39), integrin  $\alpha_v\beta_3$ -targeted microbubbles may have applications in site-specific cancer therapy. Further studies are needed to validate the potential therapeutic applications.

Although optical imaging may not be widely used in clinical settings, near-IR (700–900 nm) approaches provide opportunities for rapid and cost-effective preclinical evaluation in small animal models before the more costly radionuclide-based imaging studies. These approaches may also be translated into the clinic with fluorescence-mediated tomography (e.g., for breast cancer imaging). In the near-IR region, the absorbance of all biomolecules reaches minima, providing a clear window for *in vivo* optical imaging (40). We have shown that near-IR fluorescent dye or quantum dot-conjugated cyclic RGD peptide could be used to visualize s.c. inoculated integrin  $\alpha_v\beta_3$ -positive tumors (41, 42). The dye-RGD peptide conjugate is small in size; therefore, it targets integrin  $\alpha_v\beta_3$  on both tumor cells and tumor vasculature (Fig. 4C). For the quantum dot-RGD peptide conjugate, it mainly targets integrin  $\alpha_v\beta_3$  in the tumor vasculature because it does not extravasate well due to the relatively large size ( $\geq 20$  nm; Fig. 4D). Based on these results, an approach that takes advantage of the high integrin  $\alpha_v\beta_3$ -targeting efficacy of the cyclic RGD peptides, high stability and brightness of quantum dots, and emission wavelength in the near-IR window will have great potential

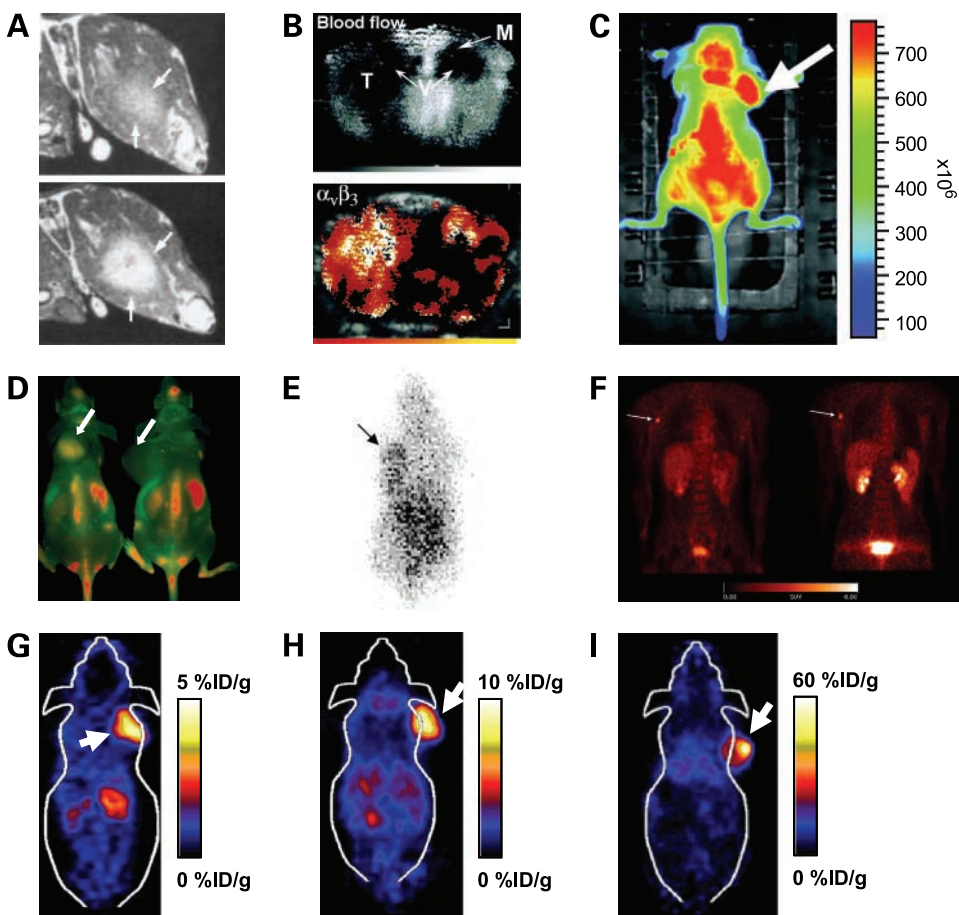


**Figure 4.** **A**, magnetic resonance images of an i.m. tumor before (top) and after (bottom) administration of integrin  $\alpha_v\beta_3$ -targeted liposomes. **B**, contrast-enhanced ultrasound images of a tumor-bearing rat depicting parametric perfusion data (top) and signal enhancement from integrin  $\alpha_v\beta_3$ -targeted microbubbles (bottom). *T*, tumor; *V*, ventricles; *M*, a periventricular metastasis. **C**, *in vivo* near-IR fluorescence imaging of s.c. U87MG tumor-bearing mice 1 h after administration of RGD-Cy5.5 conjugate. **D**, *in vivo* near-IR fluorescence imaging of U87MG tumor-bearing mice injected with quantum dot-RGD conjugate (*left*) or equal amount of unconjugated quantum dot (*right*). **E**, scintigraphic image of an ovarian carcinoma tumor-bearing mouse 2 h after administration of an [<sup>111</sup>In]-labeled dimeric RGD peptide. **F**, a patient with malignant melanoma stage IIIb and a solitary lymph node metastasis in the right axilla was visualized by both [<sup>18</sup>F]FDG (*left*) and [<sup>18</sup>F]galacto-RGD (*right*). **G**, coronal microPET image of a U87MG tumor-bearing mouse 70 min after administration of [<sup>18</sup>F]FRGD2. **H**, coronal microPET image of a U87MG tumor-bearing mouse 1 h after administration of [<sup>64</sup>Cu]DOTA-E[c(RGDfK)]<sub>2</sub>. **I**, coronal microPET image of a U87MG tumor-bearing mouse 25 h after administration of [<sup>64</sup>Cu]DOTA-Abegrin. The tumors are shown with arrows in all cases (adapted from refs. 35, 38, 41, 42, 45, 50, 55, 60, 61).

in cancer diagnosis and imaging as well as imaging-guided surgery and therapy.

Recently, Achilefu et al. (43) discovered that conjugating a presumably inactive linear hexapeptide GRDSPK with a near-IR carbocyanine molecular probe yielded Cyp-RGD that targets integrin  $\alpha_v\beta_3$ -positive tumors. More experiments need to be carried out to fully understand this surprising phenomenon, and docking study may reveal whether Cyp-RGD actually binds to the RGD binding domain in integrin  $\alpha_v\beta_3$ . Later, they synthesized and evaluated a series of multimeric RGD compounds constructed on a dicarboxylic acid-containing near-IR fluorescent dye cypate for tumor targeting (44). Optimization of the spatial alignment of the RGD moieties through careful molecular design and library construction may induce multivalent ligand-receptor interactions

useful for *in vivo* tumor imaging and tumor-targeted therapy.

### SPECT/PET Imaging of Integrin $\alpha_v\beta_3$ Expression

RGD peptides have been labeled with <sup>111</sup>In and <sup>99m</sup>Tc for SPECT imaging of integrin  $\alpha_v\beta_3$  expression. The *in vivo* behavior of radiolabeled dimeric RGD peptide E[c(RGDfK)]<sub>2</sub> was studied in an ovarian carcinoma xenograft model (45). <sup>111</sup>In/<sup>99m</sup>Tc were incorporated through DOTA and hydrazinonicotinamide (HYNIC) chelators, respectively (Fig. 4E). RP748, an <sup>111</sup>In-labeled quinolone that binds to integrin  $\alpha_v\beta_3$  with high affinity, was recently studied both *in vitro* and *in vivo* to track injury-induced vascular proliferation in rodents (46). Water-soluble *N*-(2-hydroxypropyl)methacrylamide copolymers have

been synthesized with pending doubly cyclized RGD peptides (47). The bioactivity of the polymer conjugates and free peptides was characterized both *in vitro* and *in vivo*. It was shown that specific targeting of  $\alpha_v\beta_3$  integrin and nonspecific vascular permeability both contributed significantly to the tumor uptake, with specific targeting being more important. It was concluded that peptide oligomers may be more suitable for imaging purposes because of the rapid clearance, whereas peptide-polymer conjugates may be used for high-level targeting and radiotherapeutic approaches.

PET has been the mainstay of integrin  $\alpha_v\beta_3$  expression imaging, and most reports focus on the radiolabeling of RGD peptide antagonists. Monomeric RGD peptide c(RGDyV) was first labeled with  $^{125}\text{I}$  by Haubner et al. (48). A glycopeptide based on c(RGDfK) was later labeled with  $^{18}\text{F}$  via a 2-[ $^{18}\text{F}$ ]fluoropropionate prosthetic group, and the resulting [ $^{18}\text{F}$ ]galacto-RGD exhibited integrin  $\alpha_v\beta_3$ -specific tumor uptake in integrin-positive M21 melanoma xenograft model (49). Initial clinical trials in healthy volunteers and a limited number of cancer patients revealed that this tracer can be safely given to patients and is able to delineate certain lesions that are integrin positive (Fig. 4F; ref. 50). Despite the successful translation of [ $^{18}\text{F}$ ]galacto-RGD into clinical trials, several key issues remain to be resolved, such as tumor-targeting efficacy, pharmacokinetics, and the ability to quantify integrin  $\alpha_v\beta_3$  density *in vivo*.

We have labeled a series of RGD peptides with  $^{18}\text{F}$  for PET imaging, using PEGylation and polyvalency to improve the tumor-targeting efficacy and pharmacokinetics (51–56). [ $^{18}\text{F}$ ]FB-E[c(RGDyK)]<sub>2</sub> (abbreviated as [ $^{18}\text{F}$ ]FRGD2) had predominant renal excretion and almost twice as much tumor uptake in the same animal model compared with the monomeric tracer [ $^{18}\text{F}$ ]FB-c(RGDyK) (Fig. 4G; refs. 54, 55). The synergistic effect of polyvalency and improved pharmacokinetics may be responsible for the excellent imaging characteristics of [ $^{18}\text{F}$ ]FRGD2. Graphical analyses of the dynamic microPET scans in six tumor xenograft models were carried out to correlate the tumor uptake with integrin  $\alpha_v\beta_3$  expression level measured by SDS-PAGE autoradiography, and excellent linear correlation was observed. More importantly, it was found that at late time points when most of the nonspecific binding had been cleared, the tumor/background ratio had a linear relationship with tumor integrin  $\alpha_v\beta_3$  expression level, thus making it possible to quantify integrin  $\alpha_v\beta_3$  density *in vivo*. We are currently in the process of translating [ $^{18}\text{F}$ ]FRGD2 into the clinic for cancer patient imaging.

In addition to  $^{18}\text{F}$ ,  $^{64}\text{Cu}$ -labeled RGD peptides are also of considerable interest. Copper-64 is an attractive radionuclide for both PET imaging and targeted radiotherapy of cancer. PET imaging of tumors with low doses of  $^{64}\text{Cu}$ -labeled RGD peptides may be used to determine radiation dosimetry before therapy with high dose of  $^{64}\text{Cu}$ - or  $^{67}\text{Cu}$ -labeled RGD peptides. We have labeled RGD peptides with  $^{64}\text{Cu}$  for PET imaging, again using PEGylation and polyvalency to optimize the tumor-targeting efficacy and

pharmacokinetics (53, 57–59). Recently, we reported a tetrameric RGD peptide-based tracer, [ $^{64}\text{Cu}$ ]DOTA-E[E[c(RGDfK)]<sub>2</sub>]<sub>2</sub>, which showed significantly higher receptor binding affinity than the corresponding monomeric and dimeric RGD analogues (60). This tracer exhibited rapid blood clearance, high metabolic stability, predominant renal excretion, significant receptor-mediated tumor uptake, and good contrast in xenograft-bearing mice (Fig. 4H). The high integrin avidity and favorable biokinetics makes [ $^{64}\text{Cu}$ ]DOTA-E[E[c(RGDfK)]<sub>2</sub>]<sub>2</sub> a promising agent for peptide receptor radionuclide imaging as well as targeted internal radiotherapy of integrin  $\alpha_v\beta_3$ -positive tumors.

Abegrin (MEDI-522, also called Vitaxin; MedImmune, Inc., Gaithersburg, MD), a humanized monoclonal antibody against human integrin  $\alpha_v\beta_3$  (picomolar binding affinity), is in clinical trials for cancer therapy. We have conjugated Abegrin with macrocyclic chelating agent DOTA and labeled it with  $^{64}\text{Cu}$  for PET imaging of tumor xenografts (61). MicroPET studies revealed that [ $^{64}\text{Cu}$ ]DOTA-Abegrin had very high tumor uptake in integrin  $\alpha_v\beta_3$ -positive U87MG tumor (Fig. 4I). The receptor specificity of [ $^{64}\text{Cu}$ ]DOTA-Abegrin was confirmed by effective blocking of tumor uptake with coadministration of nonradioactive Abegrin. The success of integrin  $\alpha_v\beta_3$ -specific tumor imaging using [ $^{64}\text{Cu}$ ]DOTA-Abegrin may be translated into the clinic to characterize the pharmacokinetics, tumor-targeting efficacy, dose optimization, and dose interval of Abegrin and/or Abegrin conjugates. Chemotherapeutics or radiotherapeutics using Abegrin as the delivering vehicle may also be effective in treating integrin  $\alpha_v\beta_3$ -positive tumors.

Integrin  $\alpha_v\beta_3$  is one of the most extensively studied molecular targets involved in tumor angiogenesis (30–34). The numerous reports on multimodality molecular imaging of integrin  $\alpha_v\beta_3$  again showed that tumor angiogenesis imaging can participate in multiple stages of the drug development process, such as target validation, lead optimization, and clinical trials. However, to date, only [ $^{18}\text{F}$ ]galacto-RGD has advanced into clinical settings for further testing, and the tracer itself is probably suboptimal (62). Polyvalent integrin  $\alpha_v\beta_3$  antagonists, such as multimeric RGD peptides, are also promising ligands for the molecular targeting of integrins involved in tumor angiogenesis. Translation of new multimeric RGD peptide-based tracers into the clinic will dramatically benefit antiangiogenic cancer therapy based on integrin  $\alpha_v\beta_3$  antagonism. The ability to quantify integrin  $\alpha_v\beta_3$  expression level *in vivo* will be very important in monitoring antiangiogenic treatment efficacy. Some of the abovementioned tracers with high integrin  $\alpha_v\beta_3$ -positive tumor uptake, as shown by molecular imaging studies, may also have the potential to evolve into radioimmunotherapy agents for cancer therapy.

### Imaging MMP Expression

MMPs are a family of  $\text{Zn}^{2+}$ -dependent endopeptidases, which play important roles in tumor angiogenesis, in

particular the 72-kDa (MMP-2) and 92-kDa (MMP-9) gelatinases (63). MMP-2, capable of degrading type IV collagen (major component of the basement membranes), can be localized in a proteolytically active form on the surface of invasive cancer cells based on its ability to bind to integrin  $\alpha_v\beta_3$  (9). A number of MMP inhibitors (MMPI) have been developed as cytostatic and antiangiogenic agents and are currently in clinical testing (64). Until recently, clinical trials with MMPIs have yielded disappointing results, highlighting the need for better insight into the mechanisms by which MMPs contribute to tumor growth. Molecular imaging to monitor MMP expression noninvasively *in vivo* will be critical for future drug development targeting MMPs.

Molecular imaging of MMP expression, as well as imaging of other enzymes, can be divided into two approaches. In the “targeted” probes approach, labeled small molecules, peptides, metabolites, aptamers, antibodies, or other molecules are injected i.v., and the living systems can be imaged when a fraction of the agent has bound to its target and the non-bound agent has been cleared. Non-peptidyl broad-spectrum MMPIs, tissue inhibitors of metalloproteinases, MMP-2-specific inhibitors, carboxylic and hydroxamic acid-based MMPIs, selective inhibitors of MMP-2/MMP-9, and other MMPIs have been labeled with  $^{123}\text{I}$ ,  $^{125}\text{I}$ ,  $^{111}\text{In}$ ,  $^{99m}\text{Tc}$ ,  $^{11}\text{C}$ ,  $^{18}\text{F}$ , and/or  $^{64}\text{Cu}$  for *in vivo* biological and clinical investigation of MMP expression using SPECT and PET (65–72). However, in most of the reports, selective binding of the labeled compounds to specific MMPs was not shown, and high nonspecific binding was observed possibly due to low *in vivo* stability of the tracers. Except for one most recent report (Fig. 5A; ref. 71), none of the abovementioned reports showed any convincing *in vivo* imaging results. The cyclic decapeptide CTTHWGFTLC, a selective MMP-2 and MMP-9 inhibitor, was conjugated with DOTA and labeled with  $^{64}\text{Cu}$  for PET imaging of MMP expression in xenograft models. Zymography of tumor extracts supported the *in vivo* PET imaging results. MMP-2 and MMP-9 bands were clearly detectable in the mouse imaged at 7 weeks, which had prominent tumor uptake, whereas the MMP-2 and MMP-9 expression was very weak afterwards, which gave low tumor uptake (Fig. 5A). However, MMP expression in the MDA-MB-435 tumor model used in this study had quite large individual variance. The low *in vivo* stability of the radiotracer also limits further application of this strategy.

The abovementioned approach based on affinity ligands is usually more useful for imaging receptors and cell surface-expressed molecules, but it may not be the best approach for imaging enzyme function in a living organism. Another approach is the use of “activatable probes.” Activatable probes undergo chemical or physicochemical changes on target interaction and result in signal amplification. This approach was first shown by Bremer et al. where MMP activity was imaged in live animals, and that the inhibition of MMP activity can be recorded within hours after treatment by a potent MMPI (Fig. 5B; refs. 73, 74). Later, similar approaches were used for imaging MMP expression in the heart after myocardial

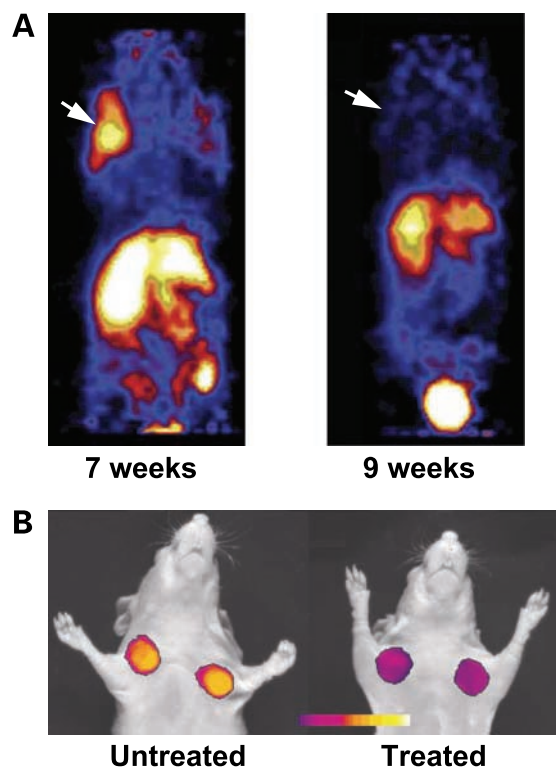


**Figure 5.** **A**, microPET imaging of a  $^{64}\text{Cu}$ -labeled MMP-2/MMP-9 inhibitor in MDA-MB-435 breast tumor-bearing mice at 7 wks (left, where MMP-2/MMP-9 expression is clearly detectable by zymography) and 9 wks (right, where MMP-2/MMP-9 expression is not detectable by zymography) after inoculation. **B**, *in vivo* near-IR fluorescence imaging of tumor-bearing mice using an activatable probe before (left) and after (right) prinomastat (a MMPI) treatment (adapted from refs. 71, 74).

infarction where an near-IR fluorescent probe was activated upon proteolytic cleavage by MMP-2 and MMP-9 (75). In another report, cellular association of polyarginine-based cell-penetrating peptides is effectively blocked when they are fused to an inhibitory domain composed of negatively charged residues, which was called “activatable cell-penetrating peptides” (76). Cleavage of the MMP-sensitive linker between the polycationic and polyanionic domains releases the cell-penetrating peptide portion and its attached cargo to bind to and enter cells. In xenograft tumor models expressing MMP-2/MMP-9, a fluorescent dye Cy5-conjugated activatable cell-penetrating peptide showed modest *in vivo* tumor contrast (2- to 3-fold when compared with contralateral normal tissue). The similar approach has also been applied to modulate the cellular uptake of quantum dot conjugates (77). Another fluorogenic activatable probe, which is MMP-7 selective, has been reported for *in vivo* detection and imaging of tumor-associated MMP-7 activity (78). Although the activatable probe strategy may give good tumor/background contrast, the major drawback of optical imaging is that it has limited clinical applications.

*In vivo* imaging of MMP expression is still underdeveloped due to many issues. First, the expression level of

MMPs varies during different stages of tumor progression, and imaging may also be complicated by naturally occurring tissue inhibitors of metalloproteinases. Second, specificity for one particular MMP is hard to achieve. There is still plenty of room for improving the selectivity between different MMPs, especially MMP-2 and MMP-9. The experimental outcome would be much better interpreted if the ligand is specific for one particular MMP. Third, quantifying the MMP expression level *in vivo* has not been demonstrated. The imaging results reported thus far are mostly qualitative. The ability of correlating the MMP imaging result with the MMP expression *in vivo* will dramatically help the advancement of MMP imaging, anti-MMP drug screening, and monitoring of treatment efficacy.

### Imaging Endoglin and E-Selectin

*In vivo* imaging of endothelial markers in intact tumor neovasculature can significantly help assessing the efficacy of antiangiogenic agents in clinical trials. Although many endothelial markers have been described, only few of them have been evaluated as imaging markers. Endoglin (CD105) is emerging as a prime vascular target for antiangiogenic cancer therapy (79). It is a cell membrane glycoprotein mainly expressed on endothelial cells and overexpressed on tumor vasculature. It functions as an accessory component of the transforming growth factor- $\beta$  receptor complex and is involved in vascular development and remodeling. Avidin-coated microbubbles have been linked to biotinylated monoclonal antibodies for endoglin targeting *in vitro* (80).  $^{125}\text{I}$ -labeled monoclonal antibody MAEND3 has been reported to target CD105 on tumor vasculature in canine models (81). Another radiolabeled monoclonal anti-endoglin antibody has also been used for *in vivo* imaging (82). The major advantage of imaging abundantly expressed endothelial targets is that this strategy circumvents delivery barriers normally associated with other tumor-targeting strategies.

E-selectin is a cell adhesion molecule and CD antigen that mediates neutrophil, monocyte, and memory T-cell adhesion to cytokine-activated endothelial cells (83). It is expressed exclusively by activated endothelial cells, and it recognizes sialylated carbohydrate groups related to the Lewis X or Lewis A family. Fluorescence reflectance imaging (a photographic process that captures views of a surface under varying lighting conditions to enhance surface detail that may otherwise be difficult to see) of E-selectin expression in mouse xenograft models of Lewis lung carcinoma has been reported (84). The imaging probe was constructed by conjugating an E-selectin-binding peptide (CDS DSDITWDQLWDL MK) to CLIO(Cy5.5) nanoparticles, where CLIO represents cross-linked iron oxide that can be used for magnetic resonance imaging.

Endostatin, which binds fibulin and nidogen, is a 20-kDa COOH-terminal fragment of collagen XVIII, and it is a potent naturally occurring inhibitor of angiogenesis (7). It has been labeled with a fluorescent dye Cy5.5 for tumor localization after i.p. injection (85). Endostatin-Cy5.5 was quickly

absorbed after administration, producing a near-IR fluorescence image of the tumors that persisted through 7 days.  $[^{99\text{m}}\text{Tc}]$ ethylenedicycysteine-endostatin has also been synthesized for evaluating the efficacy of antiangiogenic therapy (86). Tissue distribution and planar imaging of radiolabeled endostatin were determined in tumor-bearing rats. It was claimed that  $[^{99\text{m}}\text{Tc}]$ ethylenedicycysteine-endostatin could assess treatment response, and there was a correlation between tumor uptake and cellular targets expression level.

### Conclusions and Perspectives

Significant advances have been made in developing novel probes for multimodality molecular imaging of tumor angiogenesis. Small molecules, peptides, peptidomimetics, proteins, and antibodies have been labeled with radioisotopes, superparamagnetic nanoparticles, fluorescent dyes, quantum dots, and microbubbles for PET, SPECT, magnetic resonance imaging, near-IR fluorescence, and ultrasound imaging of small animal tumor models, a few of which are now in early clinical trials. The major roles of tumor angiogenesis imaging in the drug development process will be the following: target identification, characterization, and validation; patient stratification (e.g., selecting the right population of cancer patients for new clinical trials); pharmacokinetic/pharmacodynamic studies (e.g., candidate drug screening and optimization, phase I clinical trials); as well as treatment monitoring and dose optimization (phase II/III trials). Through the development of a robust tumor angiogenesis imaging platform, molecular imaging can dramatically facilitate and speed up many steps of antiangiogenic drug development in both the preclinical and clinical stages.

Despite the strong potentials of angiogenesis imaging probes, most of the research efforts have thus far been limited to probe optimization for enhanced tumor-targeting efficacy and improved *in vivo* kinetics. The translation of the imaging probes from bench to bedside has been slow. The limited margins for marketing the very special probes makes some of *de novo* imaging approaches considered too risky by investigators. The situation is, however, being improved. Food and Drug Administration recently developed exploratory Investigational New Drug mechanism to allow faster first-in-human studies. Microdosing studies with novel imaging probes can provide an opportunity for early assessment of the safety profile and pharmacokinetics in healthy volunteers. Such rapid initial clinical studies will definitely accelerate the drug discovery process. Furthermore, the molecular imaging field has grown extremely fast over the last decade, and the value of molecular imaging in drug development and screening is more widely accepted by pharmaceutical companies. By repeated imaging in preclinical models using one or more of the discussed imaging strategies, one can have several readouts of angiogenesis before and after drug administration. Even if the drug target is different from the imaging target, one can still use imaging as a potential surrogate for the efficacy of the drug at a given dose. It is expected that in the foreseeable future molecular imaging will be routinely applied in many steps of the drug development process. The combination of

molecular and anatomic/functional imaging techniques in assessing tumor angiogenesis and in the response to antiangiogenic cancer therapy will be a powerful tool.

To foster the continued discovery and development of angiogenesis-targeted imaging probes, cooperative efforts are needed from cellular/molecular biologists to identify and validate molecular imaging targets, chemists/radiochemists to synthesize and characterize the imaging probes, and medical physicists/mathematicians to develop high-sensitivity/high-resolution imaging devices/hybrid instruments and to develop better algorithms to further improve signal-to-noise ratio of a given imaging device. Close partnerships among academic researchers, clinicians, pharmaceutical industries, the National Cancer Institute, and the Food and Drug Administration are also needed to promote further development of imaging probes, to apply molecular/functional imaging approaches to predict and evaluate antiangiogenic effect during and after treatment, to move molecular imaging guided intervention strategy quickly into the clinic, and to accelerate antiangiogenic drug development.

## References

- Gwyther SJ. New imaging techniques in cancer management. *Ann Oncol* 2005;16 Suppl 2:ii63–70.
- Rudin M, Weissleder R. Molecular imaging in drug discovery and development. *Nat Rev Drug Discov* 2003;2:123–31.
- Massoud TF, Gambhir SS. Molecular imaging in living subjects: seeing fundamental biological processes in a new light. *Genes Dev* 2003;17:545–80.
- Seddon BM, Workman P. The role of functional and molecular imaging in cancer drug discovery and development. *Br J Radiol* 2003;76 Spec No 2:S128–38.
- Wang J, Maurer L. Positron emission tomography: applications in drug discovery and drug development. *Curr Top Med Chem* 2005;5:1053–75.
- Czernin J, Weber WA, Herschman HR. Molecular imaging in the development of cancer therapeutics. *Annu Rev Med* 2006;57:99–118.
- Bergers G, Benjamin LE. Tumorigenesis and the angiogenic switch. *Nat Rev Cancer* 2003;3:401–10.
- Ferrara N. VEGF and the quest for tumour angiogenesis factors. *Nat Rev Cancer* 2002;2:795–803.
- Brooks PC, Stromblad S, Sanders LC, et al. Localization of matrix metalloproteinase MMP-2 to the surface of invasive cells by interaction with integrin  $\alpha_v\beta_3$ . *Cell* 1996;85:683–93.
- De S, Razorenova O, McCabe NP, O'Toole T, Qin J, Byzova TV. VEGF-integrin interplay controls tumor growth and vascularization. *Proc Natl Acad Sci U S A* 2005;102:7589–94.
- Ferrara N. The role of VEGF in the regulation of physiological and pathological angiogenesis. *EXS* 2005;209–31.
- Hicklin DJ, Ellis LM. Role of the vascular endothelial growth factor pathway in tumor growth and angiogenesis. *J Clin Oncol* 2005;23:1011–27.
- Ferrara N. Vascular endothelial growth factor: basic science and clinical progress. *Endocr Rev* 2004;25:581–611.
- Sun J, Wang DA, Jain RK, et al. Inhibiting angiogenesis and tumorigenesis by a synthetic molecule that blocks binding of both VEGF and PDGF to their receptors. *Oncogene* 2005;24:4701–9.
- Prewett M, Huber J, Li Y, et al. Antivascular endothelial growth factor receptor (fetal liver kinase 1) monoclonal antibody inhibits tumor angiogenesis and growth of several mouse and human tumors. *Cancer Res* 1999;59:5209–18.
- Wedge SR, Ogilvie DJ, Dukes M, et al. ZD4190: an orally active inhibitor of vascular endothelial growth factor signaling with broad-spectrum antitumor efficacy. *Cancer Res* 2000;60:970–5.
- Middleton G, Lapka DV. Bevacizumab (Avastin). *Clin J Oncol Nurs* 2004;8:666–9.
- Lu E, Wagner WR, Schellenberger U, et al. Targeted *in vivo* labeling of receptors for vascular endothelial growth factor: approach to identification of ischemic tissue. *Circulation* 2003;108:97–103.
- Blankenberg FG, Mandl S, Cao YA, et al. Tumor imaging using a standardized radiolabeled adapter protein docked to vascular endothelial growth factor. *J Nucl Med* 2004;45:1373–80.
- Blankenberg FG, Backer MV, Levashova Z, Patel V, Backer JM. *In vivo* tumor angiogenesis imaging with site-specific labeled  $^{99m}\text{Tc}$ -HYNIC-VEGF. *Eur J Nucl Med Mol Imaging* 2006;33:841–8.
- Cornelissen B, Oltenfreiter R, Kersmans V, et al. *In vitro* and *in vivo* evaluation of [ $^{123}\text{I}$ ]-VEGF<sub>165</sub> as a potential tumor marker. *Nucl Med Biol* 2005;32:431–6.
- Li S, Peck-Radosavljevic M, Kienast O, et al. Iodine-123-vascular endothelial growth factor-165 ( $^{123}\text{I}$ -VEGF<sub>165</sub>). Biodistribution, safety and radiation dosimetry in patients with pancreatic carcinoma. *Q J Nucl Med Mol Imaging* 2004;48:198–206.
- Chan C, Sandhu J, Guha A, et al. A human transferrin-vascular endothelial growth factor (hnTf-VEGF) fusion protein containing an integrated binding site for  $^{111}\text{In}$  for imaging tumor angiogenesis. *J Nucl Med* 2005;46:1745–52.
- Collingridge DR, Carroll VA, Glaser M, et al. The development of [ $^{124}\text{I}$ ]iodinated-VG76e: a novel tracer for imaging vascular endothelial growth factor *in vivo* using positron emission tomography. *Cancer Res* 2002;62:5912–9.
- Jayson GC, Zweit J, Jackson A, et al. Molecular imaging and biological evaluation of HuMV833 anti-VEGF antibody: implications for trial design of antiangiogenic antibodies. *J Natl Cancer Inst* 2002;94:1484–93.
- Cai W, Chen K, Mohamedali KA, et al. Positron emission tomography imaging of vascular endothelial growth factor receptor expression. *J Nucl Med*. In press 2006.
- Goncalves M, Estieu-Gionnet K, Berthelot T, et al. Design, synthesis, and evaluation of original carriers for targeting vascular endothelial growth factor receptor interactions. *Pharm Res* 2005;22:1411–21.
- Wang Y, Iyer M, Annala A, Wu L, Carey M, Gambhir SS. Noninvasive indirect imaging of vascular endothelial growth factor gene expression using bioluminescence imaging in living transgenic mice. *Physiol Genomics* 2006;24:173–80.
- Ruoslahti E. RGD and other recognition sequences for integrins. *Annu Rev Cell Dev Biol* 1996;12:697–715.
- Hood JD, Cheresh DA. Role of integrins in cell invasion and migration. *Nat Rev Cancer* 2002;2:91–100.
- Xiong JP, Stehle T, Zhang R, et al. Crystal structure of the extracellular segment of integrin  $\alpha_v\beta_3$  in complex with an Arg-Gly-Asp ligand. *Science* 2002;296:151–5.
- Cai W, Chen X. Anti-angiogenic cancer therapy based on integrin  $\alpha_v\beta_3$  antagonism. *Anti-Cancer Agents Med Chem* 2006;6:407–28.
- Xiong JP, Stehle T, Diefenbach B, et al. Crystal structure of the extracellular segment of integrin  $\alpha_v\beta_3$ . *Science* 2001;294:339–45.
- Cai W, Gambhir SS, Chen X. Multimodality tumor imaging targeting integrin  $\alpha_v\beta_3$ . *Biotechniques* 2005;39:S6–17.
- Sipkins DA, Cheresh DA, Kazemi MR, Nevin LM, Bednarski MD, Li KC. Detection of tumor angiogenesis *in vivo* by  $\alpha_v\beta_3$ -targeted magnetic resonance imaging. *Nat Med* 1998;4:623–6.
- Anderson SA, Rader RK, Westlin WF, et al. Magnetic resonance contrast enhancement of neovasculature with  $\alpha_v\beta_3$ -targeted nanoparticles. *Magn Reson Med* 2000;44:433–9.
- Winter PM, Caruthers SD, Kassner A, et al. Molecular imaging of angiogenesis in nascent Vx-2 rabbit tumors using a novel  $\alpha_v\beta_3$ -targeted nanoparticle and 1.5 tesla magnetic resonance imaging. *Cancer Res* 2003;63:5838–43.
- Ellegala DB, Leong-Poi H, Carpenter JE, et al. Imaging tumor angiogenesis with contrast ultrasound and microbubbles targeted to  $\alpha_v\beta_3$ . *Circulation* 2003;108:336–41.
- Shohet RV, Chen S, Zhou YT, et al. Echocardiographic destruction of albumin microbubbles directs gene delivery to the myocardium. *Circulation* 2000;101:2554–6.
- Frangioni JV. *In vivo* near-infrared fluorescence imaging. *Curr Opin Chem Biol* 2003;7:626–34.

- 41.** Chen X, Conti PS, Moats RA. *In vivo* near-infrared fluorescence imaging of integrin  $\alpha_v\beta_3$  in brain tumor xenografts. *Cancer Res* 2004;64:8009–14.
- 42.** Cai W, Shin DW, Chen K, et al. Peptide-labeled near-infrared quantum dots for imaging tumor vasculature in living subjects. *Nano Lett* 2006;6:669–76.
- 43.** Achilefu S, Bloch S, Markiewicz MA, et al. Synergistic effects of light-emitting probes and peptides for targeting and monitoring integrin expression. *Proc Natl Acad Sci U S A* 2005;102:7976–81.
- 44.** Ye Y, Bloch S, Xu B, Achilefu S. Design, synthesis, and evaluation of near infrared fluorescent multimeric RGD peptides for targeting tumors. *J Med Chem* 2006;49:2268–75.
- 45.** Janssen ML, Oyen WJ, Dijkgraaf I, et al. Tumor targeting with radiolabeled  $\alpha_v\beta_3$  integrin binding peptides in a nude mouse model. *Cancer Res* 2002;62:6146–51.
- 46.** Sadeghi MM, Krassilnikova S, Zhang J, et al. Detection of injury-induced vascular remodeling by targeting activated  $\alpha_v\beta_3$  integrin *in vivo*. *Circulation* 2004;110:84–90.
- 47.** Line BR, Mitra A, Nan A, Ghandehari H. Targeting tumor angiogenesis: comparison of peptide and polymer-peptide conjugates. *J Nucl Med* 2005;46:1552–60.
- 48.** Haubner R, Wester HJ, Reuning U, et al. Radiolabeled  $\alpha_v\beta_3$  integrin antagonists: a new class of tracers for tumor targeting. *J Nucl Med* 1999;40:1061–71.
- 49.** Haubner R, Wester H-J, Weber WA, et al. Noninvasive imaging of  $\alpha_v\beta_3$  integrin expression using <sup>18</sup>F-labeled RGD-containing glycopeptide and positron emission tomography. *Cancer Res* 2001;61:1781–5.
- 50.** Haubner R, Weber WA, Beer AJ, et al. Noninvasive visualization of the activated  $\alpha_v\beta_3$  integrin in cancer patients by positron emission tomography and [<sup>18</sup>F]galacto-RGD. *PLoS Med* 2005;2:e70.
- 51.** Chen X, Park R, Hou Y, et al. MicroPET imaging of brain tumor angiogenesis with <sup>18</sup>F-labeled PEGylated RGD peptide. *Eur J Nucl Med Mol Imaging* 2004;31:1081–9.
- 52.** Chen X, Park R, Shahinian AH, et al. <sup>18</sup>F-labeled RGD peptide: initial evaluation for imaging brain tumor angiogenesis. *Nucl Med Biol* 2004;31:179–89.
- 53.** Chen X, Park R, Tohme M, Shahinian AH, Bading JR, Conti PS. MicroPET and autoradiographic imaging of breast cancer  $\alpha_v$ -integrin expression using <sup>18</sup>F- and <sup>64</sup>Cu-labeled RGD peptide. *Bioconjug Chem* 2004;15:41–9.
- 54.** Chen X, Tohme M, Park R, Hou Y, Bading JR, Conti PS. Micro-PET imaging of  $\alpha_v\beta_3$ -integrin expression with <sup>18</sup>F-labeled dimeric RGD peptide. *Mol Imaging* 2004;3:96–104.
- 55.** Zhang X, Xiong Z, Wu X, et al. Quantitative PET imaging of tumor integrin  $\alpha_v\beta_3$  expression with <sup>18</sup>F-FRGD2. *J Nucl Med* 2006;47:113–21.
- 56.** Cai W, Zhang X, Wu Y, Chen X. A thiol-reactive <sup>18</sup>F-labeling agent, *N*-[2-(4-18F-fluorobenzamido)ethyl]maleimide (<sup>18</sup>F-FBEM), and the synthesis of RGD peptide-based tracer for PET imaging of  $\alpha_v\beta_3$  integrin expression. *J Nucl Med* 2006;47:1172–80.
- 57.** Chen X, Hou Y, Tohme M, et al. Pegylated Arg-Gly-Asp peptide: <sup>64</sup>Cu labeling and PET imaging of brain tumor  $\alpha_v\beta_3$ -integrin expression. *J Nucl Med* 2004;45:1776–83.
- 58.** Chen X, Liu S, Hou Y, et al. MicroPET imaging of breast cancer  $\alpha_v$ -integrin expression with <sup>64</sup>Cu-labeled dimeric RGD peptides. *Mol Imaging Biol* 2004;6:350–9.
- 59.** Chen X, Sievers E, Hou Y, et al. Integrin  $\alpha_v\beta_3$ -targeted imaging of lung cancer. *Neoplasia* 2005;7:271–9.
- 60.** Wu Y, Zhang X, Xiong Z, et al. MicroPET imaging of glioma  $\alpha_v$ -integrin expression using <sup>64</sup>Cu-labeled tetrameric RGD peptide. *J Nucl Med* 2005;46:1707–18.
- 61.** Cai W, Wu Y, Chen K, Cao Q, Tice DA, Chen X. *In vitro* and *in vivo* characterization of <sup>64</sup>Cu-labeled Abegrin<sup>®</sup>, a humanized monoclonal antibody against integrin  $\alpha_v\beta_3$ . *Cancer Res* 2006;66:9673–81.
- 62.** Haubner R.  $\alpha_v\beta_3$ -integrin imaging: a new approach to characterise angiogenesis? *Eur J Nucl Med Mol Imaging* 2006;33 Suppl 13:54–63.
- 63.** Egeblad M, Werb Z. New functions for the matrix metalloproteinases in cancer progression. *Nat Rev Cancer* 2002;2:161–74.
- 64.** Overall CM, Lopez-Otin C. Strategies for MMP inhibition in cancer: innovations for the post-trial era. *Nat Rev Cancer* 2002;2:657–72.
- 65.** Breyholz HJ, Schafers M, Wagner S, et al. C-5-disubstituted barbiturates as potential molecular probes for noninvasive matrix metalloproteinase imaging. *J Med Chem* 2005;48:3400–9.
- 66.** Furumoto S, Takashima K, Kubota K, Ido T, Iwata R, Fukuda H. Tumor detection using <sup>18</sup>F-labeled matrix metalloproteinase-2 inhibitor. *Nucl Med Biol* 2003;30:119–25.
- 67.** Giersing BK, Rae MT, CarballidoBrea M, Williamson RA, Blower PJ. Synthesis and characterization of <sup>111</sup>In-DTPA-N-TIMP-2: a radiopharmaceutical for imaging matrix metalloproteinase expression. *Bioconjug Chem* 2001;12:964–71.
- 68.** Kopka K, Breyholz HJ, Wagner S, et al. Synthesis and preliminary biological evaluation of new radioiodinated MMP inhibitors for imaging MMP activity *in vivo*. *Nucl Med Biol* 2004;31:257–67.
- 69.** Medina OP, Kairemo K, Vaitanen H, et al. Radionuclide imaging of tumor xenografts in mice using a gelatinase-targeting peptide. *Anticancer Res* 2005;25:33–42.
- 70.** Oltenfreiter R, Staelens L, Lejeune A, et al. New radioiodinated carboxylic and hydroxamic matrix metalloproteinase inhibitor tracers as potential tumor imaging agents. *Nucl Med Biol* 2004;31:459–68.
- 71.** Sprague JE, Li WP, Liang K, Achilefu S, Anderson CJ. *In vitro* and *in vivo* investigation of matrix metalloproteinase expression in metastatic tumor models. *Nucl Med Biol* 2006;33:227–37.
- 72.** Zheng QH, Fei X, Liu X, et al. Synthesis and preliminary biological evaluation of MMP inhibitor radiotracers [<sup>11</sup>C]methyl-halo-CGS 27023A analogs, new potential PET breast cancer imaging agents. *Nucl Med Biol* 2002;29:761–70.
- 73.** Bremer C, Bredow S, Mahmood U, Weissleder R, Tung CH. Optical imaging of matrix metalloproteinase-2 activity in tumors: feasibility study in a mouse model. *Radiology* 2001;221:523–9.
- 74.** Bremer C, Tung CH, Weissleder R. *In vivo* molecular target assessment of matrix metalloproteinase inhibition. *Nat Med* 2001;7:743–8.
- 75.** Chen J, Tung CH, Allport JR, Chen S, Weissleder R, Huang PL. Near-infrared fluorescent imaging of matrix metalloproteinase activity after myocardial infarction. *Circulation* 2005;111:1800–5.
- 76.** Jiang T, Olson ES, Nguyen QT, Roy M, Jennings PA, Tsien RY. Tumor imaging by means of proteolytic activation of cell-penetrating peptides. *Proc Natl Acad Sci U S A* 2004;101:17867–72.
- 77.** Zhang Y, So MK, Rao J. Protease-modulated cellular uptake of quantum dots. *Nano Lett* 2006;6:1988–92.
- 78.** McIntyre JO, Fingleton B, Wells KS, et al. Development of a novel fluorogenic proteolytic beacon for *in vivo* detection and imaging of tumour-associated matrix metalloproteinase-7 activity. *Biochem J* 2004;377:617–28.
- 79.** Fonsatti E, Altomonte M, Nicotra MR, Natali PG, Maio M. Endoglin (CD105): a powerful therapeutic target on tumor-associated angiogenetic blood vessels. *Oncogene* 2003;22:6557–63.
- 80.** Korpany G, Grayburn PA, Shohet RV, Brekken RA. Targeting vascular endothelium with avidin microbubbles. *Ultrasound Med Biol* 2005;31:1279–83.
- 81.** Fonsatti E, Jekunen AP, Kairemo KJ, et al. Endoglin is a suitable target for efficient imaging of solid tumors: *in vivo* evidence in a canine mammary carcinoma model. *Clin Cancer Res* 2000;6:2037–43.
- 82.** Bredow S, Lewin M, Hofmann B, Marcos E, Weissleder R. Imaging of tumour neovasculature by targeting the TGF- $\beta$  binding receptor endoglin. *Eur J Cancer* 2000;36:675–81.
- 83.** Laferriere J, Houle F, Huot J. Regulation of the metastatic process by E-selectin and stress-activated protein kinase-2/p38. *Ann N Y Acad Sci* 2002;973:562–72.
- 84.** Funovics M, Montet X, Reynolds F, Weissleder R, Josephson L. Nanoparticles for the optical imaging of tumor E-selectin. *Neoplasia* 2005;7:904–11.
- 85.** Citrin D, Scott T, Sproull M, Menard C, Tofilon PJ, Camphausen K. *In vivo* tumor imaging using a near-infrared-labeled endostatin molecule. *Int J Radiat Oncol Biol Phys* 2004;58:536–41.
- 86.** Yang DJ, Kim KD, Schechter NR, et al. Assessment of antiangiogenic effect using <sup>99m</sup>Tc-EC-endostatin. *Cancer Biother Radiopharm* 2002;17:233–45.

# Multimodality Imaging of Tumor Integrin $\alpha_v\beta_3$ Expression

Xiaoyuan Chen\*

*Molecular Imaging Program at Stanford (MIPS), Department of Radiology, Stanford University, Stanford, CA 94305, USA*

**Abstract:** Most solid tumors are angiogenesis dependent. Anti-angiogenic pharmaceuticals that inhibit the growth of new blood vessels offer considerable promise as anti-cancer agents. With increasing numbers of anti-angiogenic drugs in clinical trials, there is an urgent need for detailed characterization of the heterogeneity of tumor vasculature and dissection of the complex network of mechanisms that control tumor angiogenesis. Non-invasive molecular imaging will play a key role in individualized anti-angiogenic therapy based upon molecular features of the new blood vessel growth. Integrin  $\alpha_v\beta_3$ , which binds several ligands via an RGD tripeptide sequence, is uniquely expressed in tumor vasculature and aggressive tumor cells, making it a potential target for anti-angiogenic interventions. This review highlights some recent advances in multimodality imaging of tumor integrin expression with emphasis on positron emission tomography (PET).

**Keywords:** tumor angiogenesis, molecular imaging, integrin  $\alpha_v\beta_3$ , RGD peptide, positron emission tomography (PET).

## TUMOR ANGIOGENESIS

Angiogenesis, the formation of new blood vessels from preexisting vasculature, is essential for tumor growth and progression (for a review, see REF. [1]). Without neovascularization, cells in prevascular tumors or metastases that may be replicating rapidly reach equilibrium with their rate of death. Inhibition of angiogenesis has been shown to prevent tumor growth and even to cause tumor regression in various experimental models [2]. In contrast to traditional chemotherapies, which non-specifically target all dividing cells, anti-angiogenic therapy selectively targets activated endothelial cells and tumor cells. In early Phase I/II clinical trials, angiogenic modulators have shown modest toxic effects and are mainly cytostatic, slowing or stopping the tumor growth and the development of metastasis, producing an objective remission [3] (see <http://www.angiogenesis.org> or <http://cancernet.nci.nih.gov> for a detailed list of agents in development).

Angiogenesis is a complex process involving extensive interplay between cells, soluble factors, and extracellular matrix (ECM) components [1]. The construction of a vascular network requires different sequential steps including the release of proteases from “activated” endothelial cells with subsequent degradation of basement membrane surrounding the existing vessel, migration of endothelial cells into the interstitial space, endothelial cell proliferation, and differentiation into mature blood vessels. These processes are mediated by a wide range of angiogenic inducers, including growth factors, chemokines, angiogenic enzymes, endothelial specific receptors, and adhesion molecules [4]. Each of these processes presents the possible targets for possible diagnostic and therapeutic interventions.

## ANATOMICAL/FUNCTIONAL IMAGING OF TUMOR ANGIOGENESIS

Because tumor size monitoring is still an important clinical indicator for oncologists, conventional imaging techniques will likely remain useful to follow anti-angiogenic treatment efficacy. These techniques can also be adapted to visualize and quantify morphological and functional changes associated with tumor vascularity. Computed tomography (CT) imaging can be performed with contrast agents to define the intravascular compartment, including blood flow, blood volume, mean fluid transit time, and capillary permeability [5]. Perfusion CT technique can be easily incorporated into the existing CT protocols to delineate increases in tissue perfusion that may reflect malignancy, even when there is no gross anatomical abnormality present [6]. Depiction and detection of tumor vascularity with ultrasound can be either approached by Doppler studies to delineate large and medium-sized vessels or by microbubble contrast enhanced agents to detect microvasculature [7]. Magnetic resonance imaging (MRI) can define both blood volume and blood vessel permeability using dynamic enhancement of blood pool contrast agents. Gadolinium-DTPA can distinguish between normal (non-leaky) versus malignant (leaky) tissues, reflecting the hyperpermeable tumor vasculature. Dynamic MRI used in combination with macromolecular contrast media and kinetic modeling can be applied to monitor changes in the tumor microvasculature such as transendothelial permeability or fractional plasma volume [8,9]. Positron emission tomography (PET) is another approach used to characterize neoplastic tissue. Fluorodeoxyglucose (FDG) labeled with positron emitter  $^{18}\text{F}$  ( $t_{1/2} = 109.7$  min) can be used to localize primary tumors and distal metastases and to characterize tumor glucose metabolism [10]. Blood flow and blood volume can also be detected with  $\text{H}_2^{15}\text{O}$  and  $^{11}\text{CO}$ , respectively [11].

\*Address correspondence to this author at the Xiaoyuan Chen, PhD, Molecular Imaging Program at Stanford (MIPS), Department of Radiology, Stanford University, 1201 Welch Rd P095, Stanford, CA 94305-5484, USA; Tel: 650)725-0950; Fax: 650)736-7925; E-mail: shawchen@stanford.edu

## MOLECULAR IMAGING OF TUMOR INTEGRIN EXPRESSION

Targeting tumor angiogenesis by conventional imaging modalities that detect anatomical and functional changes of tumor vascularity during tumor growth, angiogenesis, and upon anti-angiogenic treatment have been well-documented. These approaches, however, provide little or no information regarding the specific molecular markers on newly formed blood vessels and tumor cells and the molecular changes

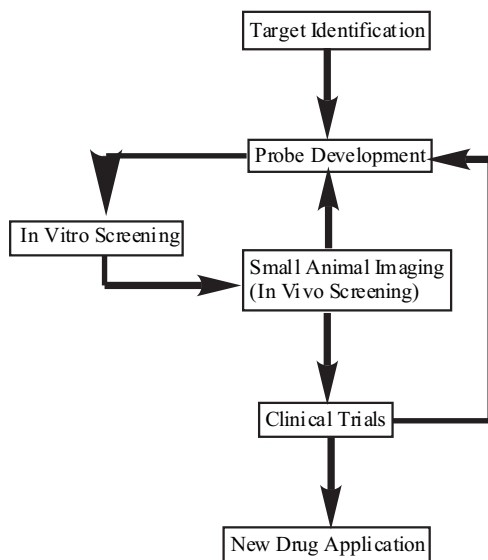


**Fig. (1).** Molecular Imaging is a novel multidisciplinary field involving the efforts from molecular and cell biology to identify the molecular imaging target, radiochemistry and bioconjugation chemistry to develop suitable imaging probes, pharmacology to optimize the probes for optimal targeting efficacy and favorable *in vivo* kinetics, and signal capture/image reconstruction techniques to non-invasively monitor the fate of molecular imaging probes *in vivo*. Once a molecular imaging target (mRNA or protein) is identified and validated (the target is required to have unique expression on the tumor cells as compared to normal organs and tissues and enough number of copies to be detectable by molecular imaging devices and to provide enough tumor/background contrast), effort will then be spent to develop molecular imaging probes for test (a more detailed description for molecular imaging probe development is shown in (Fig. 2)). The probe will then be applied to preclinical animal models for lesion detection (typically microPET or microSPECT). The tumor targeting efficacy and *in vivo* kinetics will determine whether the probe will be further evaluated. If small animal imaging demonstrates that the molecular probe has good target specific tumor uptake and favorable *in vivo* kinetic profiles, the probe will then be rapidly translated into clinical applications since the features of miniaturized small animal imaging studies closely reflect the settings of a clinical imaging study for human beings. Satisfactory clinical trials for the New Investigational Drug (IND) will enable the submission of New Drug Application (NDA) to the Division of Medical Imaging and Radiopharmaceutical Drug Research, FDA for approval. If the probe fails to provide high tumor-to-background ratio, further structure-activity relationship (SAR) studies will be performed to optimize the molecular imaging probes.

upon therapy. The evolution of molecular imaging [12,13] takes advantage of traditional diagnostic imaging techniques and introduces molecular imaging probes to determine the expression of indicative molecular markers of the tumor angiogenesis process [14,15] (A detailed depiction of molecular imaging probe development is illustrated in Fig. 1).

For a targeting approach aimed at monitoring tumor angiogenesis, the accessible targets that are specific for the tumor present at a sufficient level are a prerequisite for the lesion to be detectable and to be delineated from the background by imaging technologies. The cell adhesion molecule integrin  $\alpha_v\beta_3$  [16], which is over-expressed on both tumor cells and tumor vasculature, is an excellent molecular marker for tumor angiogenesis imaging. Interactions between vascular cells and extracellular matrixes (ECMs) are involved in the multiple steps of angiogenesis. To date, four families of cell adhesion molecules have been described: integrins, immunoglobulin superfamily members, cadherins, and selectins. Members of each family have been detected in angiogenic blood vessels, with integrins being most well-studied. Adhesion receptors of the integrin family are responsible for a wide range of cell-ECM and cell-cell interactions. Each integrin consists of non-covalently associated  $\alpha$  and  $\beta$  subunits, both type I membrane proteins with large extracellular segments that pair to create heterodimers ( $\alpha\beta$ ) with distinct adhesive capabilities. In mammals, 18  $\alpha$  and 8  $\beta$  subunits assemble into 24 different receptors. The function of integrins during angiogenesis has been studied most extensively with  $\alpha_v\beta_3$ , which is not readily detectable in quiescent vessels but becomes highly expressed in angiogenic vessels [17]. The expression of integrin adhesion molecule  $\alpha_v\beta_3$  on sprouting capillary cells and their interaction with specific matrix ligands has been shown to play a key role in angiogenesis and metastasis. Integrins expressed on endothelial cells modulate cell migration and survival during angiogenesis. Integrins expressed on carcinoma cells potentiate metastasis by facilitating invasion and movement across blood vessels. Inhibition of  $\alpha_v$  integrin activity by mAbs, cyclic RGD peptide antagonists, and peptidomimetics has been shown to induce endothelial apoptosis, to inhibit angiogenesis, and to increase endothelial monolayer permeability [18].

The ability to non-invasively visualize and quantify  $\alpha_v\beta_3$  integrin expression level will provide new opportunities to document tumor (tumor cells and sprouting tumor vasculature) receptor expression, more appropriately select patients considered for anti-integrin treatment and monitor treatment efficacy in integrin-positive patients (General procedure for molecular imaging probe development is described in (Fig. 2)). Contrast enhanced ultrasound with microbubbles targeted to  $\alpha_v\beta_3$  integrins expressed on the neovascular endothelium has been used to image tumor integrin status in addition to tumor microvascular blood volume and blood velocity, which can be easily detected with non-targeted microbubbles [19]. In an animal model, Sipkins *et al.* [20] recently demonstrated that it is feasible to image  $\alpha_v\beta_3$  expression using MRI and antibody-coated paramagnetic liposomes. Due to the unfavorable physical characteristics of mAbs (vascularization requirements, and barriers to antibody penetration, as well as intratumoral pressure) and low sensitivity of MRI, targeted MR imaging

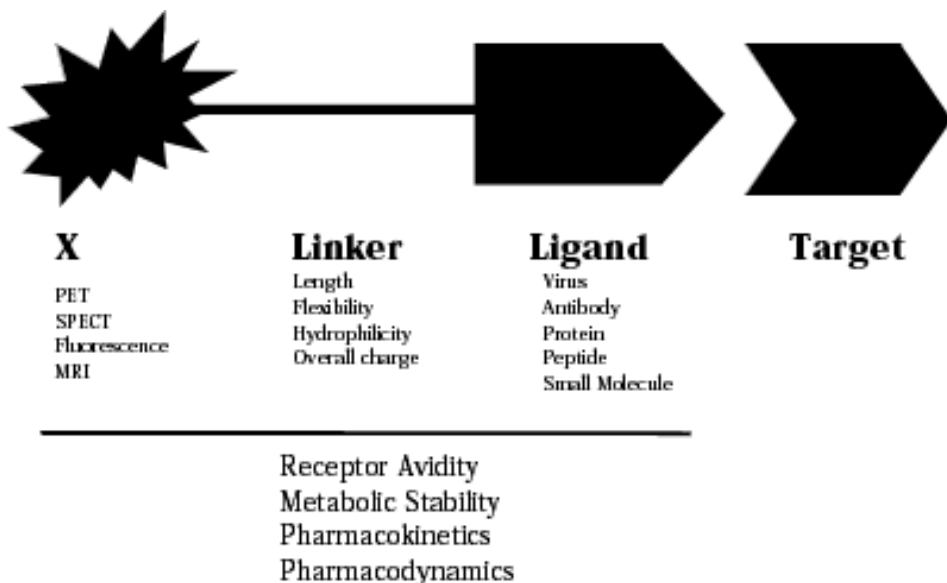


**Fig. (2).** A molecular imaging probe is often comprised of three parts: the target delivery vehicle (virus particles, monoclonal antibody, bispecific antibody or antibody fragments, proteins, peptides, or small molecule agonists/antagonists), the moiety (radionuclides for PET or SPECT, fluorescent dye for optical imaging or paramagnetic metal ion for MRI) that can be detected by an external imaging device, and a pharmacokinetic modifying (PKM) linker tethering the two together (there are exceptions if a PKM linker is not present, for example, isotopic substitution of a small molecule drug). Even though a target is validated, several factors are yet to be defined to determine whether a molecular imaging probe can be successfully applied for visualization and efficient quantification of the target, namely, receptor binding affinity and specificity, hydrophilicity, metabolic stability, overall molecular charge, molecular size, and the fate of metabolites.

will face significant obstacles to provide a robust platform for tumor integrin assessment. We and others [21,22] have also shown that near-infrared fluorescent dye conjugated cyclic RGD peptide was able to visualize subcutaneously inoculated integrin positive tumors. The major drawback of this approach is the limited penetration of light through tissue that this modality has primarily been directed towards near surface lesions that are accessible by light. Even though optical imaging may not be easily translated into human studies, this approach provides opportunities for rapid and cost-effective preclinical evaluation in animal models before the more costly radionuclide-based imaging studies. To date, most of the studies have been focused on developing suitably radiolabeled small RGD peptide antagonists of  $\alpha_v$ -integrin as radiopharmaceuticals for single-photon emission computed tomography (SPECT) and positron emission tomography (PET) imaging applications [23]. Due to the higher sensitivity of PET ( $10^{-11} - 10^{-12}$  M) as compared with SPECT ( $10^{-9}-10^{-10}$  M), the acquisition of higher count statistics is particularly valuable for detecting the fewest possible cells per unit volume with the least amount of radioactivity [24], development of probes for PET imaging of integrin expression has been the mainstay of the continued effort.

### PET IMAGING OF TUMOR INTEGRIN $\alpha_v\beta_3$

The crystal structures of extracellular segment of  $\alpha_v\beta_3$  and its complex with a potent cyclic RGD peptide, c(RGDf<sub>n</sub>NMe)V (Cilengitide, Merck, Inc., currently under Phase II clinical trials for patients with glioblastoma multiforme who have failed first-line chemotherapy) indicate that RGD binding site of the  $\alpha_v\beta_3$  integrin is located in the

deep cleft between the two subunits [25,26]. The essential arginine-glycine-aspartic acid (RGD) sequence in this specific bent conformation is desirable for high affinity and specific binding of the peptide ligand with integrin  $\alpha_v\beta_3$ . Substitution of the amino acid in position 4 (D-Phe in lead structure) with tyrosine allows electrophilic radiohalogenation (e.g.,  $^{123}\text{I}$ ,  $^{124}\text{I}$ ,  $^{125}\text{I}$ , and  $^{131}\text{I}$ ). Replacement of the amino acid in position 5 with lysine offers a further alternative for radiolabeling by derivatization of the side-chain  $\alpha$ -amino group. The lead compound c(RGDyK) was thus first labeled with  $^{125}\text{I}$  and the tracer revealed high receptor specific tumor uptake in integrin positive tumors but also persistent localization of radioactivity in the kidney region, presumably due to the electrostatic interaction between the positively charged RGD peptide and the negatively charged surface of renal proximal tubular cells [27,28]. Modifying the peptide with a sugar [27,29] or a poly(ethylene glycol) (PEG) [27] moiety increased the hydrophilicity of the lead compound and neutralized the positive charge on the lysine residue.  $^{125}\text{I}$ -labeled galacto-RGD or PEGylated RGD thus had rapid blood clearance, substantially lowered renal uptake but also slightly decreased tumor uptake due to decreased receptor binding affinity upon derivatization.

Encouraged by the ability of sugar and poly(ethylene glycol) to improve *in vivo* kinetic profile of cyclic RGD peptides, both peptides were then labeled with  $^{18}\text{F}$  through a prosthetic group (( $\pm$ )-2-[ $^{18}\text{F}$ ]fluoropropionate ( $[^{18}\text{F}]FP$ ) for RGD-containing glycopeptide [30-32] and 4-[ $^{18}\text{F}$ ]fluorobenzoyl ( $[^{18}\text{F}]FB$ ) for PEGylated RGD peptide [33]). Both compounds had fast blood clearance (less than 0.1 % injected dose/gram (%ID/g) tissue was present as early

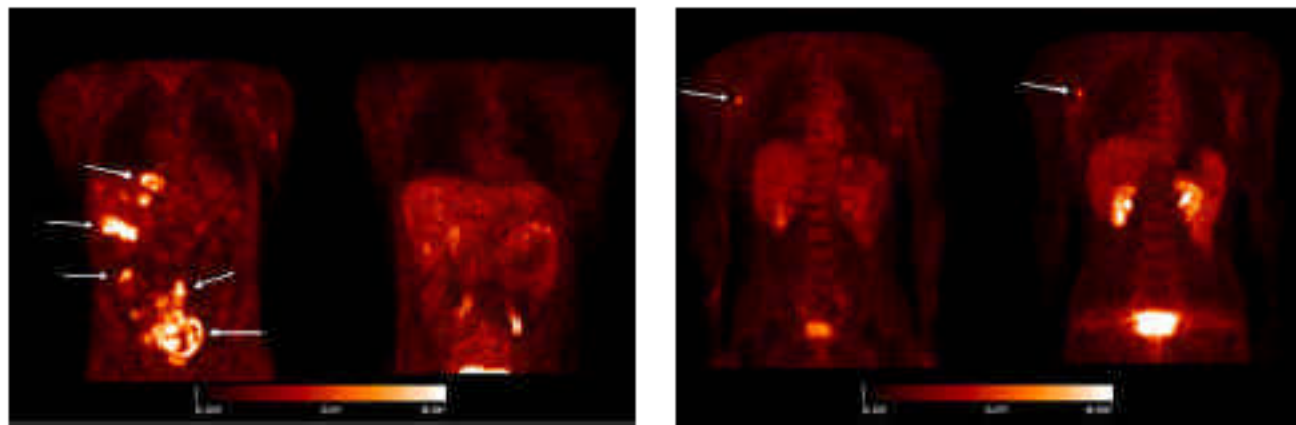


**Fig. (3).** (A) Schematic structure of  $[^{18}\text{F}]$ Galacto-RGD. Labeling with  $(\pm)$ -2- $[^{18}\text{F}]$ fluoropropionate group was carried out via acylation of the aminomethyl group at the C1-position of the sugar moiety (Adapted from Haubner *et al.*, ref. 30). (B) and (C), comparison of  $[^{18}\text{F}]$ FDG and  $[^{18}\text{F}]$ Galacto-RGD human scans. (B) A patient with malignant melanoma stage IV and multiple metastases in the liver, skin and lower abdomen (arrows) showed marked uptake of  $[^{18}\text{F}]$ FDG (left panel) but virtually no uptake of  $[^{18}\text{F}]$ Galacto-RGD (right panel). (C) A patient with malignant melanoma stage IIIb and a solitary lymph node metastasis in the right axilla can be detected by both  $[^{18}\text{F}]$ FDG (left panel) and  $[^{18}\text{F}]$ Galacto-RGD (right panel). The positive  $[^{18}\text{F}]$ FDG activity accumulation indicates viable tumor cells, whereas specific  $[^{18}\text{F}]$ Galacto-RGD peptide uptake represents integrin  $\alpha_v\beta_3$  positive tumor tissues. Although it is well documented in the literature that the expression of integrin  $\alpha_v\beta_3$  is associated with a high risk of metastasis and poor prognosis in melanoma [49], it is not well understood why angiogenesis is observed for the patient with malignant melanoma stage IIIb but not those with malignant stage IV and multiple metastases (Adapted from Haubner *et al.*, ref. 32).

as 2 h postinjection of radiotracer), rapid and high tumor uptake and moderate tumor washout, resulting in high tumor-to-background ratio and limited activity accumulation in the liver, kidneys and intestinal tracts. On the other hand, the parent RGD peptide when labeled with  $^{18}\text{F}$  through 4-[ $^{18}\text{F}$ ]fluorobenzoyl [34,35], showed tumor specific uptake and its activity accumulation is correlative with tumor integrin levels, however, the rapid tumor washout and unfavorable hepatobiliary excretion of this tracer limited its potential clinical applications. Pilot clinical trials are currently in progress to test the safety and efficacy of  $^{18}\text{F}$ -labeled glycosylated RGD monomer and to measure patient integrin expression levels [32] (Fig. 3).

The low molecular mass compound c(RGDyK) is optimized in size to fit the binding pocket of the  $\alpha_v\beta_3$  integrin receptor, thus introduction of any functional group to improve the *in vivo* kinetics is at the expense of a loss of receptor affinity. It has been proposed by several groups that the receptor binding characteristics of dimeric and multimeric RGD peptides would be better than that of monomeric RGD peptide based upon polyvalency [34,36-38]. The receptor binding of the one RGD peptide will significantly enhance the local concentration of the other RGD peptide in the vicinity of the receptor, which may lead to a faster rate of receptor binding or a slower rate dissociation of the radiolabeled dimeric RGD peptide. The dimeric RGD peptide with almost one order of magnitude higher integrin binding affinity than the monomeric analog is thus labeled with  $^{18}\text{F}$  [34, 38] and the tracer gave the highest tumor specific activity accumulation and tumor/background ratios at all time points examined as compared to monomeric RGD peptide tracers (unmodified [34,35], PEGylated [33], and glycosylated [34,36-38] RGDs) (Fig. 4).

For PET imaging of  $\alpha_v\beta_3$  expression,  $^{18}\text{F}$ -labeled RGD peptides will be the first choice since  $[^{18}\text{F}]$ F<sup>-</sup> is readily available from most medical cyclotron facilities and radiolabeling of peptides with  $^{18}\text{F}$  can be realized by introducing a prosthetic group. In addition to  $^{18}\text{F}$ ,  $^{64}\text{Cu}$ -labeled RGD peptides are of considerable interest because  $^{64}\text{Cu}$  ( $t_{1/2} = 12.8$  h;  $\beta^+ = 655$  keV [19%];  $\beta^- = 573$  keV [40%]) is an attractive radionuclide for both PET imaging and targeted radiotherapy of cancer [39]. PET imaging of tumors with low doses of  $^{64}\text{Cu}$ -labeled RGD peptides could also be utilized to determine individual radiation dosimetry prior to therapy with either  $^{64}\text{Cu}$ - or  $^{67}\text{Cu}$ -labeled RGD peptides.  $^{64}\text{Cu}$  labeling is also fairly straightforward and amenable for kit formulation. Further examples of PET imaging/internal radiotherapy radionuclide pairs include  $^{86}\text{Y}/^{90}\text{Y}$  [40] and  $^{124}\text{I}/^{131}\text{I}$  [41].

Generally speaking, the major problems with radiometal labeled peptides for tumor therapy include their rapid blood clearance thus not enough radiation dose being delivered to the tumor and unfavorable non-specific accumulation in non-tumor organs [42]. We initially coupled monomeric RGD peptide c(RGDyK) with macrocyclic chelator 1,4,7,10-tetraazacyclododecane-N,N',N'',N'''-tetraacetic acid (DOTA) and labeled the DOTA-RGD conjugate with  $^{64}\text{Cu}$  for breast cancer imaging [43]. The radiotracer showed intermediate tumor uptake but also prominent liver and kidney retention, suggesting both renal and hepatobiliary excretion routes. PEGylated monomeric RGD peptide when labeled with  $^{64}\text{Cu}$ , showed significantly reduced liver and intestinal uptake, reflecting favorable renal excretion of this tracer, with tumor targeting efficacy virtually unchanged [44]. A dimeric RGD peptide E[c(RGDyK)]<sub>2</sub> with higher integrin binding affinity when labeled with  $^{64}\text{Cu}$  indicated almost twice as high uptake in the tumor than the monomeric

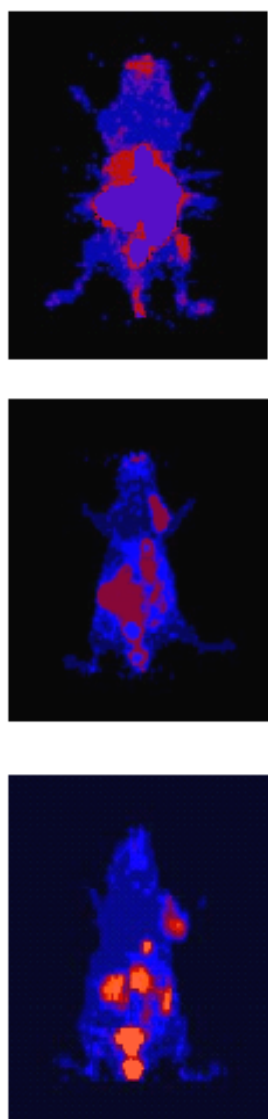


**Fig. (4).** This figure illustrates how a clinically applicable probe can be developed after identification of integrin  $\alpha_v\beta_3$  as the potential target for tumor angiogenesis imaging. Although, the initial compound [ $^{18}\text{F}$ ]FB-c(RGDyK) had a reasonably good receptor binding *in vitro* and tumor specific uptake *in vivo*, it had very rapid tumor washout and unfavorable hepatobiliary excretion, which makes detection of lesions in the lower abdomen very difficult. To increase the water solubility, a poly(ethylene glycol) (M.W. = 3,400) moiety as PKM linker was used to modify the tracer for *in vivo* evaluation. Indeed, the more hydrophilic tracers revealed better *in vivo* profile without compromising the tumor targeting efficacy *in vivo* even although the receptor binding affinity *in vitro* was lowered due to the PEGylation. A dimeric RGD peptide with higher binding affinity, molecular size and hydrophilicity was also labeled with  $^{18}\text{F}$ , the tumor uptake was almost twice as much as that of monomeric RGD peptide tracers, and the magnitude of tumor uptake was also positively correlated with tumor integrin density levels as examined in different tumor models. Two-dimensional (2D) projection images were acquired as 10 min static scans 60 min postinjection of 200  $\mu\text{Ci}$  of  $^{18}\text{F}$ -labeled RGD peptide tracer and reconstructed with ordered subset expectation maximization (OSEM) algorithm using microPET R4 system (Concorde Microsystems, Inc.).

analog, but also significantly higher renal activity accumulation presumably due to the fact that the dimeric RGD peptide tracer is more positively charged than the monomeric counterpart [34,37]. A tetrameric RGD peptide E{E[c(RGDyK)]<sub>2</sub>}<sub>2</sub> with even higher receptor affinity than the dimeric RGD peptide E[c(RGDyK)]<sub>2</sub> was labeled with  $^{64}\text{Cu}$  and applied to subcutaneous U87MG glioma model and found that the tracer had rapid liver and renal clearance, high and persistent tumor activity accumulation (e.g. tumor uptake was as high as 13 %ID/g at 2 h postinjection). This tracer may have the properties suitable for integrin targeted internal radiotherapeutic applications [45].

## FUTURE OUTLOOK

Up to now, most studies for imaging integrin receptor, a key player in tumor angiogenesis is still at the stage of imaging probe development. Systematic structure-activity relationship (SAR) studies are still needed to optimize the probes for optimal tumor targeting efficacy and improved *in vivo* kinetics for clinical trials. Furthermore, little has been done to correlate the magnitude of tumor uptake (combined receptor specific activity accumulation in the tumor cells and tumor vasculature) with integrin expression level. In other words, is the contrast obtained from non-invasive imaging a true reflection of tumor integrin levels? At any given time, the *in vivo* tumor signal is not only due to specific binding, but it also presents contributions from non-specific binding, free imaging probe in tissue, and intravascular activity. Tumor binding potential may be quantified through kinetic modeling of the dynamic microPET imaging data [46,47] and correlated with tumor integrin expression levels examined by traditional histopathological means.

Molecular imaging of tumor angiogenesis targeting at cell adhesion molecule integrin  $\alpha_v\beta_3$  may be designed to address the following aims (a schematic plot of the role of integrin expression imaging is illustrated in Fig. 5):

### 1). Lesion Detection

In spite of the clinical success with PET, [ $^{18}\text{F}$ ]FDG PET imaging has several limitations. The tracer can be non-specifically taken up by several benign conditions such as inflammatory disease, pneumonia, brown fat, muscle, bowel uptake, and granulomatous disease. Also, slow growing indolent tumors may exhibit only mildly increased glucose metabolism and therefore be missed by FDG PET [10]. As most tumor vasculature endothelial cells and many tumor cells express integrin  $\alpha_v\beta_3$ , suitably labeled RGD peptides might be a potentially more advantageous surrogate marker than FDG for early detection of some cancer types.

### 2). Patient Stratification

It is anticipated that there will be great variance in tracer accumulation in different tumor types, which indicates a great diversity in integrin receptor expression. This will indicate the importance of quantitative imaging of tumor integrin for patient stratification, allowing for appropriate selection of integrin positive patients entering clinical trials for anti-integrin treatment.

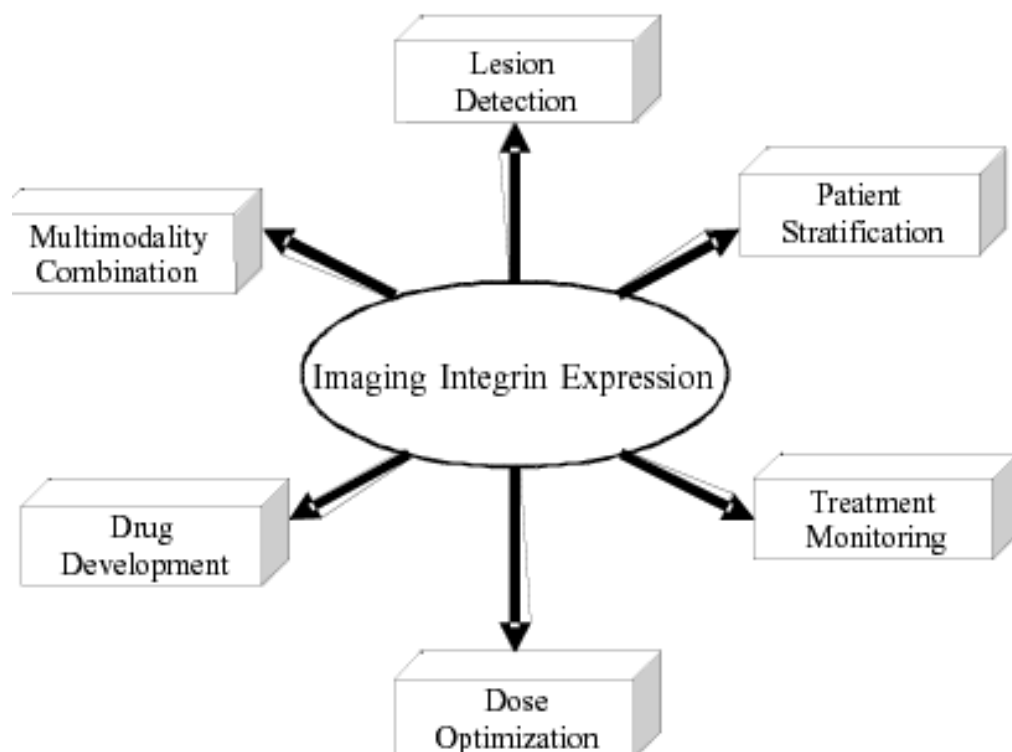


**Fig. (5).** Molecular imaging of tumor integrin expression may provide new insights into the mechanism of tumor angiogenesis and anti-angiogenic treatment efficacy in addition to simple lesion detection. RGD peptide based PET tracers are expected to supersede FDG for slowing growing tumors such as prostate cancer that exhibit only slightly increased glucose metabolism but have overexpressed integrin expression on both cells and tumor vessels. Quantitative visualization of tumor integrin can be used for patient stratification to accurately document  $\alpha_v\beta_3$  levels, this provides evidence for selecting appropriate patients into clinical trials for personalized anti-integrin treatment and to follow treatment efficacy. Receptor occupancy studies may also aid in dosage and dose interval selection for tailored dose optimization. Optimized probes for integrin imaging purpose may be easily adapted to develop new drugs for better tumor localization and retention with minimal non-specific accumulation. The same principle for integrin-based molecular imaging is applicable to molecular imaging in general.

### 3). Treatment

**Monitoring.** The intrinsic redundancy of signaling mechanisms associated with angiogenesis will lead to partial or complete resistance of the tumor vessel to therapy. Non-invasive visualization and quantification of tumor integrin levels may be applied to detect early response to anti-integrin treatment and help to elucidate the mechanisms of treatment efficacy underlying integrin signaling.

### 4). Dose Optimization

Using an established PET tracer for  $\alpha_v$ -integrin receptor expression imaging, one can expect to measure the degree to which administration of a peptide or antibody based integrin antagonist compete with the radiotracer/integrin binding. By this means, one can determine receptor binding potential as well as the percentage of receptor occupancy by administered drug when given in various doses and routes of administration. Furthermore, receptor occupancy studies as a function time after drug administration can be used to establish a favorable dosing interval for the cytostatic drug.

### 5). New Drug Development/Validation

*In vitro* receptor binding affinity and specificity may not directly reflect *in vivo* tumor receptor occupancy due to the

*in vivo* effects on binding kinetics. PET imaging in combination with radiolabeled RGD peptides might be a useful tool for studying structure-activity relationships for new anti-integrin drugs. Rapid characterization of pharmacokinetics and pharmacodynamics by *in vivo* imaging will inevitably improve data quality, reduce costs and animal numbers used and, most importantly, decrease the work-up for new compounds. The studies with microPET can be directly translated into clinical PET since the features of small animal PET imaging studies closely reflect the settings of clinical PET study for human beings.

### 6). Combination of Molecular and Functional Imaging

The combination of molecular and anatomical/functional imaging techniques in assessing tumor angiogenesis and in response to anti-angiogenic based therapy will be a powerful tool. Whereas anatomical/functional imaging with better resolution is aimed at identification of a tumoral mass and the assessment of its size and vascularization, PET imaging of integrin expression is better suited for receptor characterization. A multi-modality approach for tumor angiogenesis imaging is therefore the best strategy. The new generation clinical PET-CT [48] will facilitate this by allowing simultaneous PET and CT studies which may be difficult or even impossible with either imaging modality alone.

Tumor integrin expression imaging is given as an example here to demonstrate how molecular imaging can provide a robust platform for the understanding of mechanisms of tumor angiogenesis and for the evaluation of novel anti-angiogenic and proangiogenic therapies. Questions remain on how to improve the sensitivity and resolution of molecular imaging technologies and to develop optimal molecular imaging probes as surrogate markers to pinpoint and monitor specific molecular and cellular actions of angiogenesis inhibitors. Whether the magnitude of tracer accumulation is a true reflection of integrin  $\alpha_v\beta_3$  expression remains unclear and needs to be developed. The combination and/or fusion of anatomical/functional/molecular imaging techniques will be involved to make this happen.

## ACKNOWLEDGMENTS

The author thanks Dr. Sanjiv Sam Gambhir for very helpful discussions and critical manuscript review. Supported, in part, by National Institute of Biomedical Imaging and Bioengineering (NIBIB) Grant R21 EB001785, Department of Defense (DOD) Breast Cancer Research Program (BCRP) Concept Award DAMD17-03-1-0752, DOD BCRP IDEA Award W81XWH-04-1-0697, DOD Prostate Cancer Research Program (PCRP) New Investigator Award (NIA) DAMD1717-03-1-0143, American Lung Association California (ALAC), the Society of Nuclear Medicine Education and Research Foundation, National Cancer Institute (NCI) Small Animal Imaging Resource Program (SAIRP) grant R24 CA93862, and NCI *In Vivo* Cellular Molecular Imaging Center (ICMIC) grant P50 CA114747.

## REFERENCES

- [1] Bergers, G.; Benjamin, L. E. *Nat. Rev. Cancer.*, **2003**, *3*, 401-10.
- [2] Siemann, D. W.; Chaplin, D. J.; Horsman, M. R. *Cancer*, **2004**, *100*, 2491-9.
- [3] Brower, V., Tumor angiogenesis--new drugs on the block. *Nat. Biotechnol.*, **1999**, *17*, 963-8.
- [4] Jung, Y. D.; Ahmad, S. A.; Liu, W.; Reinmuth, N.; Parikh, A.; Stoeltzing, O.; Fan, F.; Ellis, L. M. *Semin. Cancer Biol.* **2002**, *12*, 105-12.
- [5] Lee, T. Y.; Purdie, T. G.; Stewart, E. Q. *J. Nucl. Med.*, **2003**, *47*, 171-87.
- [6] Miles, K. A. *Br. J. Radiol.*, **2003**, *76*, S36-42.
- [7] Cosgrove, D. *Br. J. Radiol.* **2003**, *76*, S43-9.
- [8] Abu-Hajir, M.; Rand, S. D.; Krouwer, H. G.; Schmainda, K. M. *Semin. Thromb. Hemost.*, **2003**, *29*, 309-15.
- [9] Turetschek, K.; Preda, A.; Novikov, V.; Brasch, R. C.; Weinmann, H. J.; Wunderbalinger, P.; Roberts, T. P. *J. Magn. Reson. Imaging*, **2004**, *20*, 138-44.
- [10] Gambhir, S. S.; Czernin, J.; Schwimmer, J.; Silverman, D. H.; Coleman, R. E.; Phelps, M. E. *J. Nucl. Med.*, **2001**, *42*, 1S-93S.
- [11] Laking, G. R.; Price, P. M. *Br. J. Radiol.* **2003**, *76*, S50-9.
- [12] Gambhir, S. S. *Nat. Rev. Cancer*, **2002**, *2*, 683-93.
- [13] Massoud, T. F.; Gambhir, S. S. *Genes Dev.*, **2003**, *17*, 545-80.
- [14] McDonald, D. M.; Choyke, P. L. *Nat. Med.*, **2003**, *9*, 713-25.
- [15] Schirner, M.; Menrad, A.; Stephens, A.; Frenzel, T.; Hauff, P.; Licha, K. *Ann. N. Y. Acad. Sci.*, **2004**, *1014*, 67-75.
- [16] Hynes, R. O. *Nat. Med.*, **2002**, *8*, 918-21.
- [17] Brooks, P. C.; Clark, R. A.; Cheresh, D. A. *Science*, **1994**, *264*, 569-71.
- [18] Tucker, G. C. *Curr. Opin. Investig. Drugs*, **2003**, *4*, 722-31.
- [19] Ellegala, D. B.; Leong-Poi, H.; Carpenter, J. E.; Klibanov, A. L.; Kaul, S.; Shaffrey, M. E.; Sklenar, J.; Lindner, J. R. *Circulation*, **2003**, *108*, 336-41.
- [20] Sipkins, D. A.; Cheresh, D. A.; Kazemi, M. R.; Nevin, L. M.; Bednarski, M. D.; Li, K. C. *Nat. Med.*, **1998**, *4*, 623-6.
- [21] Chen, X.; Conti, P. S.; Moats, R. A. *Cancer Res.*, **2004**, *64*, 8009-14.
- [22] Wang, W.; Ke, S.; Wu, Q.; Charnsangavej, C.; Gurfinkel, M.; Gelovani, J. G.; Abbruzzese, J. L.; Sevick-Muraca, E. M.; Li, C. *Mol. Imaging*, **2004**, *3*, 343-51.
- [23] Haubner, R.; Wester, H. J. *Curr. Pharm. Des.*, **2004**, *10*, 1439-55.
- [24] Wu, A. M.; Yazaki, P. J.; Tsai, S.; Nguyen, K.; Anderson, A. L.; McCarthy, D. W.; Welch, M. J.; Shively, J. E.; Williams, L. E.; Raubitschek, A. A.; Wong, J. Y.; Toyokuni, T.; Phelps, M. E.; Gambhir, S. S. *Proc. Natl. Acad. Sci. U. S. A.*, **2000**, *97*, 8495-500.
- [25] Xiong, J. P.; Stehle, T.; Zhang, R.; Joachimiak, A.; Frech, M.; Goodman, S. L.; Arnaout, M. A. *Science*, **2002**, *296*, 151-5.
- [26] Gottschalk, K. E.; Kessler, H. *Angew. Chem. Int. Ed. Engl.*, **2002**, *41*, 3767-74.
- [27] Chen, X.; Park, R.; Shahinian, A. H.; Bading, J. R.; Conti, P. S. *Nucl. Med. Biol.*, **2004**, *31*, 11-9.
- [28] Haubner, R.; Wester, H. J.; Reuning, U.; Senekowitsch-Schmidtkne, R.; Diefenbach, B.; Kessler, H.; Stocklin, G.; Schwaiger, M. *J. Nucl. Med.*, **1999**, *40*, 1061-71.
- [29] Haubner, R.; Wester, H. J.; Burkhardt, F.; Senekowitsch-Schmidtkne, R.; Weber, W.; Goodman, S. L.; Kessler, H.; Schwaiger, M. *J. Nucl. Med.*, **2001**, *42*, 326-36.
- [30] Haubner, R.; Wester, H. J.; Weber, W. A.; Mang, C.; Ziegler, S. I.; Goodman, S. L.; Senekowitsch-Schmidtkne, R.; Kessler, H.; Schwaiger, M. *Cancer Res.*, **2001**, *61*, 1781-5.
- [31] Haubner, R.; Kuhnast, B.; Mang, C.; Weber, W. A.; Kessler, H.; Wester, H. J.; Schwaiger, M. *Bioconjug. Chem.*, **2004**, *15*, 61-9.
- [32] Haubner, R.; Weber, W. A.; Beer, A. J.; Vabuliene, E.; Reim, D.; Sarbia, M.; Becker, K. F.; Goebel, M.; Hein, R.; Wester, H. J.; Kessler, H.; Schwaiger, M. *PLoS Med.*, **2005**, *2*, e70.
- [33] Chen, X.; Park, R.; Hou, Y.; Khankaldyyan, V.; Gonzales-Gomez, I.; Tohme, M.; Bading, J. R.; Laug, W. E.; Conti, P. S. *Eur. J. Nucl. Med. Mol. Imaging*, **2004**, *31*, 1081-9.
- [34] Chen, X.; Liu, S.; Hou, Y.; Tohme, M.; Park, R.; Bading, J. R.; Conti, P. S. *Mol. Imaging Biol.*, **2004**, *6*, 350-9.
- [35] Chen, X.; Park, R.; Shahinian, A. H.; Tohme, M.; Khankaldyyan, V.; Bozorgzadeh, M. H.; Bading, J. R.; Moats, R.; Laug, W. E.; Conti, P. S. *Nucl. Med. Biol.*, **2004**, *31*, 179-89.
- [36] Thumshirn, G.; Hersel, U.; Goodman, S. L.; Kessler, H. *Chemistry*, **2003**, *9*, 2717-25.
- [37] Chen, X.; Sievers, E.; Hou, Y.; Park, R.; Tohme, M.; Bart, R.; Bremner, R.; Bading, J. R.; Conti, P. S. *Neoplasia*, **2005**, *7*, 271-9.
- [38] Chen, X.; Tohme, M.; Park, R.; Hou, Y.; Bading, J. R.; Conti, P. S. *Mol. Imaging*, **2004**, *3*, 96-104.
- [39] McCarthy, D. W.; Shefer, R. E.; Klinkowstein, R. E.; Bass, L. A.; Margeneau, W. H.; Cutler, C. S.; Anderson, C. J.; Welch, M. J. *Nucl. Med. Biol.*, **1997**, *24*, 35-43.
- [40] Helisch, A.; Forster, G. J.; Reber, H.; Buchholz, H. G.; Arnold, R.; Goke, B.; Weber, M. M.; Wiedenmann, B.; Pauwels, S.; Haus, U.; Bouterfa, H.; Bartenstein, P. *Eur. J. Nucl. Med. Mol. Imaging*, **2004**, *31*, 1386-92.
- [41] Verel, I.; Visser, G. W.; Vosjan, M. J.; Finn, R.; Boellaard, R.; van Dongen, G. A. *Eur. J. Nucl. Med. Mol. Imaging*, **2004**, *31*, 1645-52.
- [42] Kwekkeboom, D.; Krenning, E. P.; de Jong, M. J. *Nucl. Med.*, **2000**, *41*, 1704-13.
- [43] Chen, X.; Park, R.; Tohme, M.; Shahinian, A. H.; Bading, J. R.; Conti, P. S. *Bioconjug. Chem.*, **2004**, *15*, 41-9.
- [44] Chen, X.; Hou, Y.; Tohme, M.; Park, R.; Khankaldyyan, V.; Gonzales-Gomez, I.; Bading, J. R.; Laug, W. E.; Conti, P. S. *J. Nucl. Med.*, **2004**, *45*, 1776-83.
- [45] Wu, Y.; Fisher, D. R.; Liu, S.; Chen, X. *J. Nucl. Med.*, **2005**, *46*, 27P.
- [46] Schmidt, K. C.; Turkheimer, F. E. *Q. J. Nucl. Med.*, **2002**, *46*, 70-85.
- [47] Logan, J. *Nucl. Med. Biol.*, **2000**, *27*, 661-70.
- [48] Kapoor, V.; McCook, B. M.; Torok, F. S. *Radiographics*, **2004**, *24*, 523-43.
- [49] Kageshita, T.; Hamby, C. V.; Hirai, S.; Kimura, T.; Ono, T.; Ferrone, S. *Int. J. Cancer*, **2000**, *89*, 153-9.

# A Thiol-Reactive $^{18}\text{F}$ -Labeling Agent, *N*-[2-(4- $^{18}\text{F}$ -Fluorobenzamido)Ethyl]Maleimide, and Synthesis of RGD Peptide-Based Tracer for PET Imaging of $\alpha_v\beta_3$ Integrin Expression

Weibo Cai\*, Xianzhong Zhang\*, Yun Wu, and Xiaoyuan Chen

Molecular Imaging Program at Stanford (MIPS) and Bio-X Program, Department of Radiology, Stanford University School of Medicine, Stanford, California

The cell adhesion molecule integrin  $\alpha_v\beta_3$  plays a key role in tumor angiogenesis and metastasis. A series of  $^{18}\text{F}$ -labeled RGD peptides have been developed for PET of integrin expression based on primary amine-reactive prosthetic groups. In this study we introduced a new method of labeling RGD peptides through a thiol-reactive synthon, *N*-[2-(4- $^{18}\text{F}$ -fluorobenzamido)ethyl]maleimide ( $^{18}\text{F}$ -FBEM). **Methods:**  $^{18}\text{F}$ -FBEM was synthesized by coupling *N*-succinimidyl 4- $^{18}\text{F}$ -fluorobenzoate ( $^{18}\text{F}$ -SFB) with *N*-(2-aminoethyl)maleimide. After high-pressure liquid chromatography purification, it was allowed to react with thiolated RGD peptides, and the resulting tracers were subjected to receptor-binding assay, *in vivo* metabolic stability assessment, biodistribution, and microPET studies in murine xenograft models. **Results:** Conjugation of monomeric and dimeric sulphydryl-RGD peptides with  $^{18}\text{F}$ -FBEM was achieved in high yields ( $85\% \pm 5\%$  nondecay-corrected on the basis of  $^{18}\text{F}$ -FBEM). The radiochemical purity of the  $^{18}\text{F}$ -labeled peptides was  $>98\%$  and the specific activity was  $100\sim150$  TBq/mmol. Noninvasive microPET and direct tissue sampling experiments demonstrated that both  $^{18}\text{F}$ -FBEM-SRGD (RGD monomer) and  $^{18}\text{F}$ -FBEM-SRGD2 (RGD dimer) had integrin-specific tumor uptake in subcutaneous U87MG glioma and orthotopic MDA-MB-435 breast cancer xenografts. **Conclusion:** The new tracer  $^{18}\text{F}$ -FBEM-SRGD2 was synthesized with high specific activity via  $^{18}\text{F}$ -FBEM and the tracer exhibited high receptor-binding affinity, tumor-targeting efficacy, metabolic stability, as well as favorable *in vivo* pharmacokinetics. The new synthon  $^{18}\text{F}$ -FBEM developed in this study will also be useful for radiolabeling of other thiolated biomolecules.

**Key Words:** thiol-reactive synthon;  $^{18}\text{F}$ -FBEM; microPET;  $^{18}\text{F}$  labeling; integrin  $\alpha_v\beta_3$

J Nucl Med 2006; 47:1172–1180

**T**he  $\alpha_v\beta_3$  integrin, which binds to arginine-glycine-aspartic acid (RGD)-containing components of the interstitial matrix, such as vitronectin, fibronectin, and thrombospondin, is significantly upregulated on endothelium during angiogenesis but not in quiescent endothelium (1,2). The special role of integrin  $\alpha_v\beta_3$  in tumor invasion and metastasis arises from its ability to recruit and activate matrix metalloproteinase MMP-2 and plasmin, which degrade components of the basement membrane and interstitial matrix (3). Integrins expressed on endothelial cells modulate cell migration and survival during angiogenesis, whereas integrins expressed on carcinoma cells potentiate metastasis by facilitating invasion and movement across blood vessels (2,4). Antagonists of integrin  $\alpha_v\beta_3$  (antibodies, peptides, and peptidomimetics) can inhibit tumor angiogenesis, tumor growth, and metastasis *in vivo* (5). The ability to noninvasively visualize and quantify tumor integrin  $\alpha_v\beta_3$  expression level will provide new opportunities to document tumor (tumor cells and sprouting tumor vasculature) integrin expression, to more appropriately select patients for antiintegron treatment, and to monitor treatment efficacy in integrin-positive patients.

Over the last several years, significant advances have been achieved in developing novel probes for multimodality molecular imaging of tumor integrin expression (6). Small molecules, peptides, peptidomimetic integrin  $\alpha_v\beta_3$  antagonists, and antibodies have been labeled with radioisotopes, superparamagnetic nanoparticles, fluorescent dyes, quantum dots, and microbubbles for PET, SPECT, MRI, near-infrared fluorescence, and ultrasound imaging of small animals, mostly tumor models (6,7). Because of the high sensitivity and adequate spatial and temporal resolution of PET, development of PET probes for integrin expression imaging is currently the most active among all of these modalities.

Cyclic RGD peptide was first labeled with  $^{18}\text{F}$  by Haubner et al. and the resulting  $^{18}\text{F}$ -galacto-RGD exhibited integrin  $\alpha_v\beta_3$ –specific tumor uptake in an integrin-positive

Received Nov. 30, 2005; revision accepted Mar. 6, 2006.

For correspondence or reprints contact: Xiaoyuan Chen, PhD, Molecular Imaging Program at Stanford (MIPS) and Bio-X Program, Department of Radiology, Stanford University School of Medicine, 1201 Welch Rd., Room P095, Stanford, CA 94305-5484.

E-mail: shawchen@stanford.edu

\*Contributed equally to this work.

COPYRIGHT © 2006 by the Society of Nuclear Medicine, Inc.

M21 melanoma xenograft model (8,9). Initial clinical trials in healthy volunteers and a limited number of cancer patients revealed that this tracer can be administered safely to patients and is capable of delineating certain lesions that are integrin positive with some indication of integrin  $\alpha_v\beta_3$  expression level in vivo (9,10). We labeled a series of mono-, di-, and tetrameric RGD peptides with  $^{18}\text{F}$  or  $^{64}\text{Cu}$  for integrin-positive tumor targeting (11–19). In particular, the dimeric RGD peptide-based tracer  $^{18}\text{F}$ -FRGD2 was found to be able to visualize and quantify the integrin expression level in vivo (11,12).

Radiofluorination of RGD peptides generally uses  $^{18}\text{F}$ -synthons such as *N*-succinimidyl 4- $^{18}\text{F}$ -fluorobenzoate ( $^{18}\text{F}$ -SFB) (20,21) or *p*-nitrophenyl  $^{18}\text{F}$ -fluoropropionate ( $^{18}\text{F}$ -NFP) (22) to form a stable amide bond by reacting with primary amino groups of RGD peptides. It was also reported that oxoamino derivatives of RGD peptides react with 4- $^{18}\text{F}$ -fluorobenzaldehyde ( $^{18}\text{F}$ -FBA) under acidic condition to form an oxime (23). A few  $^{18}\text{F}$  labeled thiol-reactive reagents have been reported in the literature—namely, 1-(4- $^{18}\text{F}$ -fluorophenyl)pyrrole-2,5-dione ( $^{18}\text{F}$ -FPPD) (24), *N*-[3-(2,5-dioxo-2,5-dihydropyrrol-1-yl)phenyl]-4- $^{18}\text{F}$ -fluorobenzamide ( $^{18}\text{F}$ -DDPFB) (24), 1-[3-(2-( $^{18}\text{F}$ -fluoropyridin-3-yloxy)propyl]pyrrole-2,5-dione ( $^{18}\text{F}$ -FPyME) (25), and *N*-[4-[(4- $^{18}\text{F}$ -fluorobenzylidene)aminoxy]butyl]maleimide ( $^{18}\text{F}$ -FBABM) (26). However, no *in vivo* microPET data have been reported on tracers synthesized using these prosthetic groups. In this study, we developed a new thiol-reactive synthon, *N*-[2-(4- $^{18}\text{F}$ -fluorobenzamido)ethyl]maleimide ( $^{18}\text{F}$ -FBEM), for  $^{18}\text{F}$  labeling of thiol-containing molecules. Two thiolated RGD peptides were labeled with  $^{18}\text{F}$  through  $^{18}\text{F}$ -FBEM and tested in murine xenograft models.

## MATERIALS AND METHODS

Unless otherwise specified, all chemicals were of analytic grade and commercially available. RGD peptides were synthesized as previously reported (11,12). *N*-Succinimidyl *S*-acetylthioacetate (SATA), hydroxylamine-HCl, and tris(2-carboxyethyl)phosphine hydrochloride (TCEP-HCl) were purchased from Pierce Biotechnology, Inc. *N*-(2-Aminoethyl)maleimide trifluoroacetate salt, 4-fluorobenzoic acid, *N,N,N',N'*-tetramethyl-*O*-(*N*-succinimidyl) uronium tetrafluoroborate (TSTU), *N*-hydroxysuccinimide (NHS), and *N,N*-diisopropylethylamine (DIPEA) were purchased from Sigma-Aldrich. No-carrier-added  $^{18}\text{F}$ - $\text{F}^-$  was obtained from the in-house PETtrace cyclotron (GE Healthcare). The  $^{18}\text{F}$ - $\text{F}^-$  was provided in a mixture solution of  $\text{K}_2\text{CO}_3$  (2 mg/mL in water) and Kryptofix 2.2.2. (Sigma-Aldrich; 10 mg/mL in acetonitrile). The semipreparative reversed-phase high-pressure liquid chromatography (RP-HPLC) system was reported earlier (12). Reversed-phase extraction C<sub>18</sub> Sep-Pak cartridges (Waters) were pretreated with methanol and water before use.

The SATA-RGD peptides were prepared following the protocol supplied by the vendor. Briefly, c(RGDyK) or E[c(RGDyK)]<sub>2</sub> (5  $\mu\text{mol}$ ) in 1 mL 50 mmol/L Na<sub>2</sub>B<sub>4</sub>O<sub>7</sub> buffer (pH 8.5) was mixed with 100  $\mu\text{L}$  SATA solution in dimethyl sulfoxide (DMSO; 6  $\mu\text{mol}$ ). After the reaction had gone to completion as shown by analytic RP-HPLC, it was quenched by 100  $\mu\text{L}$  2% trifluoroacetic

acid (TFA) in water. The crude product was lyophilized without purification. The yield of SATA-c(RGDyK) (HPLC retention time [R<sub>t</sub>], 12.1 min) was 95% and that of SATA-E[c(RGDyK)]<sub>2</sub> (R<sub>t</sub>, 13.6 min) was 65% on the basis of analytic RP-HPLC.

The crude SATA-RGD peptides (20 mg) were dissolved in 1 mL water and 100  $\mu\text{L}$  of 0.5 mol/L hydroxylamine solution were added. The pH was adjusted to 6.0. After 2 h, sulfhydryl-c(RGDyK) and sulfhydryl-E[c(RGDyK)]<sub>2</sub> (denoted as SRGD and SRGD2, respectively) were purified by semipreparative RP-HPLC. The overall yield was 80% and 50% for SRGD (R<sub>t</sub>, 10.7 min) and SRGD2 (R<sub>t</sub>, 13.1 min), respectively; little or no dimerization was observed for either peptide when stored under acidic condition (pH 3). MALDI-TOF MS (matrix-assisted laser desorption/ionization time-of-flight mass spectroscopy): SRGD, C<sub>29</sub>H<sub>43</sub>N<sub>9</sub>O<sub>9</sub>S, calculated 693.3, observed 694.5 ([M+H]<sup>+</sup>); SRGD2, C<sub>61</sub>H<sub>89</sub>N<sub>19</sub>O<sub>19</sub>S, calculated 1,423.6, observed 1,422.7 ([M+H]<sup>+</sup>).

*N*-(2-Aminoethyl)maleimide (5  $\mu\text{mol}$ ) in 200  $\mu\text{L}$  acetonitrile, *N*-succinimidyl 4-fluorobenzoate (4.5  $\mu\text{mol}$ ) in 100  $\mu\text{L}$  acetonitrile, and 500  $\mu\text{L}$  50 mmol/L Na<sub>2</sub>B<sub>4</sub>O<sub>7</sub> buffer (pH 8.5) were mixed and reacted at 50°C for 20 min. The reaction was quenched by adding 100  $\mu\text{L}$  2% TFA in water. HPLC purification gave FBEM in 85% yield. <sup>1</sup>H NMR (chloroform-*d*, 400 MHz): 7.79–7.76 (m, 2H, phenyl *o*-H); 7.26–7.09 (m, 2H, phenyl *m*-H); 6.75 (2H, CH=CH); 3.86–3.65 (m, 4H, CH<sub>2</sub>–CH<sub>2</sub>).

The sulfhydryl-RGD peptides (0.5  $\mu\text{mol}$ ) were dissolved in 0.5 mL phosphate-buffered saline (PBS, pH 7.4; Invitrogen Corp.). FBEM (0.55  $\mu\text{mol}$ ) was dissolved in 200  $\mu\text{L}$  acetonitrile and added to the solution. After 30 min, the reaction mixture was subjected to HPLC purification. FBEM-SRGD (R<sub>t</sub>, 14.8 min) and FBEM-SRGD2 (R<sub>t</sub>, 15.2 min) were obtained with 80% yield. MALDI-TOF MS: FBEM-SRGD, C<sub>42</sub>H<sub>54</sub>FN<sub>11</sub>O<sub>12</sub>S, calculated 956.1, observed 956.7 ([M+H]<sup>+</sup>); FBEM-SRGD2, C<sub>73</sub>H<sub>98</sub>FN<sub>21</sub>O<sub>22</sub>S, calculated 1,672.5, observed 1,673.5 ([M+H]<sup>+</sup>).

## Radiochemistry

$^{18}\text{F}$ -SFB was synthesized as previously reported (12,15) with C<sub>18</sub> Sep-Pak cartridge purification. It was dissolved in acetonitrile (300  $\mu\text{L}$ ) and 1 mg *N*-(2-aminoethyl)maleimide in 500  $\mu\text{L}$  acetonitrile and 20  $\mu\text{L}$  DIPEA were added. The reaction mixture was heated to 40°C for 20 min and then quenched by addition of 50  $\mu\text{L}$  TFA. HPLC purification gave  $^{18}\text{F}$ -FBEM (R<sub>t</sub>, 13.9 min; total reaction time, 150 ± 20 min with nondecay-corrected radiochemical yield of 5% ± 2% on the basis of  $^{18}\text{F}$ - $\text{F}^-$ ; specific activity, 150~200 TBq/mmol).

$^{18}\text{F}$ -FBEM was dissolved in 600  $\mu\text{L}$  PBS buffer (pH 7.4); 0.2 mg of sulfhydryl-RGD peptide in 50  $\mu\text{L}$  DMSO and 1.0 mg TCEP-HCl in 0.1 mL water were then added. The pH was adjusted to 7.0~7.5 using 0.2 mol/L NaOH solution. The reaction mixture was kept at room temperature (r.t.) for 20 min. HPLC purification gave  $^{18}\text{F}$ -FBEM-SRGD (R<sub>t</sub>, 14.9 min) and  $^{18}\text{F}$ -FBEM-SRGD2 (R<sub>t</sub>, 15.3 min) in 80% nondecay-corrected yield in both cases. The radiotracers were reconstituted in PBS and passed through a 0.22- $\mu\text{m}$  Millipore filter into a sterile vial for *in vivo* applications. Nonreacted sulfhydryl-RGD peptides were baseline-separated from the desired products during HPLC and the specific activity of the tracers was 100–150 TBq/mmol.

Eppendorf microcentrifuge tubes containing 500  $\mu\text{L}$  of octanol, 500  $\mu\text{L}$  of normal saline, and ~370 kBq of  $^{18}\text{F}$ -FBEM-SRGD or  $^{18}\text{F}$ -FBEM-SRGD2 were vortexed vigorously for 1 min. Each tube was centrifuged at 14,000 rpm for 5 min and the activities in 20- $\mu\text{L}$  aliquots of both organic and aqueous layers were measured

by a  $\gamma$ -counter (GMI, Inc.). The reported octanol/water partition coefficient represents the mean  $\pm$  SD of 6 measurements.

### In Vitro Cell-Binding Assay

Both U87MG and MDA-MB-435 cell lines were purchased from American Type Culture Collection and the culture media were obtained from Invitrogen Co. U87MG glioblastoma cells were grown in Dulbecco's modified Eagle medium (DMEM, low glucose) and MDA-MB-435 breast cancer carcinoma cells were grown in Leibovitz's L-15 medium. Both cell lines were cultured in the medium supplemented with 10% (v/v) fetal bovine serum (FBS) at 37°C. In vitro integrin-binding affinities and specificities were assessed via displacement cell-binding assays using  $^{125}$ I-echistatin as the integrin  $\alpha_v\beta_3$ -specific radioligand. Both U87MG and MDA-MB-435 cells are integrin  $\alpha_v\beta_3$  positive (12). Cell-binding assay were performed using U87MG cells. The cells were harvested, washed twice with PBS, and resuspended ( $2 \times 10^6$  cells/mL) in binding buffer (20 mmol/L Tris, pH 7.4, 150 mmol/L NaCl, 2 mmol/L CaCl<sub>2</sub>, 1 mmol/L MgCl<sub>2</sub>, 1 mmol/L MnCl<sub>2</sub>, 0.1% bovine serum albumin). Millipore 96-well filter multiscreen DV plates (pore size, 0.65  $\mu$ m) were seeded with  $10^5$  cells per well and incubated with  $^{125}$ I-echistatin (30,000 cpm/well) in the presence of increasing concentrations of different RGD peptide analogs (0–1,000 nmol/L). The total volume in each well was adjusted to 200  $\mu$ L. After incubation at r.t. for 2 h, the plates were filtered through a multiscreen vacuum manifold and washed twice with cold binding buffer. The filters were collected and the radioactivity was measured using a  $\gamma$ -counter. The best-fit IC<sub>50</sub> (inhibitory concentration of 50%) values for U87MG cells were calculated by fitting the data by nonlinear regression using GraphPad Prism (GraphPad Software, Inc.). Experiments were performed twice with triplicate samples.

### Animal Models

All animal experiments were performed under a protocol approved by the Stanford University Administrative Panel on Laboratory Animal Care. The MDA-MB-435 breast cancer model was established by orthotopic injection of  $5 \times 10^6$  cells into the left mammary fat pad of female athymic nude mice, whereas the U87MG tumor model was obtained by injecting a mixture of  $5 \times 10^6$  cells suspended in 50  $\mu$ L medium and 50  $\mu$ L Matrigel (BD Biosciences) into the right front leg. The mice were used for biodistribution and microPET imaging studies when the tumor volume reached 300–400 mm<sup>3</sup> (3–4 wk after inoculation for both U87MG and MDA-MB-435 tumors).

### Biodistribution Studies

Female athymic nude mice bearing both U87MG and MDA-MB-435 tumors were injected with 1 MBq of  $^{18}$ F-FBEM-SRGD or  $^{18}$ F-FBEM-SRGD2. The mice were sacrificed and dissected at 10, 30, and 60 min after injection. Blocking experiment was performed by coinjecting radiotracer with a saturating dose of c(RGDyK) (10 mg/kg mouse body weight) and the mice were sacrificed at 60 min after injection. Blood, tumor, major organs, and tissues were collected and wet weighed (contents in the intestines were removed before weighing). The radioactivity in the tissues was measured using a  $\gamma$ -counter. The results were calculated as percentage injected dose per gram (%ID/g). For each mouse, the radioactivity of the tissue samples was calibrated against a known aliquot of the injectate and normalized to a body weight of 20 g. Values are expressed as mean  $\pm$  SD for 3 animals per group.

### microPET and Image Analysis

PET scans were performed using a microPET R4 rodent model scanner (Concorde Microsystems Inc.). The scanner has a computer-controlled bed and 10.8-cm transaxial and 8-cm axial fields of view (FOVs). It has no septa and operates exclusively in the 3-dimensional list mode. Animals were placed near the center of FOV of the microPET scanner, where the highest image resolution and sensitivity are available. Mice were injected with 3.7 MBq of  $^{18}$ F-FBEM-SRGD or  $^{18}$ F-FBEM-SRGD2 via tail vein under isoflurane anesthesia. The 60-min dynamic ( $5 \times 60$  s,  $5 \times 120$  s,  $5 \times 180$  s,  $6 \times 300$  s) microPET data acquisition (total of 21 frames) was started about 3 min after radiotracer injection. Later time-point static images were also acquired as 10-min static images after obtaining a 1-h dynamic scan. The images were reconstructed by a 2-dimensional ordered-subsets expectation maximum algorithm and no correction was applied for attenuation or scatter (27).

For each microPET scan, regions of interests (ROIs) were drawn over each tumor, normal tissue, and major organs by using vendor software ASI Pro 5.2.4.0 on decay-corrected whole-body coronal images. The maximum radioactivity concentration (accumulation) within a tumor or an organ was obtained from mean pixel values within the multiple ROI volume, which were converted to MBq/mL/min by using a conversion factor. Assuming a tissue density of 1 g/mL, the ROIs were converted to MBq/g/min, and then divided by the administered activity to obtain an imaging ROI-derived %ID/g.

### Metabolic Stability

Athymic nude mice bearing U87MG tumor were intravenously injected 3.7 MBq of  $^{18}$ F-FBEM-SRGD2. The animals were sacrificed 60 min after tracer injection. Blood, urine, liver, kidneys, and tumor were collected. Blood was immediately centrifuged for 5 min at 13,200 rpm. Organs were homogenized using an IKA Ultra-Turrax T8 homogenizer (IKA Works Inc.), suspended in 1 mL of PBS buffer, and centrifuged for 5 min at 13,200 rpm. After removal of the supernatant, the pellets were washed with 500  $\mu$ L of PBS. For each sample, supernatants of both centrifugation steps were combined and passed through Sep-Pak C<sub>18</sub> cartridges. The urine sample was directly diluted with 1 mL of PBS and then passed through the cartridge. The cartridges were washed with 2 mL of water and eluted with 2 mL of acetonitrile containing 0.1% TFA. After removal of acetonitrile, the residue was redissolved in 1 mL of water and injected onto an analytic HPLC column. Radioactivity was monitored using a solid-state radiation detector. The eluent was also collected using a fraction collector (0.5 min/fraction) and the activity of each fraction was measured by a  $\gamma$ -counter.

### Statistical Analysis

Quantitative data are expressed as mean  $\pm$  SD. Means were compared using 1-way ANOVA and a Student *t* test. *P* values  $< 0.05$  were considered significant.

## RESULTS

### Chemistry

Both monomeric peptide SRGD and the dimeric peptide SRGD2 were synthesized with good overall yield (80% for SRGD and 50% for SRGD2, respectively). FBEM was prepared by reacting SFB with *N*-(2-aminoethyl)maleimide (90% yield). The conjugation of SRGD or SRGD2 with

FBEM was performed at r.t. The resulting conjugates FBEM-SRGD and FBEM-SRGD2 were purified by RP-HPLC and confirmed by MALDI-TOF mass spectrometry.

<sup>18</sup>F-SFB was synthesized following a previously reported procedure (12,15). <sup>18</sup>F-FBEM was obtained by coupling <sup>18</sup>F-SFB with *N*-(2-aminoethyl)maleimide (Fig. 1A). After HPLC purification, the thiol-reactive synthon was allowed to react with SRGD or SRGD2 at r.t. for 20 min. Starting from <sup>18</sup>F-F<sup>-</sup>, the total reaction time including final HPLC purification was about 200 ± 25 min. The overall decay-corrected radiochemical yield was 20% ± 4% (*n* = 5) for both <sup>18</sup>F-FBEM-SRGD (Fig. 1B) and <sup>18</sup>F-FBEM-SRGD2 (Fig. 1C). On the basis of <sup>18</sup>F-FBEM, both reactions were

achieved in high yields ( $85\% \pm 5\%$  nondecay corrected), virtually quantitative. The radiochemical purity of the  $^{18}\text{F}$ -labeled peptides was  $>98\%$  according to analytic HPLC. The octanol/water partition coefficient ( $\log P$ ) for  $^{18}\text{F}$ -FBEM-SRGD was determined to be  $0.93 \pm 0.02$ , indicating the hydrophobic character of this tracer, whereas  $^{18}\text{F}$ -FBEM-SRGD2 was hydrophilic ( $\log P = -1.69 \pm 0.02$ ).

## In Vitro Cell-Binding Assay

The cell-binding affinity studies of c(RGDyK), E[c(RGDyK)]<sub>2</sub>, FBEM-SRGD, and FBEM-SRGD2 with U87MG cells are summarized in Figure 2. All 4 peptides inhibited the binding of <sup>125</sup>I-echistatin to U87MG cells in a

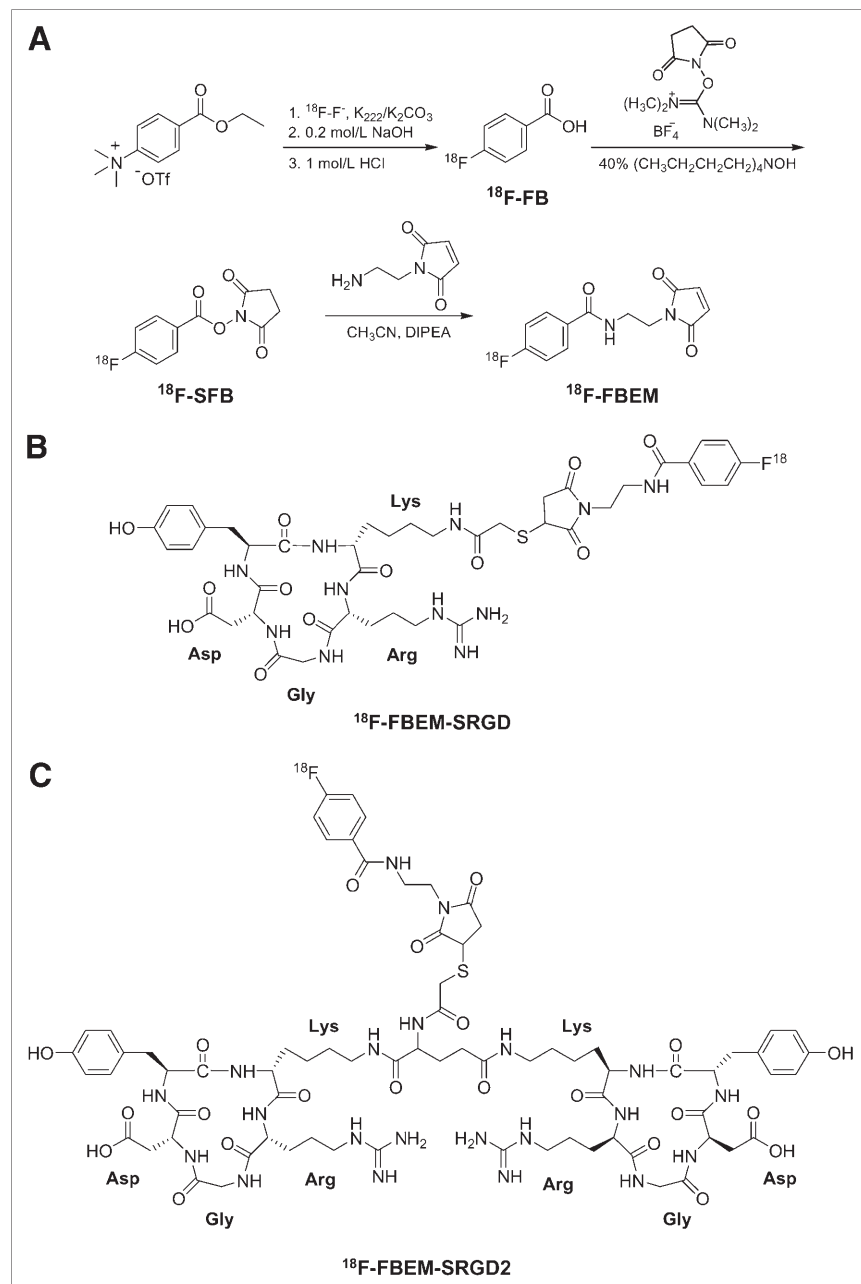


**FIGURE 1.** (A) Synthetic route for *N*-[2-(4-<sup>18</sup>F-fluorobenzamido)ethyl]maleimide (<sup>18</sup>F-FBEM). (B) Structure of <sup>18</sup>F-FBEM-SRGD. (C) Structure of <sup>18</sup>F-FBEM-SRGD2

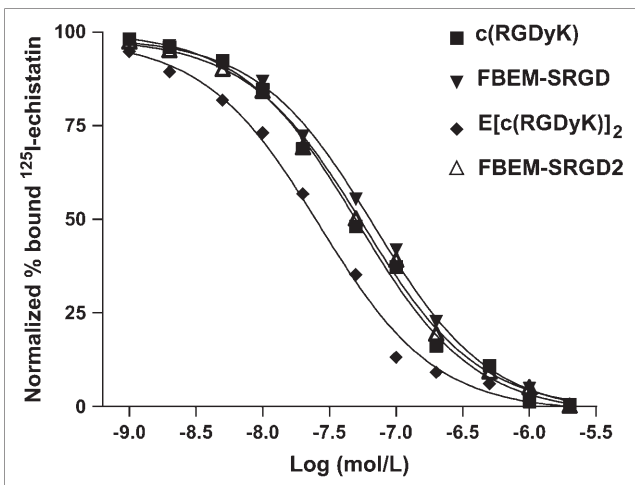


**FIGURE 2.** Cell-binding assay of c(RGDyK), E[c(RGDyK)]<sub>2</sub>, FBEM-SRGD, and FBEM-SRGD2 using U87MG cells (integrin  $\alpha_v\beta_3$ -positive human glioblastoma). The cell-binding affinity of the peptides was determined by performing competitive displacement studies with <sup>125</sup>I-echistatin. IC<sub>50</sub> values for c(RGDyK), E[c(RGDyK)]<sub>2</sub>, FBEM-SRGD, and FBEM-SRGD2 were 51.3  $\pm$  4.2, 26.1  $\pm$  3.2, 66.8  $\pm$  5.1, and 55.1  $\pm$  6.5 nmol/L, respectively ( $n = 6$ ).

dose-dependent manner. The IC<sub>50</sub> values for c(RGDyK), E[c(RGDyK)]<sub>2</sub>, FBEM-SRGD, and FBEM-SRGD2 were 51.3  $\pm$  4.2, 26.1  $\pm$  3.2, 66.8  $\pm$  5.1, and 55.1  $\pm$  6.5 nmol/L, respectively, indicating that FBEM conjugation had minimal effect on the integrin-binding avidity of the RGD peptides.

#### Biodistribution

Biodistribution of <sup>18</sup>F-FBEM-SRGD and <sup>18</sup>F-FBEM-SRGD2 was determined in athymic nude mice bearing both U87MG and MDA-MB-435 tumors and the results are shown in Figure 3. For <sup>18</sup>F-FBEM-SRGD (Fig. 3A), the U87MG and MDA-MB-435 tumor uptakes were 1.33  $\pm$  0.28 and 1.43  $\pm$  0.11 %ID/g, respectively, at 60 min after injection. When blocked by coinjection of c(RGDyK) at a dose of 10 mg/kg body weight, the tumor uptake decreased to 0.40  $\pm$  0.02 %ID/g for the U87MG tumor ( $P < 0.05$  when compared with the U87MG tumor without blocking) and 0.77  $\pm$  0.04 %ID/g for the MDA-MB-435 tumor ( $P < 0.05$  when compared with the MDA-MB-435 tumor without blocking), respectively. Intestine exhibited a high uptake of <sup>18</sup>F-FBEM-SRGD (16.57  $\pm$  0.81 %ID/g when c(RGDyK) was coinjected), most probably due to the relatively hydrophobic nature of the tracer, which is consistent with our previous result for <sup>18</sup>F-FB-RGD (18). For <sup>18</sup>F-FBEM-SRGD2 (Fig. 3B), the U87MG and MDA-MB-435 tumor uptakes were 2.71  $\pm$  0.19 and 5.25  $\pm$  0.17 %ID/g, respectively, at 60 min after injection ( $P < 0.01$  for U87MG and  $P < 0.001$  for MDA-MB-435 when compared with <sup>18</sup>F-FBEM-SRGD). When blocked by coinjection of c(RGDyK) at 10 mg/kg body weight, the tumor uptake of U87MG tumor decreased  $>5$ -fold to 0.52  $\pm$  0.26 %ID/g ( $P < 0.01$ ). Blocking reduced

the tumor uptake of both tracers to the background level (due to nonspecific binding in normal organs), clearly indicating integrin-specific binding. Kidney uptake of <sup>18</sup>F-FBEM-SRGD was high at an early time point (11.40  $\pm$  0.22 %ID/g at 10 min after injection), but the washout was also fast. The 2 tracers exhibited different excretion routes due to the difference in hydrophilicity. <sup>18</sup>F-FBEM-SRGD is relatively hydrophobic, therefore exhibiting mainly hepatobiliary excretion, whereas <sup>18</sup>F-FBEM-SRGD2 is more hydrophilic and mainly excreted through the kidney. It is worth noting that more radioactivity accumulated in the MDA-MB-435 tumor with time for <sup>18</sup>F-FBEM-SRGD2 (Fig. 3B), which might be due to the internalization of the tracer. A similar phenomenon was observed in our previous studies for the <sup>18</sup>F-FRGD2 tracer (12). Comparing these 2 radiotracers, <sup>18</sup>F-FBEM-SRGD2 has significantly higher kidney and tumor uptake, whereas <sup>18</sup>F-FBEM-SRGD has much higher intestine uptake. There was no major difference in the tracer uptake by other organs between the 2 tracers.

#### microPET

Dynamic microPET scans were performed for both radiotracers. Selected coronal images at different time points after injection in a mouse bearing both subcutaneous U87MG and orthotopic MDA-MB-435 tumors are shown in Figure 4. High tumor activity accumulation was observed as early as 6 min after injection for both tracers. For <sup>18</sup>F-FBEM-SRGD, the U87MG and MDA-MB-435 tumor uptakes were 1.27 and 1.04 %ID/g at 60 min after injection, respectively, whereas the liver and kidney uptake were much higher than that of the tumors. Up to 4 h after injection, there is still a fair amount of activity accumulated in the abdomen. <sup>18</sup>F-FBEM-SRGD was excreted through both liver and kidneys (Fig. 5A). For <sup>18</sup>F-FBEM-SRGD2, most radioactivity in nontargeted tissues was cleared at 60 min after injection. The uptakes in the U87MG, MDA-MB-435, kidneys, liver, and lung at 60 min after injection were 2.14, 2.11, 4.00, 1.46, and 0.58 %ID/g, respectively. Time-activity curves showed that this tracer excreted predominantly through the renal route (Fig. 5B). When the microPET images of these 2 radiotracers were compared, <sup>18</sup>F-FBEM-SRGD2 had a much better tumor-to-background contrast and higher tumor uptake, which makes it more suitable for future clinical studies.

Static microPET scans with blocking were then performed for <sup>18</sup>F-FBEM-SRGD2 on U87MG tumor-bearing mice (Fig. 6). When coinjected with 10 mg/kg of c(RGDyK), the tracer uptake in the U87MG tumor dropped from 2.21 %ID/g to 0.94 %ID/g at 30 min after injection and from 1.73 %ID/g to 0.44 %ID/g at 60 min after injection, which are essentially at the background level. Successful blocking again confirmed the integrin  $\alpha_v\beta_3$ -specific binding of the radiotracer <sup>18</sup>F-FBEM-SRGD2.

#### Metabolism of <sup>18</sup>F-FBEM-SRGD2

The metabolic stability of <sup>18</sup>F-FBEM-SRGD2 was also determined in mouse blood and urine samples and in liver,

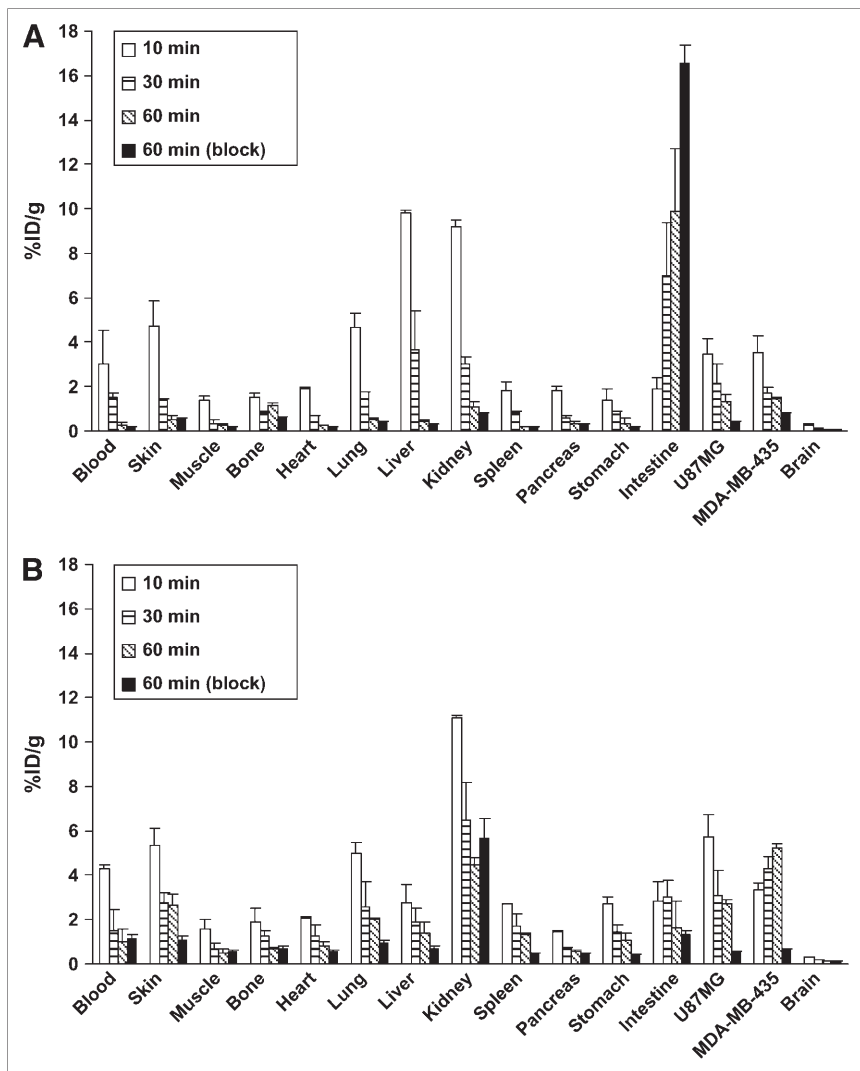


**FIGURE 3.** Biodistribution of <sup>18</sup>F-FBEM-SRGD (A) and <sup>18</sup>F-FBEM-SRGD2 (B) in athymic nude mice bearing both U87MG and MDA-MB-435 tumors at 10, 30, and 60 min after injection ( $n = 3$ ). Biodistribution of both tracers at 60 min after injection when coinjected with 10 mg/kg mice body weight of c(RGDyK) is also shown.

kidneys, and U87MG tumor homogenates at 60 min after tracer injection. The extraction efficiency for all organs was  $>90\%$  (Table 1). The lowest elution efficiency was found for the U87MG tumor and the liver. HPLC analysis results of the soluble fractions of all samples are shown in Figure 7. The percentage of intact tracer was between 41.7% (urine) and 85.8% (kidney). Although we did not identify the composition of the metabolites, we found that all metabolites came out earlier from the HPLC column than the parent compound. The major metabolite peak was found at about 13 min for almost all organs except the kidney. No defluoridation of <sup>18</sup>F-FBEM-SRGD2 was observed, as there is no bone uptake visible in all of the microPET scans.

## DISCUSSION

<sup>18</sup>F labeling is generally achieved through 3 types of functional groups: amino group, carboxylic acid group, and sulfhydryl group. Most known <sup>18</sup>F-labeling reagents for peptides and protein react with the primary amino groups at the N terminus or the lysine side chain. This can be

achieved through active esters, aldehydes, imides, or azido functionalities. <sup>18</sup>F-SFB is probably the most-often-used active ester for <sup>18</sup>F labeling via an acylation reaction (12,15,21). Reductive amination using 4-<sup>18</sup>F-fluorobenzaldehyde (<sup>18</sup>F-FBA) (28), oxime formation using <sup>18</sup>F-FBA (23,29), imidation reaction using 3-<sup>18</sup>F-fluoro-5-nitrobenzimidate (<sup>18</sup>F-FNB) (30), photochemical conjugation using 4-azidophenacyl <sup>18</sup>F-fluoride (<sup>18</sup>F-APF) (22), and alkylation reactions using 4-<sup>18</sup>F-fluorophenacyl bromide (<sup>18</sup>F-FPB) have been reported earlier (30). The major concern for protein labeling using these reagents is the possible interference with biologic activity: modification of one or more lysines located at or near the active site could reduce the binding affinity through steric hindrance if a bulky group is added. <sup>18</sup>F labeling of peptide or protein via the carboxylic acid group at the C terminus or internal glutamic/aspartic acid side chain is less common. Only 2 amines, 1-[4-(<sup>18</sup>F-fluoromethyl)benzoyl]aminobutane-4-amine (<sup>18</sup>F-FMBAA) (31) and 4-<sup>18</sup>F-fluorophenylhydrazine (<sup>18</sup>F-FPH) (32), have been reported for these amidation reactions.

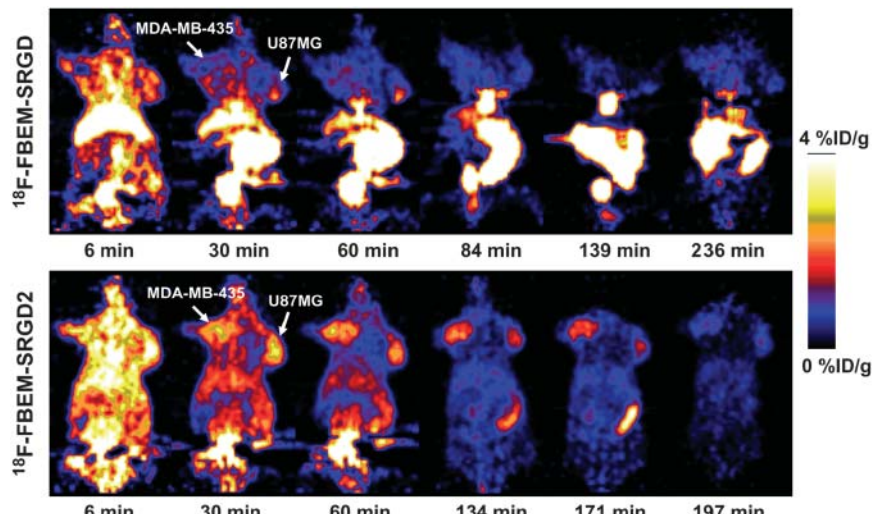


**FIGURE 4.** Dynamic microPET scans using both radiotracers at different time points in a mouse bearing both U87MG and MDA-MB-435 tumors. Ten-minute static scans at several later time points were also conducted to complete the tracer kinetic study.

Thiol-reactive agents have been used to modify peptides and proteins at specific sites, providing high chemoselectivity as compared with amine and carboxylate-reactive reagents (32,33). The disulfide bonds of a protein can be reduced to enable modification using thiol-specific reagents (34–36). More recently, site-directed mutagenesis was used to place cysteine residues on the surface of proteins to

provide reactive sulphydryl groups (37,38). Several thiol-reactive  $^{18}\text{F}$ -synthons have been described (24–26), all of which bear a maleimide group allowing for thiol-specific Michael addition reaction. The total synthesis time (100–150 min) and radiochemical yield (10%–20% non-decay corrected) of these synthons are comparable to  $^{18}\text{F}$ -FBEM. However, no *in vivo* data have been reported on tracers synthesized using these prosthetic groups.

We have labeled c(RGDyK) with  $^{18}\text{F}$  using  $^{18}\text{F}$ -SFB as a prosthetic group (18). The labeling yield was reasonably good for *in vivo* imaging applications. The resulting  $^{18}\text{F}$ -FB-RGD had good tumor-to-blood and tumor-to-muscle ratios but also rapid tumor washout and unfavorable hepatobiliary excretion, making it suitable only for visualizing lesions above the liver (e.g., breast cancer, head and neck cancer, and brain tumor). Because the bent conformation of c(RGDyK) has been optimized to fit into the deep cleft between the  $\alpha$ - and  $\beta$ -units of integrin  $\alpha_v\beta_3$ , it is unlikely that one can further improve integrin affinity and selectivity of the monomeric RGD peptide by fine tuning the pentapeptide configuration (39). Therefore, the polyvalency effect has been applied to develop dimeric and multimeric RGD peptides, with repeating cyclic pentapeptide

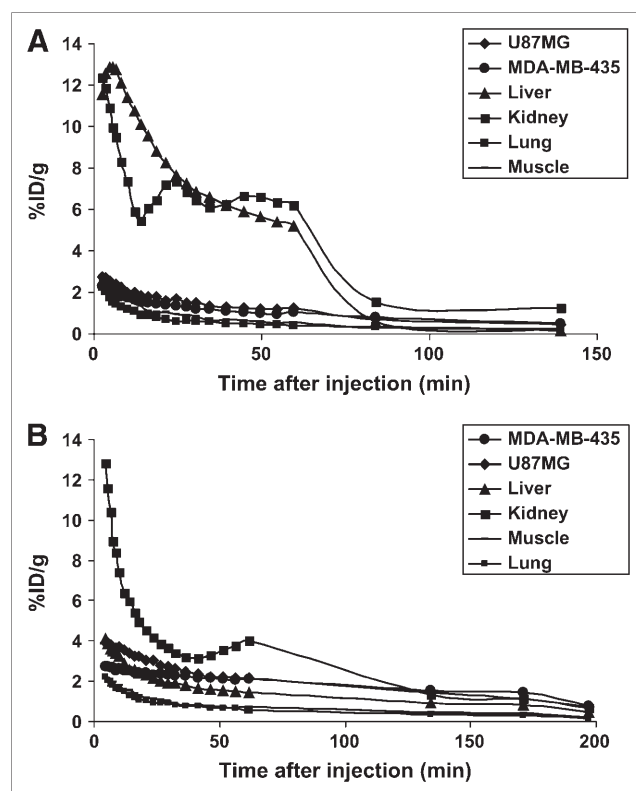


**FIGURE 5.** Time-activity curves of  $^{18}\text{F}$ -FBEM-SRGD (A) and  $^{18}\text{F}$ -FBEM-SRGD2 (B) obtained from microPET scans. The inflection point for tracer clearance is most likely due to the slower metabolism during the dynamic scan when mice were under anesthesia and body temperature was lowered.

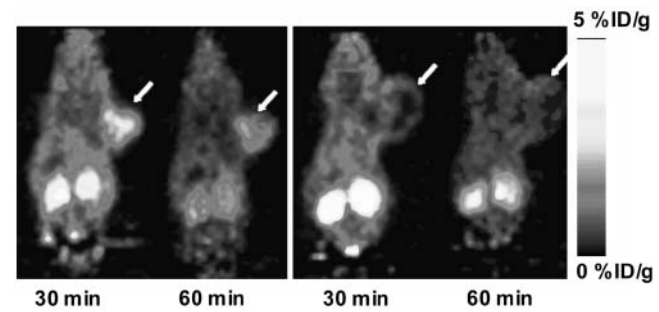


**FIGURE 6.** Ten-minute static microPET scans of U87MG tumor-bearing mice (arrows) injected with 3.7 MBq of  $^{18}\text{F}$ -FBEM-SRGD2. (Left) Control mouse. (Right) Blocking with 10 mg/kg mouse body weight of c(RGDyK).

**TABLE 1**

Extraction and Elution Efficiency Data and HPLC Analysis of Soluble Fraction of Tissue Samples at 60 Minutes After Injection of  $^{18}\text{F}$ -FBEM-SRGD2

Organ or tissue	Extraction efficiency (%)	Elution efficiency (%)	Intact fraction (%)
Blood	91.5	94.9	80.7
Urine	100.0	99.3	41.7
Liver	91.4	66.2	59.7
U87MG	91.0	66.2	77.5
Kidney	93.5	86.0	85.8

units connected by glutamates (11,12,14,19,40). We have found that  $^{18}\text{F}$ -FRGD2 ( $^{18}\text{F}$ -FB-E[c(RGDyK)]<sub>2</sub>) had predominant renal excretion and almost twice as much tumor uptake in the same animal model as compared with the monomeric tracer  $^{18}\text{F}$ -FB-RGD (11,12). The synergistic effect of polyvalency and improved pharmacokinetics may be responsible for the excellent imaging characteristics of  $^{18}\text{F}$ -FRGD2. At late time points when most of the nonspecific binding had been cleared, the tumor-to-background ratio also had a linear relationship with the tumor integrin levels, thus making it possible to quantify the tumor integrin expression level *in vivo* with static PET scans using  $^{18}\text{F}$ -FRGD2. We are currently in the process of translating  $^{18}\text{F}$ -FRGD2 into clinical trials. In parallel, we developed  $^{18}\text{F}$ -FBEM as a prosthetic group for dimeric RGD peptide labeling as well as for protein or engineered antibody labeling through site-specific Michael addition with the sulphydryl group. The reaction between  $^{18}\text{F}$ -FBEM and the thiolated RGD peptides was virtually quantitative. Although  $^{18}\text{F}$ -FBEM-SRGD2 demonstrated integrin specificity, as evidenced by effective inhibition of tumor activity accumulation in the presence of a blocking dose of integrin  $\alpha_v\beta_3$  antagonist c(RGDyK), whether it is able to quantify integrin expression *in vivo* remains to be determined in future studies. It is also worth noting that addition of the thiolated RGD peptides to  $^{18}\text{F}$ -FBEM generates a new

asymmetric center, resulting in 2 diastereomeric products. Because we only observed one sharp peak in the analytic HPLC for both  $^{18}\text{F}$ -FBEM-SRGD and  $^{18}\text{F}$ -FBEM-SRGD2, it is very likely that such a small change was not detectable by the HPLC system used.

This study demonstrated that  $^{18}\text{F}$ -FBEM could be used to efficiently label peptides through the sulphydryl group. The major advantage of  $^{18}\text{F}$ -FBEM lies in the fact that it can be applied to label a variety of peptides, proteins, or oligonucleotides containing sulphydryl groups. Because most proteins contain Cys residues, whereas those that do not can be easily engineered to incorporate a Cys residue without compromising the biologic activity, it is expected that  $^{18}\text{F}$ -FBEM will have wide applications in the near future for development of novel tracers for *in vivo* PET.

## CONCLUSION

The objective of the present work was to develop a new thiol-reactive  $^{18}\text{F}$ -labeling reagent for the prosthetic labeling of peptides and proteins via selective conjugation with a sulphydryl group.  $^{18}\text{F}$ -FBEM was thus incorporated with thiolated monomeric and dimeric RGD peptides via efficient alkylation of the free thiol group through the maleimido function. The advantage of labeling at the sulphydryl group using  $^{18}\text{F}$ -FBEM over labeling at the primary amino group using  $^{18}\text{F}$ -SFB was confirmed. The dimeric RGD peptide labeled through the  $^{18}\text{F}$ -FBEM strategy showed high integrin affinity *in vitro* and effective tumor targeting *in vivo*. The fast tracer clearance, good tumor-to-background contrast, relatively good metabolic stability, and favorable pharmacokinetics of  $^{18}\text{F}$ -FBEM-SRGD2 promise further investigation of this tracer in both preclinical and clinical settings for documenting tumor integrin expression (such as the correlation between the tumor uptake and the integrin  $\alpha_v\beta_3$  expression level *in vivo*).  $^{18}\text{F}$ -FBEM also provides a general method of labeling thiol-containing peptides, proteins, antibodies, as well as 5'-thio-functionalized oligonucleotides in high radiochemical yield and high specific activity for successful PET applications.

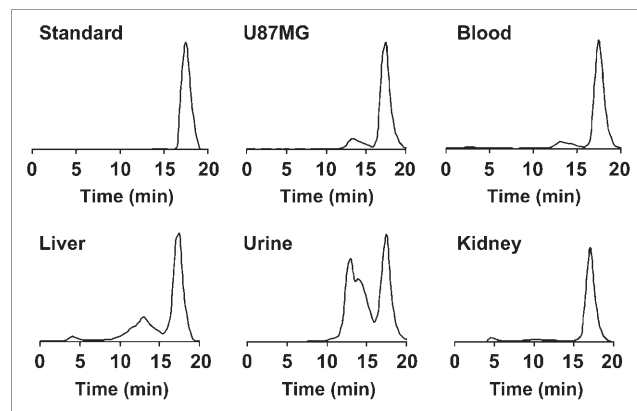


**FIGURE 7.** Metabolic stability of  $^{18}\text{F}$ -FBEM-SRGD2 in mouse blood and urine samples and in liver, kidneys, and U87MG tumor homogenates 60 min after injection. HPLC profile of tracer itself (Standard) is also shown.

## ACKNOWLEDGMENTS

This work was supported, in part, by National Institute of Biomedical Imaging and Bioengineering grant R21 EB001785, Department of Defense (DOD) Breast Cancer Research Program (BCRP) Concept Award DAMD17-03-1-0752, DOD BCRP IDEA Award W81XWH-04-1-0697, DOD Ovarian Cancer Research Program Award OC050120, DOD Prostate Cancer Research Program New Investigator Award DAMD1717-03-1-0143, American Lung Association California, Benedict Cassen Postdoctoral Fellowship from the Education and Research Foundation of the Society of Nuclear Medicine (W. Cai), National Cancer Institute (NCI) Small Animal Imaging Resource Program grant R24 CA93862, and NCI In Vivo Cellular Molecular Imaging Center grant P50 CA114747.

## REFERENCES

1. Felding-Habermann B, O'Toole TE, Smith JW, et al. Integrin activation controls metastasis in human breast cancer. *Proc Natl Acad Sci U S A.* 2001;98:1853–1858.
2. Hood JD, Cheresh DA. Role of integrins in cell invasion and migration. *Nat Rev Cancer.* 2002;2:91–100.
3. Brooks PC, Stromblad S, Sanders LC, et al. Localization of matrix metalloproteinase MMP-2 to the surface of invasive cells by interaction with integrin  $\alpha_v\beta_3$ . *Cell.* 1996;85:683–693.
4. Bogenrieder T, Herlyn M. Axis of evil: molecular mechanisms of cancer metastasis. *Oncogene.* 2003;22:6524–6536.
5. Kumar CC. Integrin  $\alpha_v\beta_3$  as a therapeutic target for blocking tumor-induced angiogenesis. *Curr Drug Targets.* 2003;4:123–131.
6. Cai W, Gambhir SS, Chen X. Multimodality tumor imaging targeting integrin  $\alpha_v\beta_3$ . *Biotechniques.* 2005;39(suppl):S6–S17.
7. Haubner RH, Wester HJ, Weber WA, Schwaiger M. Radiotracer-based strategies to image angiogenesis. *Q J Nucl Med.* 2003;47:189–199.
8. Haubner R, Wester H-J, Weber WA, et al. Noninvasive imaging of  $\alpha_v\beta_3$  integrin expression using  $^{18}\text{F}$ -labeled RGD-containing glycopeptide and positron emission tomography. *Cancer Res.* 2001;61:1781–1785.
9. Haubner R, Weber WA, Beer AJ, et al. Noninvasive visualization of the activated  $\alpha_v\beta_3$  integrin in cancer patients by positron emission tomography and  $[^{18}\text{F}]$ galacto-RGD. *PLoS Med.* [serial online]. 2005;2:e70.
10. Beer AJ, Haubner R, Goebel M, et al. Biodistribution and pharmacokinetics of the  $\alpha_v\beta_3$ -selective tracer  $^{18}\text{F}$ -galacto-RGD in cancer patients. *J Nucl Med.* 2005;46:1333–1341.
11. Chen X, Tohme M, Park R, Hou Y, Bading JR, Conti PS. Micro-PET imaging of  $\alpha_v\beta_3$ -integrin expression with  $^{18}\text{F}$ -labeled dimeric RGD peptide. *Mol Imaging.* 2004;3:96–104.
12. Zhang X, Xiong Z, Wu X, et al. Quantitative PET imaging of tumor integrin  $\alpha_v\beta_3$  expression with  $[^{18}\text{F}]$ FRGD2. *J Nucl Med.* 2006;47:113–121.
13. Chen X, Hou Y, Tohme M, et al. Pegylated Arg-Gly-Asp peptide:  $^{64}\text{Cu}$  labeling and PET imaging of brain tumor  $\alpha_v\beta_3$ -integrin expression. *J Nucl Med.* 2004;45:1776–1783.
14. Chen X, Liu S, Hou Y, et al. MicroPET imaging of breast cancer  $\alpha_v$ -integrin expression with  $^{64}\text{Cu}$ -labeled dimeric RGD peptides. *Mol Imaging Biol.* 2004;6:350–359.
15. Chen X, Park R, Hou Y, et al. MicroPET imaging of brain tumor angiogenesis with  $^{18}\text{F}$ -labeled PEGylated RGD peptide. *Eur J Nucl Med Mol Imaging.* 2004;31:1081–1089.
16. Chen X, Park R, Shahinian AH, et al.  $^{18}\text{F}$ -Labeled RGD peptide: initial evaluation for imaging brain tumor angiogenesis. *Nucl Med Biol.* 2004;31:179–189.
17. Chen X, Sievers E, Hou Y, et al. Integrin  $\alpha_v\beta_3$ -targeted imaging of lung cancer. *Neoplasia.* 2005;7:271–279.
18. Chen X, Park R, Tohme M, Shahinian AH, Bading JR, Conti PS. MicroPET and autoradiographic imaging of breast cancer  $\alpha_v$ -integrin expression using  $^{18}\text{F}$ - and  $^{64}\text{Cu}$ -labeled RGD peptide. *Bioconjug Chem.* 2004;15:41–49.
19. Wu Y, Zhang X, Xiong Z, et al. MicroPET imaging of glioma  $\alpha_v$ -integrin expression using  $^{64}\text{Cu}$ -labeled tetrameric RGD peptide. *J Nucl Med.* 2005;46:1707–1718.
20. Mading P, Fuchtnar F, Wust F. Module-assisted synthesis of the bifunctional labelling agent *N*-succinimidyl 4-[ $^{18}\text{F}$ ]fluorobenzoate ( $[^{18}\text{F}]$ SFB). *Appl Radiat Isot.* 2005;63:329–332.
21. Vaidyanathan G, Zalutsky MR. Improved synthesis of *N*-succinimidyl 4-[ $^{18}\text{F}$ ]fluorobenzoate and its application to the labeling of a monoclonal antibody fragment. *Bioconjug Chem.* 1994;5:352–356.
22. Wester HJ, Hamacher K, Stoecklin G. A comparative study of n.c.a. fluorine-18 labeling of proteins via acylation and photochemical conjugation. *Nucl Med Biol.* 1996;23:365–372.
23. Poethko T, Schottelius M, Thumshirn G, et al. Two-step methodology for high-yield routine radiohalogenation of peptides:  $^{18}\text{F}$ -labeled RGD and octreotide analogs. *J Nucl Med.* 2004;45:892–902.
24. Shiu CY, Wolf AP, Hainfeld JF. Synthesis of  $^{18}\text{F}$ -labelled *N*-(*p*-[ $^{18}\text{F}$ ]fluorophenyl)maleimide and its derivatives for labelling monoclonal antibody with  $^{18}\text{F}$ . *J Labelled Compds Radiopharm.* 1998;26:287–289.
25. de Bruin B, Kuhnast B, Hinnen F, et al. 1-[3-( $^{18}\text{F}$ )Fluoropyridin-3-yl]propylpyrrole-2,5-dione: design, synthesis, and radiosynthesis of a new [ $^{18}\text{F}$ ]fluoropyridine-based maleimide reagent for the labeling of peptides and proteins. *Bioconjug Chem.* 2005;16:406–420.
26. Toyokuni T, Walsh JC, Dominguez A, et al. Synthesis of a new heterobifunctional linker, *N*-[4-(aminoxy)butyl]maleimide, for facile access to a thiol-reactive  $^{18}\text{F}$ -labeling agent. *Bioconjug Chem.* 2003;14:1253–1259.
27. Visvikis D, Cheze-LeRest C, Costa DC, Bomanji J, Gacinovic S, Ell PJ. Influence of OSEM and segmented attenuation correction in the calculation of standardised uptake values for  $[^{18}\text{F}]$ FDG PET. *Eur J Nucl Med.* 2001;28:1326–1335.
28. Herman LW, Fischman AJ, Tompkins RG, et al. The use of pentafluorophenyl derivatives for the  $^{18}\text{F}$  labelling of proteins. *Nucl Med Biol.* 1994;21:1005–1010.
29. Schottelius M, Poethko T, Herz M, et al. First  $^{18}\text{F}$ -labeled tracer suitable for routine clinical imaging of sst receptor-expressing tumors using positron emission tomography. *Clin Cancer Res.* 2004;10:3593–3606.
30. Kilbourn MR, Dence CS, Welch MJ, Mathias CJ. Fluorine-18 labeling of proteins. *J Nucl Med.* 1987;28:462–470.
31. Shai Y, Kirk KL, Channing MA, et al.  $^{18}\text{F}$ -Labeled insulin: a prosthetic group methodology for incorporation of a positron emitter into peptides and proteins. *Biochemistry.* 1989;28:4801–4806.
32. Wilbur DS. Radiohalogenation of proteins: an overview of radionuclides, labeling methods and reagents for conjugate labeling. *Bioconjug Chem.* 1992;3:432–470.
33. Brinkley M. A brief survey of methods for preparing protein conjugates with dyes, haptens, and cross-linking reagents. *Bioconjug Chem.* 1992;3:2–13.
34. Izanaga-Escobar N. Direct radiolabeling of monoclonal antibodies with rhenium-188 for radioimmunotherapy of solid tumors: a review of radiolabeling characteristics, quality control and *in vitro* stability studies. *Appl Radiat Isot.* 2001;54:399–406.
35. Rhodes BA. Direct labeling of proteins with  $^{99m}\text{Tc}$ . *Int J Rad Appl Instrum B.* 1991;18:667–676.
36. Saito G, Swanson JA, Lee KD. Drug delivery strategy utilizing conjugation via reversible disulfide linkages: role and site of cellular reducing activities. *Adv Drug Deliv Rev.* 2003;55:199–215.
37. Bragg PD. Site-directed mutagenesis of the proton-pumping pyridine nucleotide transhydrogenase of Escherichia coli. *Biochim Biophys Acta.* 1998;1365:98–104.
38. Chorostowska-Wynimko J, Swiercz R, Skrzypczak-Jankun E, Wojtowicz A, Selman SH, Jankun J. A novel form of the plasminogen activator inhibitor created by cysteine mutations extends its half-life: relevance to cancer and angiogenesis. *Mol Cancer Ther.* 2003;2:19–28.
39. Xiong JP, Stehle T, Zhang R, et al. Crystal structure of the extracellular segment of integrin  $\alpha_v\beta_3$  in complex with an Arg-Gly-Asp ligand. *Science.* 2002;296:151–155.
40. Janssen M, Oyen WJ, Massuger LF, et al. Comparison of a monomeric and dimeric radiolabeled RGD-peptide for tumor targeting. *Cancer Biother Radiopharm.* 2002;17:641–646.

# Multimodality tumor imaging targeting integrin $\alpha_v\beta_3$

Weibo Cai, Sanjiv Sam Gambhir, and Xiaoyuan Chen  
Stanford University School of Medicine, Stanford, CA, USA

BioTechniques 39:S6-S17 (December 2005)  
doi 10.2144/000112091

The cell adhesion molecule integrin  $\alpha_v\beta_3$  is an important player in the process of tumor angiogenesis and metastasis. Antibodies, peptides, peptidomimetics, and small molecule antagonists against integrin  $\alpha_v\beta_3$  have been shown to induce endothelial apoptosis, to inhibit tumor angiogenesis, and to increase endothelial permeability. The ability to quantitatively image integrin  $\alpha_v\beta_3$  expression *in vivo* in a noninvasive manner may shed new light into the mechanism of angiogenesis and antiangiogenic treatment efficacy based on integrin antagonism. Tumor integrin expression imaging will also aid in lesion detection, patient stratification, new anti-integrin drug development/validation, as well as treatment monitoring and optimization. This review summarizes the recent advances in multimodality imaging of tumor integrin  $\alpha_v\beta_3$  expression using magnetic resonance imaging (MRI), ultrasound, near-infrared (NIR) fluorescence, single photon emission computed tomography (SPECT), and positron emission tomography (PET).

## INTRODUCTION

### Molecular Imaging

Molecular imaging refers to the characterization and measurement of biological processes at the molecular level (1,2). Conventional imaging modalities that detect anatomical and functional changes of tumor vascularity during angiogenesis, tumor growth, and upon antiangiogenic treatment provide little or no information regarding the specific molecular markers on newly formed blood vessels, tumor cells, and the molecular changes upon therapy. Molecular imaging takes advantage of traditional diagnostic imaging techniques and introduces molecular probes to determine the expression of indicative molecular markers of the tumor development at different stages (2–4). Detection of these molecular markers permits much earlier diagnosis, earlier treatment, and better prognosis. Subsequent profiling to identify suitable treatment targets could lead to individualized therapy and treatment monitoring. Molecular imaging technologies include, but are not limited to, positron emission tomography (PET), single photon emission computed tomography (SPECT), magnetic resonance imaging (MRI), magnetic resonance spectroscopy (MRS), optical bioluminescence, optical fluorescence, and ultrasound (2,5). In computed tomography (CT), the images are obtained because tissues absorb X-rays differently as they pass through the body, therefore providing mainly anatomical information. Since CT signal is rarely specific at the molecular level, it will not be discussed here.

Since many tumors are quite heterogeneous, tissue sampling does not always represent the biochemical or pathological processes of the disease. Furthermore, temporal studies usually need large numbers of animals to be sacrificed at various time points to obtain statistically significant results. Noninvasive imaging of genetic and cellular processes at the molecular level will compliment the established *ex vivo* molecular biological assays and provide both spatial and temporal dimensions to our understanding of various diseases. Two prerequisites need to be satisfied in order to image and quantify biological processes *in vivo* noninvasively: (*i*) a probe composed of a label that can be detected with high sensitivity and a ligand that binds specifically and with high affinity to the target and (*ii*) a sensitive, high-resolution imaging instrument to detect the signal noninvasively. In this review, we will highlight the recent advances in developing molecular imaging probes and techniques targeting a tumor-specific molecular marker, integrin  $\alpha_v\beta_3$ .

### Tumor Angiogenesis and Metastasis

Angiogenesis, the formation of new blood vessels from preexisting blood vessels, is a fundamental process occurring during tumor progression (6). Angiogenesis depends on the balance

between pro-angiogenic molecules [vascular endothelial growth factor (VEGF), fibroblast growth factor (FGF), epidermal growth factor (EGF), etc.] and antiangiogenic molecules (angiostatin, endostatin, etc.) (7,8). The fact that tumors are dependent on blood supply has inspired many scientists to search for antiangiogenic molecules and to design antiangiogenic strategies for cancer treatment and prevention of cancer recurrence and metastasis (9–11). Tumor angiogenesis differs significantly from physiological angiogenesis. The differences include aberrant vascular structure, altered endothelial cell-pericyte interactions, abnormal blood flow, increased permeability, and delayed maturation (6,12). Most tumors start growing as avascular dormant nodules until they reach a steady-state level of proliferating and apoptosing cells. Angiogenesis begins with perivascular detachment and vessel dilation, followed by angiogenic sprouting, new vessel formation and maturation, and the recruitment of perivascular cells. Blood-vessel formation continues as the tumor grows, feeding on hypoxic and necrotic areas of the tumor for essential nutrients and oxygen.

Cancer cells spread throughout the body by metastasis (13–16). Metastasis occurs through several steps. First, cancer cells lose E-cadherin-dependent intercellular adhesions, acquire a migratory phenotype, detach from neighboring cells, penetrate the basement membrane, and invade the interstitial matrix. Second, tumor cells penetrate into blood vessels and lymphatic vessels and enter the circulatory system, a process called intravasation. After reaching the bloodstream, tumor cells often adhere to platelets and leukocytes, forming emboli that stop in the microcirculation of target organs more easily than individual tumor cells. Finally, metastatic cells exit the bloodstream (extravasation) and undergo expansive growth within the parenchyma of the target organ.

### Role of Integrin $\alpha_v\beta_3$ During Tumor Progression

Molecules regulating angiogenesis include growth factor receptors, tyrosine kinase receptors, G protein-coupled receptors for angiogenesis modulating proteins, and integrins (6–8). Integrins are a family of adhesion molecules consisting of two noncovalently bound transmembrane subunits ( $\alpha$  and  $\beta$ ), both type I membrane proteins with large extracellular segments that pair to create heterodimers with distinct adhesive capabilities (17,18). In mammals, 18  $\alpha$  and 8  $\beta$  subunits assemble into 24 different receptors. Increasing amounts of evidence now imply that integrin signaling plays a key role in tumor angiogenesis and metastasis (19–21). Integrins expressed on endothelial cells modulate cell migration and survival during angiogenesis, while integrins expressed on carcinoma cells potentiate metastasis by facilitating invasion and movement across blood vessels. Efficient tumor invasion requires partial degradation of the extracellular matrix (ECM) at the invasion front. The matrix metalloproteinases (MMPs)

are the major proteases involved in remodeling the ECM (15). The  $\alpha_v\beta_3$  integrin, which binds to arginine-glycine-aspartic acid (RGD)-containing components of the interstitial matrix, such as vitronectin, fibronectin, and thrombospondin, is significantly up-regulated on endothelium during angiogenesis but not on quiescent endothelium (21–23). The special role of integrin  $\alpha_v\beta_3$  in tumor invasion and metastasis arises from its ability to recruit and activate MMP-2 and plasmin, which degrade components of the basement membrane and interstitial matrix (24). Research has shown that tumor expression of integrin  $\alpha_v\beta_3$  correlates well with tumor progression in several malignancies such as melanoma (25), glioma (26), ovarian cancer (27), and breast cancer (28,29). Inhibition of  $\alpha_v$ -integrin activity by monoclonal antibodies (MAbs), cyclic RGD peptide antagonists, and peptidomimetics has also been shown to induce endothelial cell apoptosis (30), to inhibit angiogenesis (20), and to increase endothelial monolayer permeability (31).

### **Integrin $\alpha_v\beta_3$ as the Imaging Target**

For a targeting approach aimed at monitoring tumor angiogenesis and metastasis, the sufficient level of accessible tumor specific targets is essential for the detection and delineation of lesions from background by imaging technologies. Integrin  $\alpha_v\beta_3$ , the most extensively studied in the integrin family, serves as an excellent molecular marker for tumor angiogenesis and metastasis imaging, since it is not readily detectable in quiescent vessels but becomes highly expressed in angiogenic vessels (19). The ability to noninvasively visualize and quantify integrin  $\alpha_v\beta_3$  expression level will provide new opportunities to document tumor (tumor cells and sprouting tumor vasculature) integrin expression, to more appropriately select patients for anti-integrin treatment, and to monitor treatment efficacy in integrin-positive patients. Several review articles on tumor angiogenesis imaging have partially covered some integrin targeting approaches (32,33). In this review article, recent advances in both nonradionuclide (MRI, ultrasound, and optical) and radionuclide imaging (SPECT and PET) of tumor integrin  $\alpha_v\beta_3$  will be summarized.

## **NONRADIONUCLIDE IMAGING OF INTEGRIN $\alpha_v\beta_3$ EXPRESSION**

### **Magnetic Resonance Imaging**

The major advantage of MRI over radionuclide or optical imaging is its higher spatial resolution (usually submillimeter level). However, MRI is many orders of magnitude less sensitive than radionuclide and optical techniques, which means that much larger amounts of molecular probes must be retained at the target for detectable MRI signal (34). High mass amounts of probe can be toxic, and this must be carefully studied before any MRI probe is translated into the clinic. The inherent low sensitivity of MRI can be only partially compensated by working at relatively high magnetic fields (4.7–14 T), using hardware and software dedicated to small animal imaging and much longer acquisition times during imaging.

In an animal model, Sipkins et al. first demonstrated the use of antibody-coated paramagnetic liposomes (300–350 nm in diameter) containing Gd<sup>3+</sup> for MRI imaging of integrin  $\alpha_v\beta_3$  expression (35). Imaging of a rabbit model of squamous cell carcinomas (V2) was achieved by directly targeting paramagnetic agents to the angiogenic vasculature using LM609, a mouse anti-human integrin  $\alpha_v\beta_3$  MAb (Figure 1). Anderson et. al. (36) also reported site-directed contrast enhancement of angiogenic vessels *in vivo* using antibody-coated MRI contrast agent. The targeted contrast agent consists of Gd-perfluorocarbon nanoparticles conjugated to integrin  $\alpha_v\beta_3$  antibody DM101 (400–700 nm in diameter). The study was carried out in a rabbit corneal micropocket model, where neovasculature

was induced in the cornea using basic FGF. However, only a modest increase (<25%) in the average MR signal intensity was observed after 90 min.

Winter et al. attached peptidomimetic integrin  $\alpha_v\beta_3$  antagonist to magnetic nanoparticles for MRI imaging under common clinical field strength of 1.5 T (37,38). Two animal models were used, New Zealand white rabbits implanted with Vx-2 tumors and an atherosclerosis model. In the Vx-2 model, integrin  $\alpha_v\beta_3$ -targeted paramagnetic nanoparticles increased MRI signal dramatically in the periphery of the tumor at 2 h postinjection (p.i.). Similar increases in MR contrast were also observed within the walls of some vessels proximate to the tumor. Despite the relatively large size (about 270 nm in diameter), these nanoparticles penetrated into the leaky tumor neovasculature but did not migrate into the interstitium in an appreciable amount, since only marginal increase in MR signal was observed at 2 h (characteristic of passive targeting rather than integrin-specific targeting). Immunohistochemistry of integrin  $\alpha_v\beta_3$  confirmed the extent and distribution of neovascularity observed by MRI. In the atherosclerosis model, enhancement in the MRI signal was also observed among rabbits that received integrin-targeted nanoparticles. Histology and immunohistochemistry confirmed the proliferation of angiogenic vessels within the aortic adventitia of the atherosclerotic rabbits as compared with control animals. Since this integrin-targeting nanoparticle system can carry a variety of drugs in its lipid membrane, it may have potential for simultaneous molecular imaging and site-directed drug delivery for early atherosclerotic disease.

Very recently, athymic nude mice bearing human melanoma tumors were also imaged using systemically injected  $\alpha_v\beta_3$  integrin-targeted paramagnetic nanoparticles (25). Contrast enhancement of neovascularity in animals that received targeted nanoparticles increased significantly by 2 h as compared with nontargeted paramagnetic nanoparticles. MRI results were also supported by histology. This technique may be employed to noninvasively detect small regions of angiogenesis associated with nascent melanoma tumors, as well as to phenotype and to stage other integrin-positive tumors in a clinical setting.

In all these studies, the targeted paramagnetic nanoparticles are coated with either antibodies or small peptidic/peptidomimetic integrin  $\alpha_v\beta_3$  antagonists. Coating the paramagnetic nanoparticles with peptides or peptidomimetics is potentially better than antibodies, since hundreds even thousands of peptides/peptidomimetics can be attached to the nanoparticles, which leads to much higher local concentration of the ligand and higher binding affinity. Moreover, not only do antibodies add to the already large size of the nanoparticle contrast agents, antibody-coated contrast agents also stay in the circulation system much longer while peptide- or peptidomimetics-coated contrast agents home to the target faster and that gives better contrast.

### **Ultrasound**

Because of its low cost, high availability, and safety, ultrasonography is the most commonly used clinical imaging modality. High-frequency (>20 kHz) sound waves are emitted from a transducer placed against the skin, and ultrasound images are obtained based on the sound wave reflected back from the internal organs (39). The ultrasound contrast is dependent on the sound speed, sound attenuation, backscatter, and the imaging algorithm. Ultrasound imaging using diagnostic ultrasound instrumentation operated in the 7.5–15 MHz frequency range has been applied to several small animal models.

Ellegala et al. reported the ultrasound imaging of tumor angiogenesis using integrin  $\alpha_v\beta_3$ -targeted microbubbles (40). Athymic nude rats were inoculated intracerebrally with U87MG human glioma cells. On 2 or 4 weeks after implantation, contrast-enhanced ultrasound (CEU) was performed using microbubbles (3–4  $\mu$ m

in diameter) targeted to integrin  $\alpha_v\beta_3$  by surface conjugation of echistatin, a disintegrin containing an RGD sequence that can be recognized by many membrane-associated adhesion receptors including integrin  $\alpha_v\beta_3$ . CEU perfusion imaging using nontargeted microbubbles was also performed to determine tumor microvascular blood volume and blood velocity. It was found that CEU signal from targeted microbubbles in tumors increased significantly from 2 to 4 weeks. The signal was highest at the periphery of tumors, where  $\alpha_v$ -integrin expression was most prominent based on immunohistochemistry, which correlated well with tumor microvascular blood volume. In another study, the integrin  $\alpha_v$ -targeting microbubbles were prepared by conjugating echistatin (MBE) or the MAb against murine  $\alpha_v$  (MBA) to the surface (41). Control microbubbles (MBC) were also prepared. The microvascular behavior of these microbubbles was assessed by intravital microscopy of the cremaster muscle in mice treated for 4 days with the sustained release of FGF-2. It was observed that microvascular retention was much greater for MBE and MBA than MBC, where the microbubble retention was minimal. The signal from targeted microbubbles (MBE and MBA) also correlated quite well with the blood volume determined by CEU perfusion imaging. In yet another study, hindlimb ischemia was produced in rats by ligation of an iliac artery (42). Immediately after ligation and at subsequent intervals from 4 to 28 days, targeted CEU imaging of integrin expression was performed using microbubbles conjugated with echistatin. It was observed that iliac artery ligation led to a 65%–70% reduction in blood flow and oxygen tension. In untreated ischemic muscle, blood flow and oxygen tension partially recovered by weeks 2 to 4, and signal from integrin-targeted microbubbles reached maximum between 4 to 7 days, which was before the blood flow increase. FGF-2-treated muscle had a greater rate and extent of blood flow recovery and greater signal intensity from integrin-targeted microbubbles as compared to control animals.

Since acoustic destruction of “payload-bearing” microbubbles may be used to deliver drugs or to augment gene transfection (43), angiogenesis-targeted microbubbles may also have applications in site-specific therapy for ischemic tissues or tumors. Of course, further characterization of integrin  $\alpha_v$ -targeted microbubbles in physiological models of ischemia or tumor angiogenesis is needed to validate these potential applications. So far, it is still unclear whether this approach will lead to additional diagnostic and prognostic information compared to those already used in the clinic.

### Optical Imaging

One advantage of optical imaging is that multiple probes with different spectral character could potentially be used for multichannel imaging. The major drawback of optical imaging of living subjects is the poor tissue penetration of light. Due to the limited penetration and intense scattering of light, optical imaging will be only possible in humans in limited sites such as the tissues and lesions close to the surface of the skin, tissues accessible by endoscopy, and intraoperative visualization. Even though optical imaging may not be widely used in clinical settings, near-infrared (NIR; 700–900 nm) approaches provide opportunities for rapid and cost-effective preclinical evaluation in small animal models before the more costly radionuclide-based imaging studies, since the absorbance spectra for all biomolecules reach minima in the NIR region, which provides a clear window for *in vivo* optical imaging (44). Charged-coupled device (CCD) cameras have been developed to more efficiently detect the light emitted from the body (45), and fluorescence-mediated tomography has also been developed recently (46). The subject is exposed to continuous wave or pulsed light from different sources, and multiple detectors arranged in a spatially defined order in an imaging chamber are used to capture the emitted light. Mathematical processing of this information gives the reconstructed

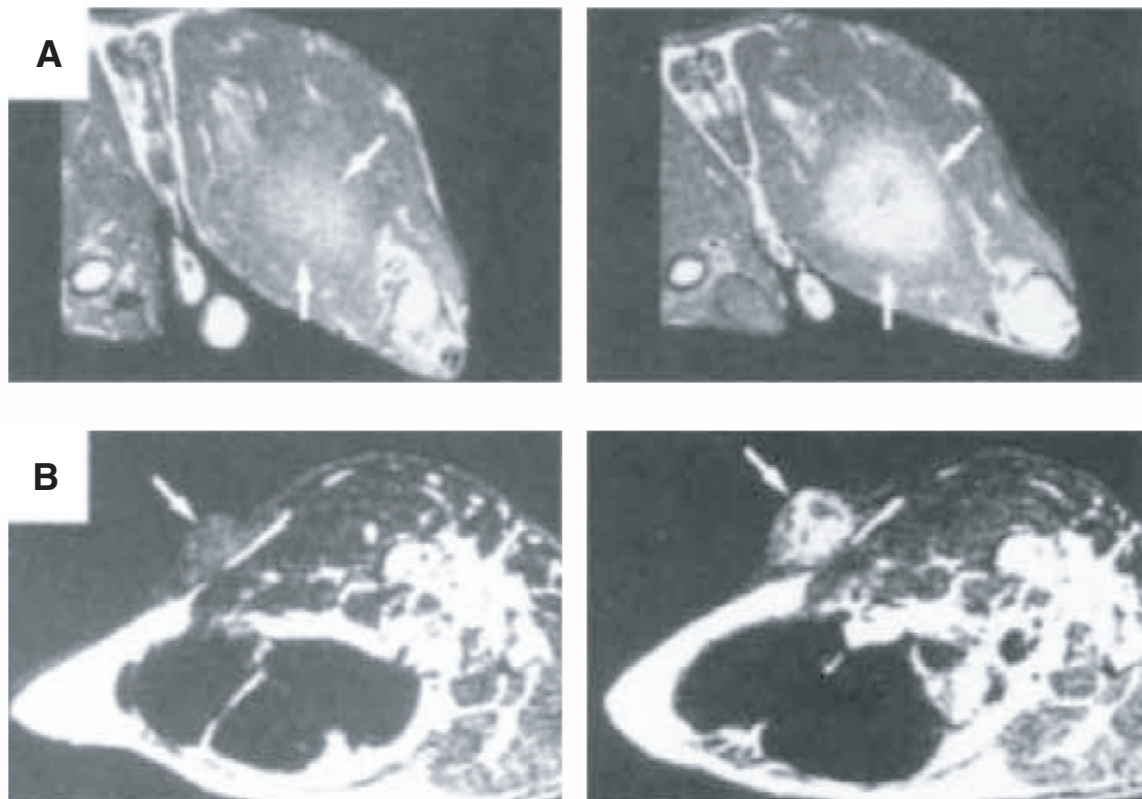


**Figure 1. Magnetic resonance imaging (MRI) of tumor angiogenesis *in vivo*.** (A) Axial images of an intramuscular tumor before (left) and after (right) administration of integrin  $\alpha_v\beta_3$ -targeted liposomes. (B) Visualization of a subcutaneous tumor precontrast (left) and postcontrast (right). Adapted from Reference 35.

tomographic image. Improvement in the algorithm and extensive mathematical validation is needed for practical implementation.

We first demonstrated that NIR fluorescent dye Cy™5.5 conjugated cyclic RGD peptide could be used to visualize subcutaneously (s.c.) inoculated integrin-positive tumors (Figure 2) (47). In vivo imaging with a prototype three-dimensional (3-D) small-animal imaging system visualized subcutaneously U87MG glioblastoma xenograft with a broad range of concentrations of fluorescent probe administered via the tail vein. The intermediate dose (0.5 nmol) produced better tumor contrast than the high dose (3 nmol) and the low dose (0.1 nmol) during 30 min to 24 h p.i., because of partial self-inhibition of receptor-specific tumor uptake at high dose and the presence of significant amount of background fluorescence at low dose, respectively. Subsequently, Wang et al. also reported optical imaging of tumor xenografts using an integrin  $\alpha_v\beta_3$ -targeted peptide c(KRGDF) labeled with fluorescent dyes Cy5.5 and IRDye800 (48,49). In vitro, the peptide-dye conjugates bound specifically to integrin  $\alpha_v\beta_3$ -positive tumor cells. When administered intravenously (i.v.) into mice, dynamic imaging revealed that Cy5.5-c(KRGDF) was rapidly taken up by KS1767 tumor (human Kaposi's sarcoma) after bolus injection, and the uptake of Cy5.5-c(KRGDF) in tumor regions were linearly increased with a dose of up to 1.5 nmol/mouse (possibly integrin receptor saturation above this dose). However, the tumor-to-background ratio was modest, and very low contrast was observed in another integrin  $\alpha_v\beta_3$ -positive M21 human melanoma tumor.

Burnett et al. (50) also reported the use of integrin  $\alpha_v\beta_3$ -targeted optical probes both in vitro and in vivo. A series of aliphatic carbamate derivatives of the nonpeptide integrin antagonists were synthesized, and the binding affinity was determined by enzyme-linked immunoabsorbent assay (ELISA) and cell adhesion inhibition assays. They observed that a hydrophobic carbamate linker increased the binding affinity of the parent compound for integrin  $\alpha_v\beta_3$  by 2- to 20-fold and demonstrated that the probe with a neopentyl linker exhibited increased binding affinity and significant tumor cell uptake in vitro as well as specific tumor accumulation and retention in vivo. Very recently, Achilefu et al. (51) discovered that

conjugating a presumably inactive linear hexapeptide GRDSPK with an NIR carbocyanine molecular probe yielded Cyp-GRD that targets integrin  $\alpha_v\beta_3$ -positive tumors. In vivo, Cyp-GRD selectively accumulated in tumors. Blocking studies with c(RGDFV) inhibited the uptake of Cyp-GRD, suggesting that both compounds target the same site of integrin  $\alpha_v\beta_3$ . Surprisingly, neither a Cypate-labeled linear RGD peptide nor an  $^{111}\text{In}$ -labeled DOTA-GRD conjugate exhibited specific tumor targeting. Ex vivo redox studies suggested that the probe accumulation level in integrin  $\alpha_v\beta_3$ -positive tumors might be correlated with mitochondrial NADH concentration. More experiments need to be carried out to fully understand this phenomenon, and a docking experiment is needed to confirm whether Cyp-RGD actually binds to the RGD binding domain in integrin  $\alpha_v\beta_3$ .

Quantum dots (QDs) with size- and composition-tunable fluorescence emission have high quantum yields and photostability suitable for optical imaging and multiplexing (52). We (53) labeled QD705 (emission wavelength 705 nm) with a monomeric RGD peptide c(RGDyK), and the resulting conjugate QD705-RGD was tested for in vitro staining of several cancer cell lines, ex vivo tissue staining, and in vivo tumor targeting. The in vitro cell staining experiments demonstrated the specific integrin targeting ability of QD705-RGD, and the fluorescence intensity correlated well with the integrin level of the cell lines. The tumor signal of QD705-RGD in nude mice U87MG xenografts steadily increased during the first several hours and reached a peak at 6 h (tumor-to-muscle ratio of about 3.6). QD705 had minimal tumor uptake, and no enhancement was found throughout the study as compared to muscle. Most of the injected particles accumulated in the liver, spleen, bone marrow, and lymphatic systems, suggesting that the mononuclear phagocytes of the reticuloendothelial system (RES), which can mediate nonspecific uptake of circulating particulates are involved in the clearance of some of the circulating QD705 and QD705-RGD particles in the mice (54). Based on these results, an approach that takes advantage of the high integrin targeting efficacy of the cyclic RGD peptides, high stability and brightness of QD, and emission wavelength in the NIR window will have great potential in cancer diagnosis and imaging as well as imaging-guided surgery and therapy.

## RADIOMUCLEIDE IMAGING OF INTEGRIN $\alpha_v\beta_3$ EXPRESSION

### Single Photon Emission Computed Tomography

As its name suggests (single photon emission), the source of SPECT images are  $\gamma$ -ray emissions (55). Internal radiation is administered through a low mass amount of pharmaceutical labeled with a radioactive isotope, which is then inhaled, ingested, or injected. The radioactive isotope decays and emits  $\gamma$ -rays, which can be detected by a  $\gamma$ -camera. The  $\gamma$ -camera can be used in planar imaging to obtain two-dimensional (2-D) images, or in SPECT imaging, to obtain 3-D images. The first object that an emitted  $\gamma$ -photon encounters after exiting the body is the collimator that allows it to travel only along certain directions to reach the detector, to ensure that the

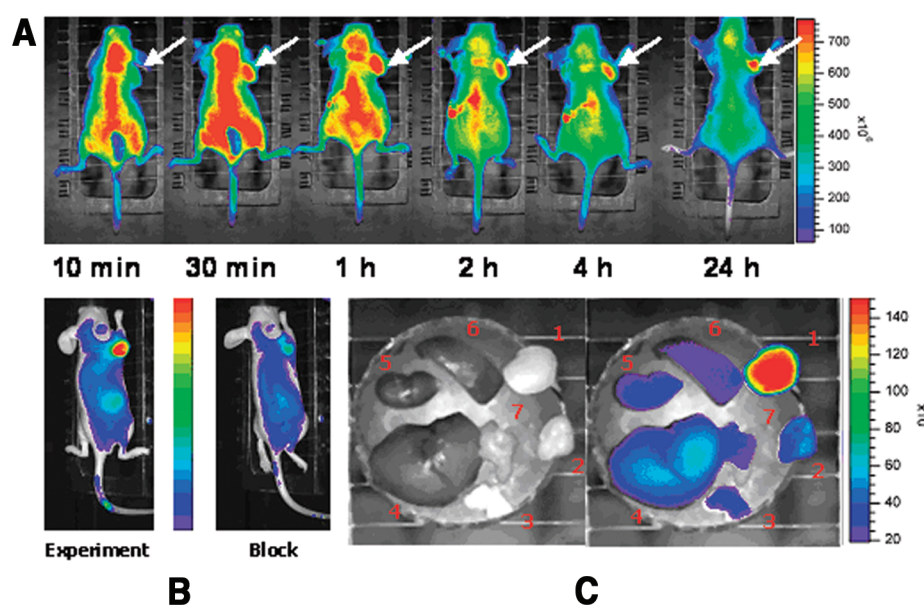


**Figure 2. In vivo and ex vivo optical imaging of tumor xenografts.** (A) In vivo near-infrared (NIR) fluorescence imaging of subcutaneously (s.c.) U87MG tumor bearing athymic nude mice after intravenously (i.v.) injection of arginine-glycine-aspartic acid (RGD)-Cy5.5 conjugate (3 nmol). (B) Representative NIR images (60° mounting angle) of tumor mice demonstrating blocking of RGD-Cy5.5 (0.5 nmol) uptake in the tumors by co-injection of 10 mg/kg mice body weight of c(RGDyK). Pseudocolor fluorescence images of tumor bearing mice were acquired 4 h postinjection (p.i.) of RGD-Cy5.5 (left, experiment) or RGD-Cy5.5 + RGD (right, block). (C) Representative images of dissected organs of a tumor mouse sacrificed 4 h p.i. 1, U87MG tumor; 2, muscle; 3, pancreas; 4, liver; 5, kidney; 6, spleen; 7, lung. Adapted from Reference 47.

position on the detector accurately represents the source of the  $\gamma$ -ray. SPECT imaging has a very low detection efficiency of  $<10^{-4}$  times the emitted number of  $\gamma$ -rays because of the use of lead collimators to define the angle of incidence. However, the advantage of SPECT imaging is that it allows simultaneous imaging of multiple radionuclides since  $\gamma$ -rays emitted from different radioisotopes can be differentiated based on the energy.

Janssen and coworkers (56) studied the in vivo behavior of the radiolabeled dimeric RGD peptide E[c(RGDfK)]<sub>2</sub> in the subcutaneous NIH:OVCAR-3 ovarian carcinoma xenograft model in BALB/c nude mice. <sup>111</sup>In/<sup>90</sup>Y and <sup>99m</sup>Tc were incorporated through DOTA and hydrazinonicotinamide (HYNIC) chelators, respectively (Figure 3). Tumor uptake was as high as 7.5% injected dose (ID)/g (<sup>111</sup>In-DOTA-E[c(RGDfK)]<sub>2</sub>) at 2 h p.i. or 6.0% ID/g (<sup>99m</sup>Tc-HYNIC-E-[c(RGDfK)]<sub>2</sub>) at 1 h p.i.. A single injection of <sup>90</sup>Y-DOTA-E-[c(RGDfK)]<sub>2</sub> at 37 MBq in mice with small subcutaneous tumors caused a significant growth delay as compared with control mice. However, increasing the number of injections did not improve the therapeutic efficacy (57,58). Moreover, the prominent renal uptake limits its potential in clinical applications. Multimeric RGD peptides with even higher receptor affinity and longer tumor retention time might be more suitable for clinical translation.

RP748, an <sup>111</sup>In-labeled quinolone that binds to integrin  $\alpha_v\beta_3$  with high affinity, was recently studied both in vitro and in vivo to track injury-induced vascular proliferation in rodents (59). This tracer exhibits selective binding to activated  $\alpha_v\beta_3$  integrin, and activation of integrin  $\alpha_v\beta_3$  by Mn<sup>2+</sup> led to increased cell binding. RP748 was then injected into mice at 1, 3, or 4 weeks after left carotid injury, and carotids were harvested for autoradiography. It was found that the relative autographic intensity was higher at 1 and 3 weeks and

decreased significantly by 4 weeks after injury. Carotid  $\alpha_v$  and  $\beta_3$  integrin expression peaked at 1 week and decreased by 4 weeks after injury. The proliferation index obtained from Ki67 staining exhibited a temporal pattern that correlates to RP748 uptake. In vivo imaging of this radiolabeled integrin  $\alpha_v\beta_3$ -targeting agent was performed in a canine model of postinfarction angiogenesis (60). Serial in vivo dual-isotope SPECT imaging with RP748 and <sup>99m</sup>Tc-MIBI demonstrated focal radiotracer uptake in hypoperfused regions where angiogenesis was stimulated. A 4-fold increase in myocardial radiotracer uptake in the infarct region was observed, which was confirmed by histological staining of  $\alpha_v\beta_3$  integrin. These results demonstrated in vivo imaging of vascular cell proliferation-associated states, whether focal, as in postangioplasty re-stenosis, or diffuse, as in pulmonary hypertension, which may lead to better understanding of pathophysiology, development of novel paradigms for management of cardiovascular disease, as well as better risk stratification of patients following myocardial infarction.

### Positron Emission Tomography

To date, most of integrin targeted PET studies have been focused on the radiolabeling of RGD peptide antagonists of integrin  $\alpha_v\beta_3$  due to its high binding affinity (nanomolar to subnanomolar range for monomeric and multimeric RGD peptides) (61–64). For early lesion detection, acquisition of higher count statistics is particularly valuable for detecting the fewest possible cells per unit volume with the least amount of radioactivity. The sensitivity of PET is very high ( $10^{-11}$ – $10^{-12}$  M), and there is no depth limitation for detecting tumor signal (1,65). Therefore, PET imaging of tumor integrin expression is the most extensively studied among all the modalities described above. The current status of RGD-based PET probe development is reviewed next.

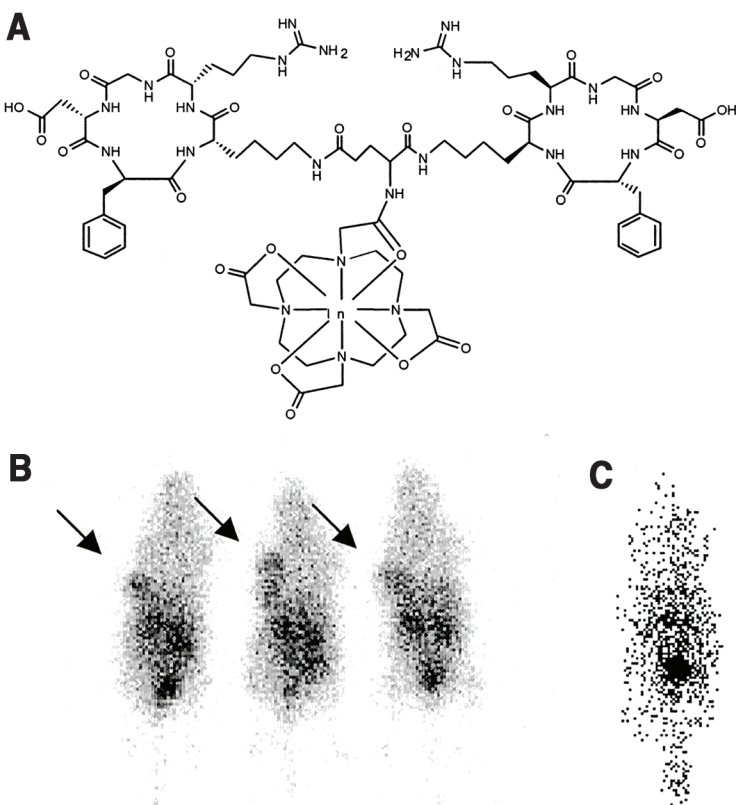


**Figure 3. In vivo tumor imaging using <sup>111</sup>In-labeled tracer.** (A) Structure of <sup>111</sup>In-DOTA-E-[c(RGDfK)]<sub>2</sub>. (B) Scintigraphic image of three athymic BALB/c mice with a subcutaneous NIH:OVCAR-3 tumor 2 h after injection of 1.8 MBq <sup>111</sup>In-DOTA-E-[c(RGDfK)]<sub>2</sub>, tumors are pointed out by arrows. Prominent activity accumulations in the kidneys, liver, and intestines are also obvious. (C) Mouse injected with 1.8 MBq of the <sup>111</sup>In-labeled scrambled peptide DOTA-E-[c(RGKfD)]<sub>2</sub> showed no significant tumor uptake. Adapted from Reference 56.

### <sup>18</sup>F-Labeled RGD Peptides

Monomeric RGD peptide c(RGDyV) was first labeled by Haubner et al. (61) with <sup>125</sup>I. This tracer had rapid tumor washout and unfavorable hepatobiliary excretion due to its high lipophilicity, which limited its further application. Glycosylation on the lysine side chain of a similar RGD peptide c(RGDfK) decreased the lipophilicity and the hepatic uptake (66). Another glycopeptide based on c(RGDfK) was then labeled with <sup>18</sup>F via 2-[<sup>18</sup>F]fluoropropionate prosthetic group, and the resulting [<sup>18</sup>F]galacto-RGD (Figure 4A) exhibited integrin  $\alpha_v\beta_3$ -specific tumor uptake in integrin-positive M21 melanoma xenograft model (62,67,68). It was also demonstrated that [<sup>18</sup>F]galacto-RGD is sensitive enough to visualize  $\alpha_v\beta_3$  expression resulting exclusively from the tumor vasculature using an A431 human squamous cell carcinoma model, in which the tumor cells are integrin negative. Quantitative analysis showed that uptake of [<sup>18</sup>F]Galacto-RGD in the melanoma model is related to  $\alpha_v\beta_3$  expression as determined by Western blot analyses. Initial clinical trials in healthy volunteers and a limited number of cancer patients revealed that this tracer can be safely administered to patients and is able to delineate certain lesions that are integrin-positive with reasonable contrast (62,69). Therefore, this approach may help in planning and optimizing therapeutic strategies targeting the  $\alpha_v\beta_3$  integrin.

Despite the successful translation of [<sup>18</sup>F]Galacto-RGD into clinical trials, several key issues remain to be resolved. (i) Tumor targeting efficacy—as a monomeric RGD peptide tracer, it has relatively low integrin binding affinity and only modest tumor standard uptake values (SUVs). Therefore, tumors with low integrin expression level may not be detectable. (ii) Pharmacokinetics—although glycosylation improved the pharmacokinetic behavior of the tracer to a

certain degree, prominent activity accumulation in the liver, kidneys, spleen, and intestines was still observed in both preclinical models and human studies, which makes it difficult to visualize lesions in the abdomen. (iii) Quantification of integrin density—it is unclear whether the tumor contrast from [<sup>18</sup>F]galacto-RGD/PET is a true reflection of tumor integrin  $\alpha_v\beta_3$  expression level in vivo. In the preclinical M21/M21-L model, there is moderate correlation between tumor/background ratios (obtained from PET) and relative integrin  $\alpha_v\beta_3$  expression level (from Western blot analyses) (Figure 4, B and C). In the clinical trial, the kinetic modeling was carried out using a two-tissue compartment model for the tumors and a one-tissue compartment model for the muscle. The tracer uptake does not seem to correlate with melanoma patient tumor grading and the tumor metastatic potential. As shown in Figure 4D, a patient with malignant melanoma stage IV and multiple metastases in the liver, skin, and lower abdomen showed virtually no uptake of [<sup>18</sup>F]Galacto-RGD, while in Figure 4E, a patient with malignant melanoma stage IIIb and a solitary lymph node metastasis in the right axilla can be detected.

Sutcliffe-Goulden et al. (70) labeled a linear RGD peptide with <sup>18</sup>F via solid-phase synthesis. Unfortunately, low metabolic stability and low avidity of the linear RGD peptide did not give tumor contrast. RGD peptides have also been labeled with <sup>18</sup>F through electrophilic substitution method (71). The direct fluorination strategy resulted in multiple side products that were difficult to purify by high-performance liquid chromatography (HPLC). The low specific activity of the carrier-added product, in particular, makes such tracers unsuitable for in vivo integrin imaging.

We labeled c(RGDyK) with <sup>18</sup>F through a fluorobenzoyl prosthetic group (Figure 5) (26,29,72). The resulting [<sup>18</sup>F]FB-RGD had good tumor-to-blood and tumor-to-muscle ratios but also rapid tumor washout and unfavorable hepatobiliary excretion, making it only suitable for visualizing lesions above the liver (e.g., breast cancer,

head and neck cancer, and brain tumor). Rather than introducing an amino sugar moiety to increase the hydrophilicity (62,67), an amphiphilic polyethylene glycol (PEG) linker (MW = 3400) was incorporated to improve the pharmacokinetics (26,73). PEGylation significantly prolonged tumor retention without compromising the desired rapid clearance of radioactivity from liver and kidneys, yet it also reduced the receptor binding affinity of the RGD peptide. The overall effect is that the tumor uptake is comparable to the unmodified monomeric RGD peptide but with improved pharmacokinetics. One disadvantage is that PEG is not a monodisperse compound, which makes complete characterization of the tracer more difficult.

Since c(RGDyK) gives better in vivo imaging results than c(RGDFK), due to its increased hydrophilicity (D-Tyr is more hydrophilic than D-Phe), which gives lower liver uptake, and the bent conformation of both peptides has been optimized to fit into the deep cleft between the  $\alpha$  and  $\beta$  units of integrin  $\alpha_v\beta_3$ , it is unlikely that one can further improve integrin affinity and selectivity of the monomeric RGD peptide by fine-tuning the pentapeptide configuration (22,74). Polyvalency effects have been applied to develop dimeric and multimeric RGD peptides, with repeating cyclic pentapeptide units connected by glutamates (28,56–58,63,75,76). Indeed, the dimeric RGD peptide E[c(RGDyK)]<sub>2</sub> exhibited one order of magnitude higher binding affinity than the corresponding monomer c(RGDyK). [<sup>18</sup>F]FB-E[c(RGDyK)]<sub>2</sub> (abbreviated as [<sup>18</sup>F]FRGD2) (Figure 6A) had predominant renal excretion and almost twice as much tumor uptake in the same animal model as compared to the monomeric tracer [<sup>18</sup>F]FB-c(RGDyK). The synergistic effect of polyvalency (77) and improved pharmacokinetics may be responsible for the excellent imaging characteristics of [<sup>18</sup>F]FRGD2 (Figure 6B).

In order to quantify integrin  $\alpha_v\beta_3$  expression level in vivo, graphical analyses of the dynamic microPET scans in several tumor xenograft models, such as glioma, breast cancer, prostate cancer, and non-small cell lung cancers were performed (78). The Logan

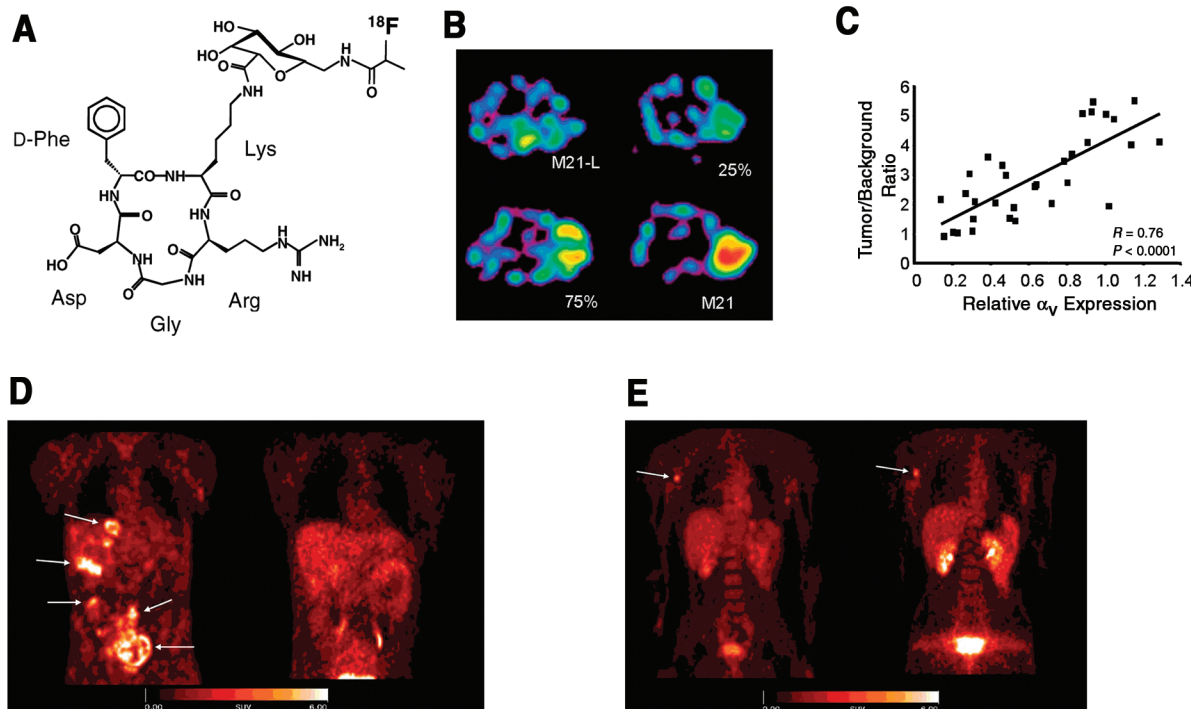


**Figure 4. Integrin  $\alpha_v\beta_3$  expression imaging in cancer patients using an RGD-based tracer.** (A) Structure of [<sup>18</sup>F]Galacto-RGD. (B) Transaxial images of nude mice bearing tumors with increasing amounts of  $\alpha_v\beta_3$ -positive M21 cells (0% [M21-L], 25%, 75%, and 100% [M21]) 90 min postinjection (p.i.) obtained from a small-animal positron emission tomography (PET) scanner show increasing tracer uptake in the tumor. (C) The correlation between tumor/background ratios (obtained from PET) and relative integrin  $\alpha_v\beta_3$  expression (obtained from Western blot analyses). (D) A patient with malignant melanoma stage IV and multiple metastases in the liver, skin, and lower abdomen (arrows) showed marked uptake of [<sup>18</sup>F]FDG (left panel) but virtually no uptake of [<sup>18</sup>F]Galacto-RGD (right panel) using a clinical PET camera. (E) A patient with malignant melanoma stage IIIb and a solitary lymph node metastasis in the right axilla can be detected by both [<sup>18</sup>F]FDG (left panel) and [<sup>18</sup>F]Galacto-RGD (right panel). RGD, arginine-glycine-aspartic acid. Adapted from Reference 62.

plot (79) (Figure 6C) gave better fit than the Patlak analysis (80), reflecting the reversible binding characteristics of [<sup>18</sup>F]FRGD2. Since <sup>125</sup>I-echistatin forms a sodium dodecyl sulfate (SDS)-stable complex with integrin  $\alpha_v\beta_3$  (resistant to 0.6% SDS) in the absence of chemical cross-linkers, reducing conditions and heating (81), the tumor integrin density can be quantified by SDS polyacrylamide gel electrophoresis (SDS-PAGE)/autoradiography using <sup>125</sup>I-echistatin as radioligand. The binding potential (BP) thus calculated from the Logan plot correlated well with the receptor density measured from receptor autoradiography (Figure 6D). Most importantly, at late time points when most of the nonspecific binding had been cleared, the tumor-to-background ratio also had a linear relationship with the tumor integrin levels (Figure 6F), thus making it possible to quantify tumor integrin expression level *in vivo* with static PET scans and [<sup>18</sup>F]FRGD2. Whether this tracer [<sup>18</sup>F]FRGD2 will be translated into the clinic to correlate between tumor-to-background ratios or SUVs and tumor integrin expression level remains to be determined.

The initial clinical trial of [<sup>18</sup>F]Galacto-RGD boasts promising future of RGD-based PET tracer for *in vivo* tumor imaging. This tracer gives good contrast in most regions of the body except for the urogenital tract and the liver and spleen, even though the tracer itself is not quite optimal. Multimeric RGD peptides have been reported to exhibit increased binding affinities *in vitro* and improved tumor accumulation and tumor-to-background ratios in preclinical rodent models as compared with the monomeric compounds (28,58,63,64,78). Therefore, it is necessary to

perform a side-by-side comparison to determine whether multimeric RGD-based tracers such as [<sup>18</sup>F]FRGD2 may exhibit more specific and more sensitive tumor targeting in both the preclinical rodent model and in clinical trials. It is very likely that the multimeric ligand approach will be used for performance optimization of RGD-based PET tracer development.

#### <sup>64</sup>Cu-Labeled RGD Peptides

For PET imaging of integrin  $\alpha_v\beta_3$  expression, <sup>18</sup>F-labeled RGD peptides will likely be the first choice, since [<sup>18</sup>F]F- is readily available from most medical cyclotron facilities. In addition to <sup>18</sup>F-labeled RGD peptides, <sup>64</sup>Cu- and <sup>86</sup>Y-labeled RGD peptides are also of considerable interest. <sup>64</sup>Cu [ $t_{1/2} = 12.7$  h;  $\beta^+ = 655$  keV (19%);  $\beta^- = 573$  keV (40%)] is an attractive radionuclide for both PET imaging and targeted radiotherapy of cancer (82) while <sup>86</sup>Y ( $t_{1/2} = 14.7$  h) is usually used as a substitute of <sup>90</sup>Y for pharmacokinetics and dosimetry studies (83). PET imaging of tumors with low doses of <sup>64</sup>Cu-labeled RGD peptides could also be utilized to determine individual radiation dosimetry prior to therapy with either high dose <sup>64</sup>Cu- or <sup>67</sup>Cu-labeled RGD peptides.

We initially labeled the DOTA-c(RGDyK) conjugate with <sup>64</sup>Cu for breast cancer imaging (29). The radiotracer exhibited moderate tumor uptake with prominent liver and kidney retention. The PEGylated analog, <sup>64</sup>Cu-DOTA-PEG-c(RGDyK) showed significantly reduced hepatic activity accumulation, higher renal uptake

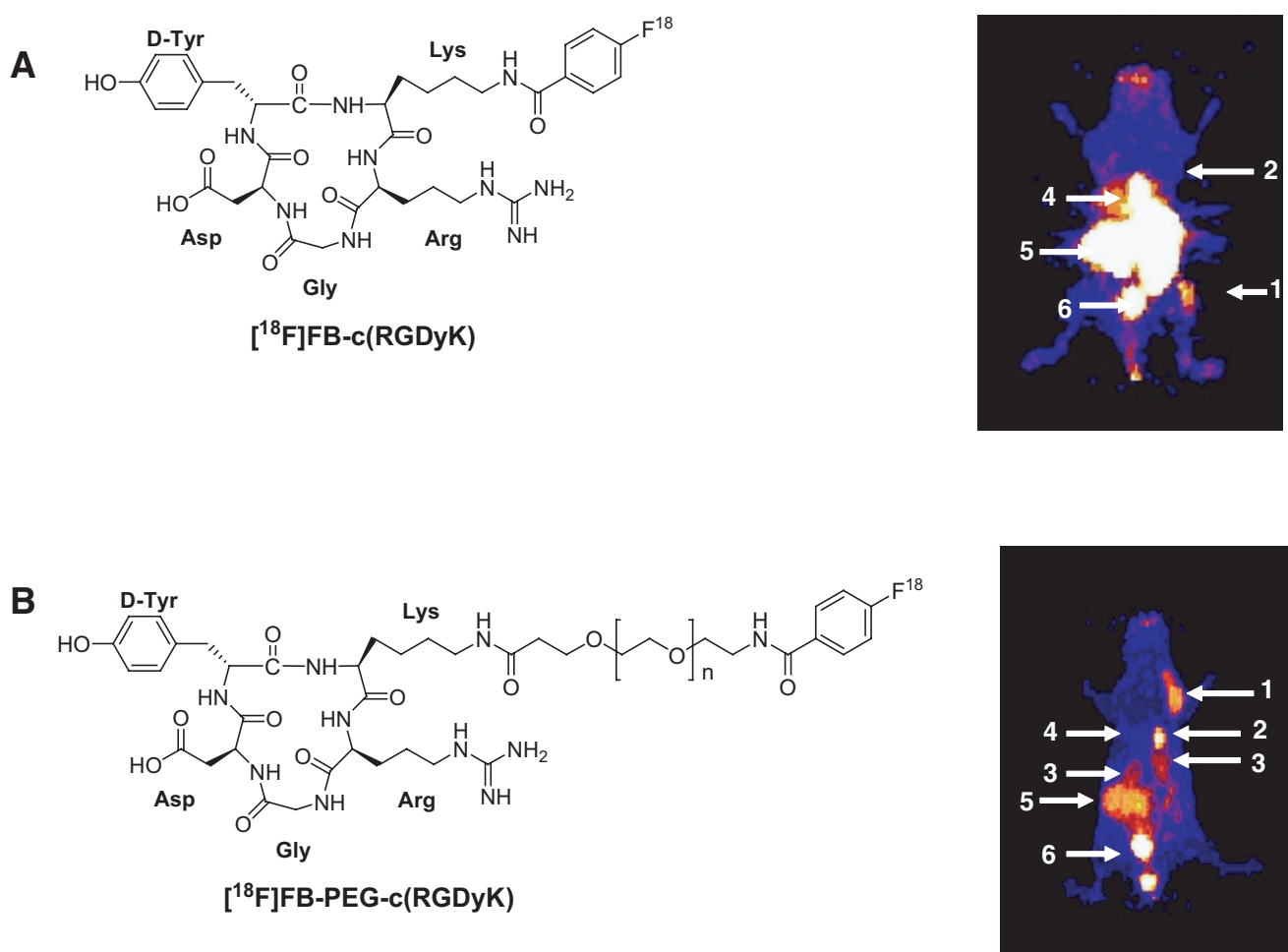


**Figure 5. PEGylation improves the *in vivo* kinetics of <sup>18</sup>F-labeled RGD peptides.** (A) Structure of [<sup>18</sup>F]FB-RGD and two-dimensional (2-D) projection microPET image of U87MG tumor-bearing mouse 60 min after injection of [<sup>18</sup>F]FB-RGD. (B) Structure of [<sup>18</sup>F]FB-PEG-RGD (PEG M.W. = 3400) and 2-D projection image of U87MG tumor-bearing mouse 60 min after injection of [<sup>18</sup>F]FB-PEG-RGD. 1, U87MG tumor; 2, gallbladder; 3, kidney; 4, liver; 5, intestines; 6, bladder; RGD, arginine-glycine-aspartic acid; PET, positron emission tomography.

at early time points, but more rapid clearance compared with  $^{64}\text{Cu}$ -DOTA-c(RGDyK) (84). Although PEGylation at the lysine side chain reduced the integrin binding affinity of the RGD peptide, the tumor activity accumulation was virtually unaltered. However, the suboptimal tumor uptake and retention of this PEGylated tracer limited its further application for receptor radionuclide therapy.

Dimeric RGD peptides were then labeled with  $^{64}\text{Cu}$ , and their tumor targeting efficacy in murine xenograft models was tested (Figure 7A) (28). At all time points, activity accumulation of  $^{64}\text{Cu}$ -DOTA-E[c(RGDyK)]<sub>2</sub> in tumors was significantly higher than that of the D-Phe analog. Liver uptake of  $^{64}\text{Cu}$ -DOTA-E[c(RGDyK)]<sub>2</sub> was lower than the D-Phe derivative  $^{64}\text{Cu}$ -DOTA-E[c(RGDfK)]<sub>2</sub> at early time points but the difference became marginal over time. Overall,  $^{64}\text{Cu}$ -DOTA-E[c(RGDyK)]<sub>2</sub> yielded better PET images in orthotopic MDA-MB-435 bearing mice than did  $^{64}\text{Cu}$ -DOTA-E[c(RGDfK)]<sub>2</sub>, most likely attributed to the increased hydrophilicity of D-Tyr over D-Phe. Both dimeric peptides showed better tumor retention than the previously tested monomeric RGD counterparts, presumably because of bivalency and the increase in apparent molecular size. In both cases, the tumor uptake can be efficiently blocked by injection of the unlabeled RGD peptide. PEGylated RGD dimer  $^{64}\text{Cu}$ -DOTA-

PEG-E[c(RGDyK)]<sub>2</sub> had similar blood clearance, more rapid renal clearance, and significantly reduced hepatic uptake as compared with  $^{64}\text{Cu}$ -DOTA-E[c(RGDyK)]<sub>2</sub> (75). Rapid tumor localization and high tumor-to-background contrast makes  $^{64}\text{Cu}$ -DOTA-PEG-E[c(RGDyK)]<sub>2</sub> a promising agent for integrin  $\alpha_v\beta_3$ -positive tumor imaging. One striking observation is that it accumulated specifically in both primary and metastatic lung tumor lesions (Figure 7B), while FDG only delineates the primary tumor but none of the metastatic sites because of high uptake of FDG in the heart area. However, the significance of this finding may be slightly diluted by the fact that the magnitude of tumor uptake is too low (<3% ID/g) for peptide receptor radiotherapy applications.

Janssen et al. first applied the polyvalency strategy for SPECT imaging using  $^{99m}\text{Tc}$  and  $^{111}\text{In}$ -labeled dimeric RGD peptides (56,58). Various reports have since demonstrated that the dimer gives better in vivo kinetics as well as much improved imaging results. Very recently, Wu et al. (64) developed a tetrameric RGD peptide tracer  $^{64}\text{Cu}$ -DOTA-E[c(RGDfK)]<sub>2</sub> (Figure 8A) for integrin  $\alpha_v\beta_3$  imaging in a subcutaneous U87MG glioma xenograft model. The RGD tetramer showed significantly higher integrin binding affinity than the corresponding mono- and dimeric RGD analogs. The radio-

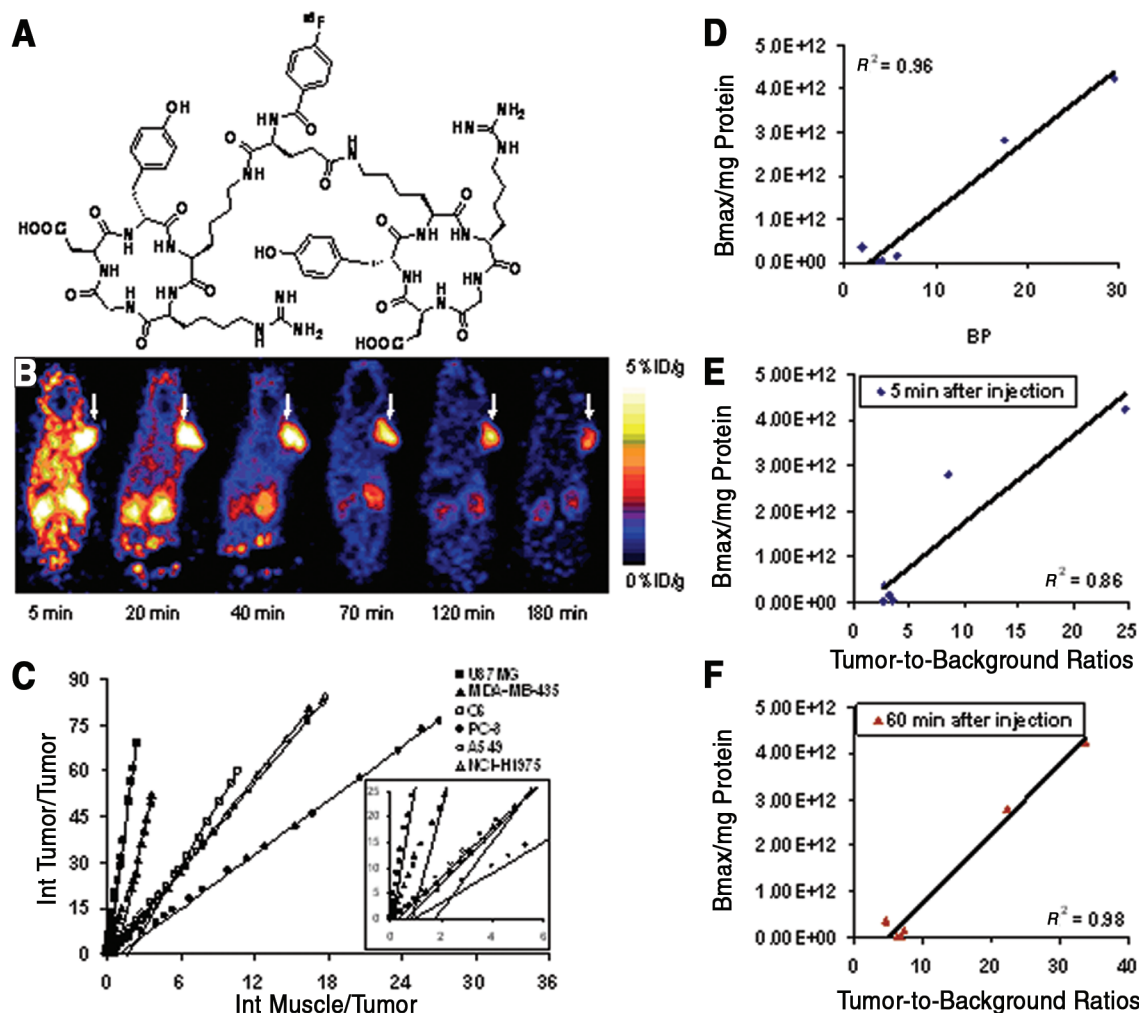


**Figure 6. Quantitative imaging of integrin  $\alpha_v\beta_3$  expression in vivo.** (A) Structure of  $[^{18}\text{F}]FB\text{-E}[c(\text{RGDyK})]_2$  (abbreviated as  $[^{18}\text{F}]FRGD2$ ). (B) Dynamic microPET study of U87MG tumor-bearing mouse over 60 min after injection of  $[^{18}\text{F}]FRGD2$ , static scans at 120 min and 180-min time points were also conducted to complete the tracer kinetic study. Decay-corrected whole-body coronal images containing the tumor are shown. (C) Logan plots derived from 60-min dynamic microPET imaging data showed excellent linearity of normalized integrated (Int) tumor activity versus normalized integrated muscle tissue activity effective for  $t > 25$  min. The curves for  $t < 25$  min are shown in the inset. (D) Correlation analysis between tumor tissue receptor density [Bmax/mg protein measured from sodium dodecyl sulfate polyacrylamide gel electrophoresis (SDS-PAGE)/autoradiography using  $^{125}\text{I}$ -echistatin as the radioligand] versus binding potential (BP; calculated from the Logan plot transformation of dynamic microPET imaging data). (E) Tumor tissue receptor density versus tumor-to-background ratio at 5 min postinjection (p.i.) of  $[^{18}\text{F}]FRGD2$ . (F) Tumor tissue receptor density versus tumor-to-background ratio at 60 min p.i. of  $[^{18}\text{F}]FRGD2$ . PET, positron emission tomography. Adapted from References 63 and 78.

labeled peptide showed rapid blood clearance, predominant renal excretion, significant receptor-mediated tumor uptake, and good contrast in tumor mice. Tumor uptake was rapid and high, and the tumor washout was slow ( $9.93 \pm 1.05\%$  ID/g at 30 min p.i. and  $4.56 \pm 0.51\%$  ID/g at 24 h p.i.) (Figure 8B). This tracer was metabolically stable. The high integrin avidity and favorable biokinetics make  $^{64}\text{Cu}$ -DOTA-E[E(c(RGDfK)]<sub>2</sub>] a promising agent for peptide receptor radionuclide imaging as well as radiotherapy of integrin-positive tumors.

## CONCLUSION AND FUTURE PERSPECTIVE

Significant advances have been achieved in developing novel probes for multimodality molecular imaging of tumor integrin expression. Small molecules, peptides, peptidomimetic integrin  $\alpha_v\beta_3$  antagonists, and antibodies have been labeled with radioisotopes, superparamagnetic nanoparticles, fluorescent dyes, QDs, and microbubbles for PET, SPECT, MRI, NIR fluorescence, and ultrasound imaging of small animals, mostly tumor models. The nanoparticles or microbubbles used for MRI or ultrasound imaging has relatively large particle sizes (usually >200 nm) and typically can not extravasate from the blood vessels. Therefore, they may only be suitable for tumor vasculature imaging rendering limited potential in the clinic due to less available targets as compared to the small molecule tracers that can extravasate and therefore target

not only the tumor vasculature but also the tumor cells. Because of the high sensitivity and adequate spatial and temporal resolution of PET, development of PET probes for integrin expression imaging is currently the most active among all these modalities.  $[^{18}\text{F}]$ Galacto-RGD is already in clinical trials for cancer imaging.  $[^{18}\text{F}]$ -labeled RGD dimer  $[^{18}\text{F}]$ FRGD2 may outperform  $[^{18}\text{F}]$ Galacto-RGD because of its higher receptor avidity and more favorable pharmacokinetics as well as the ability to quantify integrin expression *in vivo*.  $^{64}\text{Cu}$ -labeled tetramer exhibited high and prolonged tumor retention and rapid liver and kidney clearance resulting in good tumor-to-normal organ ratios, which not only makes this tracer suitable for early lesion detection but also for integrin-targeted radiotherapy. RGD peptides may also be labeled with less common PET isotopes such as  $^{124}\text{I}$  and  $^{86}\text{Y}$ , which can help guide  $^{131}\text{I}$  and  $^{90}\text{Y}$ -RGD therapy, respectively. Radiolabeled antibodies against integrin  $\alpha_v\beta_3$  have not been well studied despite the fact that a humanized monoclonal antibody Vitaxin® is already in phase II clinical trials for treatment of melanoma and prostate cancer patients (85,86). Development of suitably labeled Vitaxin for imaging the pharmacokinetics and pharmacodynamic of the systemically administered antibody or for integrin-targeted radioimmunotherapy may need to be emphasized for future studies.

Despite the fact that  $[^{18}\text{F}]$ galacto-RGD is already in early clinical trials for documentation of integrin expression in cancer patients, many other relevant integrin  $\alpha_v\beta_3$ -specific imaging probes discussed in this review suffer from the slow translation from bench to bedside. Multiple steps in preclinical development, such as pharmacokinetics, dosimetry, imaging feasibility, and investigational new drug (IND)-directed toxicology, are necessary to convert a potential new agent into a diagnostic drug candidate suitable for early clinical testing. Emphasis on highly specific molecular targets and processes has led to products with increased complexity and higher costs of development but smaller market potential. This trend has effectively created a class of agents that investors consider too risky for commercial development, but these agents may have the potential to influence diagnosis and treatment significantly. A general strategy of angiogenesis imaging may thus be more practical in the long run than very specific protein targets (e.g., Her-2/Neu).

Tumor integrin expression imaging has potential clinical applications in many aspects. The first aspect is lesion detection. Despite the clinical success with  $[^{18}\text{F}]$ FDG/PET imaging, this tracer has several limitations. The tracer can be nonspecifically taken up by several benign conditions such as inflammatory disease, pneumonia, brown fat, muscle, bowel uptake, and granulomatous disease. Also, slow growing indolent tumors may exhibit only a mild increase in glucose metabolism and therefore can be missed by FDG PET (1,87). As most tumor vasculature endothelial cells and many tumor cells express integrin  $\alpha_v\beta_3$ , suitably labeled RGD peptides might be a potentially more advantageous surrogate marker than FDG for more sensitive detection or detecting lower tumor burden. The second aspect is patient stratification. Differences in tracer accumulation in various tumor types suggest a great diversity in integrin receptor expression. In light of the differences in receptor expression and tracer accumulation, quantitative imaging of tumor integrin becomes very important as a mechanism to stratify and select patients to enter clinical trials focused on anti-integrin treatment. The third aspect is new drug development and/or validation. Rapid characterization of pharmacokinetics and pharmacodynamics by multimodality *in vivo* imaging of new tracers or anti-integrin drugs can improve

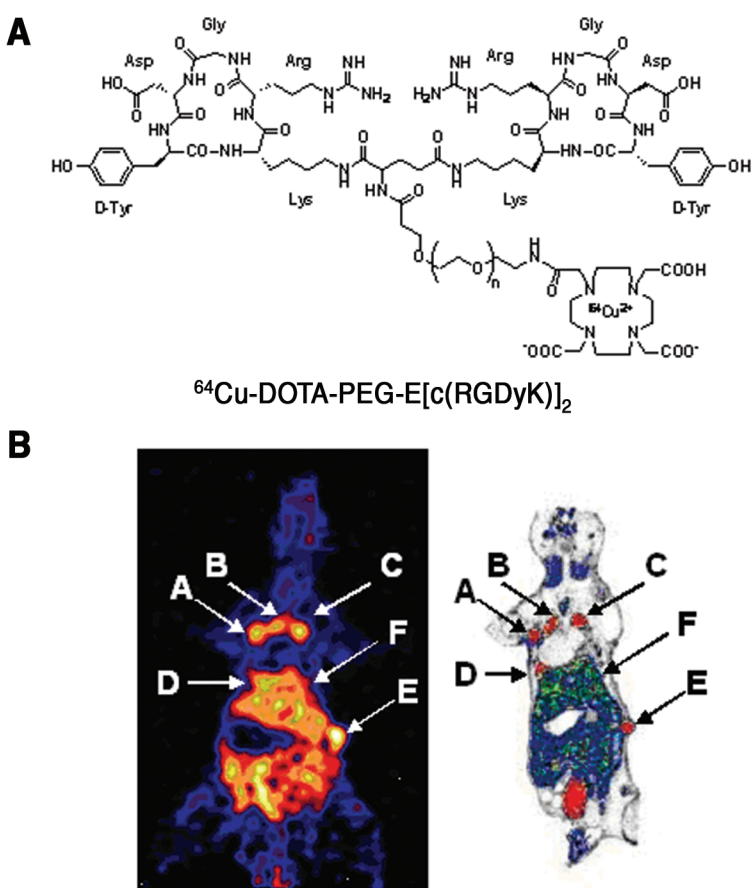


**Figure 7.**  $^{64}\text{Cu}$ -labeled tracer for integrin  $\alpha_v\beta_3$  expression imaging. (A) The structure of  $^{64}\text{Cu}$ -DOTA-PEG-E[c(RGDyK)]<sub>2</sub>. (B, left panel) coronal image (15-min static scan) of severe combined immunodeficiency (SCID)-bg mouse bearing both subcutaneous and orthotopic NCI-H1975 tumors at 2 h after injection of  $^{64}\text{Cu}$ -DOTA-PEG-E[c(RGDyK)]<sub>2</sub>. Both primary tumors and metastases are clearly identified. (B, right panel) Whole body digital autoradiograph of a 50- $\mu\text{m}$ -thick section correlating well with the coronal microPET image shown on the left. (B, panel labels) A, primary orthotopic tumor in the upper lobe of the left lung; B, local metastasis of the primary tumor; C, contralateral lung metastasis; D, metastasis in the diaphragm; E, subcutaneous tumor; F, liver. PET, positron emission tomography. Adapted from Reference 75.

data quality, reduce costs, reduce number of animals used, and most importantly, decrease the work-up for new compounds. Fourth is treatment monitoring and optimization. Visualization and quantification of tumor integrin levels by noninvasive molecular imaging can be applied to detect early response to anti-integrin treatment and to elucidate the mechanisms of treatment efficacy underlying integrin signaling, therefore providing important information for treatment optimization. Finally, the fifth aspect is the combination of molecular and functional imaging. As the molecular imaging probes get more specific regarding which leads to a visible signal in only the tumor or other targeted tissue, anatomical and/or functional imaging techniques are needed to identify the exact location of the signal. The combination of molecular and anatomical and/or functional imaging techniques in assessing tumor angiogenesis and in response to antiangiogenic-based therapy will be a powerful tool, and the new generation clinical PET-CT and microPET/microCT will likely play a major role in cancer imaging for the years to come.

Tumor integrin  $\alpha_v\beta_3$  expression imaging is given as an example here to demonstrate how molecular imaging can provide a robust platform for understanding the mechanisms of tumor angiogenesis and evaluating the efficacy of novel antiangiogenic therapies. Further progress is needed to improve the sensitivity and resolution of molecular imaging technologies and to develop optimal molecular imaging probes as surrogate markers to pinpoint and monitor specific molecular and cellular actions of angiogenesis inhibitors.

Development of multimodality probes, for example, probes that can give both PET and MRI signals, will be of significant value but are currently unexplored. Other targets besides integrins, such as VEGFR, MMP-2, etc., are also being studied for multimodality *in vivo* imaging of tumor angiogenesis.

#### ACKNOWLEDGMENTS

We apologize to authors whose works were not cited in this review due to space limitations. This work was supported, in part, by National Cancer Institute (NCI) grant R21 CA102123, National Institute of Biomedical Imaging and Bioengineering (NIBIB) grant R21 EB001785, Department of Defense (DOD) Breast Cancer Research Program (BCRP) Concept Award DAMD17-03-1-0752, DOD BCRP IDEA Award W81XWH-04-1-0697, DOD Ovarian Cancer Research Program (OCRP) Award OC050120, DOD Prostate Cancer Research Program (PCRP) New Investigator Award (NIA) DAMD1717-03-1-0143, American Lung Association California (ALAC), the Society of Nuclear Medicine Education and Research Foundation, National Cancer Institute (NCI) Small Animal Imaging Resource Program (SAIRP) grant R24 CA93862, and NCI In Vivo Cellular Molecular Imaging Center (ICMIC) grant P50 CA114747. The production of Cu-64 at Washington University School of Medicine is supported by the NCI grant R24 CA86307.

#### COMPETING INTERESTS STATEMENT

The authors declare no competing interests.

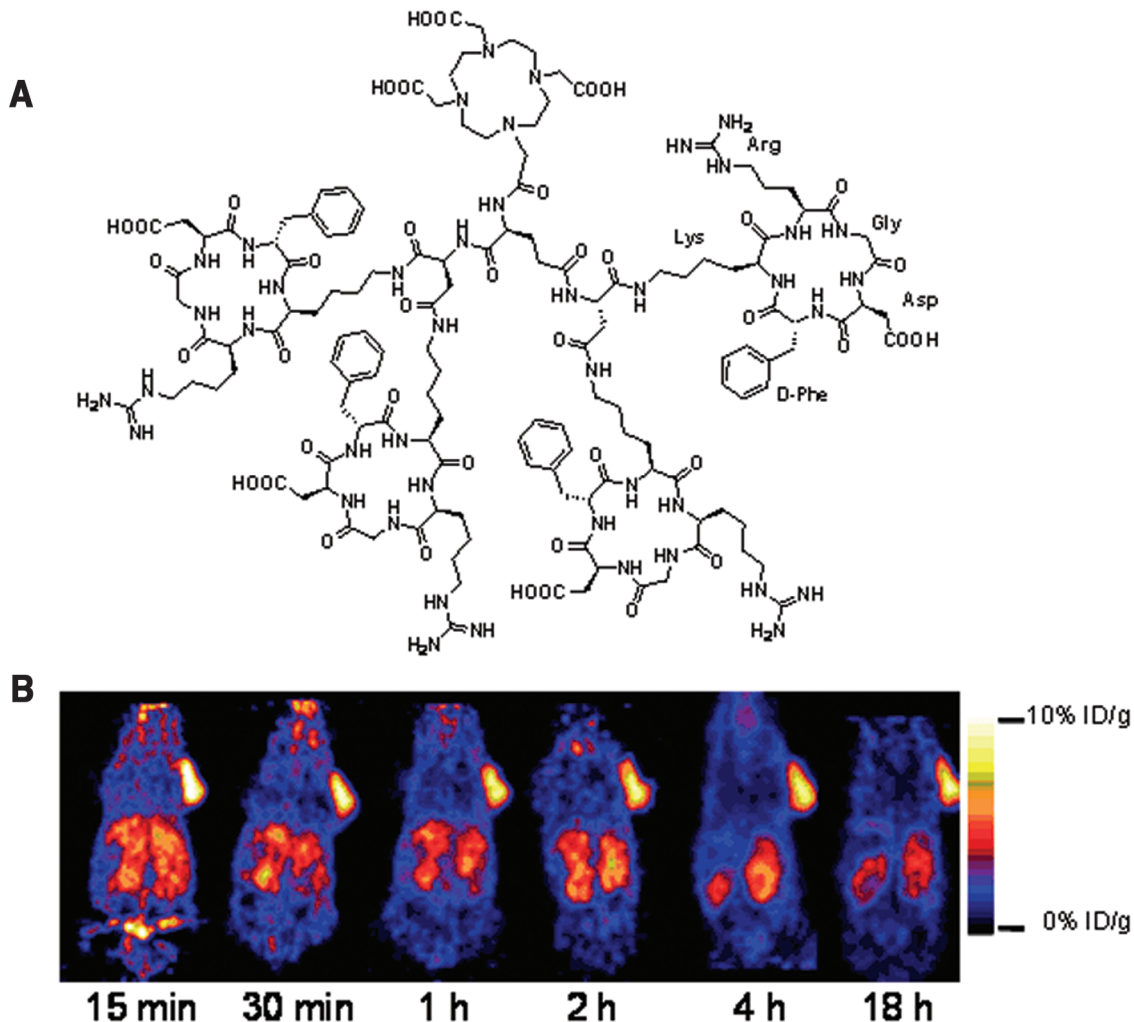


**Figure 8.** <sup>64</sup>Cu-labeled tetrameric RGD-based tracer for integrin expression imaging. (A) Structure of DOTA-E[E(c(RGDfK)]<sub>2</sub>]<sub>2</sub>. (B) Decay-corrected whole-body coronal microPET images of a nude mouse bearing human U87MG tumor at various time points (10-min static image) after injection of <sup>64</sup>Cu-DOTA-E[E(c(RGDfK)]<sub>2</sub>]<sub>2</sub>. PET, positron emission tomography. Adapted from Reference 64.

## REFERENCES

1. Gambhir, S.S. 2002. Molecular imaging of cancer with positron emission tomography. *Nat. Rev. Cancer* 2:683-693.
2. Massoud, T.F. and S.S. Gambhir. 2003. Molecular imaging in living subjects: seeing fundamental biological processes in a new light. *Genes Dev.* 17:545-580.
3. Herschman, H.R. 2003. Molecular imaging: looking at problems, seeing solutions. *Science* 302:605-608.
4. Gross, S. and D. Piwnica-Worms. 2005. Spying on cancer: molecular imaging in vivo with genetically encoded reporters. *Cancer Cell* 7:5-15.
5. Weissleder, R. and U. Mahmood. 2001. Molecular imaging. *Radiology* 219:316-333.
6. Bergers, G. and L.E. Benjamin. 2003. Tumorigenesis and the angiogenic switch. *Nat. Rev. Cancer* 3:401-410.
7. Ferrara, N. 2002. VEGF and the quest for tumour angiogenesis factors. *Nat. Rev. Cancer* 2:795-803.
8. Nyberg, P., L. Xie, and R. Kalluri. 2005. Endogenous inhibitors of angiogenesis. *Cancer Res.* 65:3967-3979.
9. Kerbel, R. and J. Folkman. 2002. Clinical translation of angiogenesis inhibitors. *Nat. Rev. Cancer* 2:727-739.
10. Tucker, G.C. 2003.  $\alpha_1$  integrin inhibitors and cancer therapy. *Curr. Opin. Investig. Drugs* 4:722-731.
11. Jain, R.K. 2005. Normalization of tumor vasculature: an emerging concept in antiangiogenic therapy. *Science* 307:58-62.
12. Hanahan, D. and J. Folkman. 1996. Patterns and emerging mechanisms of the angiogenic switch during tumorigenesis. *Cell* 86:353-364.
13. Friedl, P. and K. Wolf. 2003. Tumour-cell invasion and migration: diversity and escape mechanisms. *Nat. Rev. Cancer* 3:362-374.
14. Sahai, E. 2005. Mechanisms of cancer cell invasion. *Curr. Opin. Genet. Dev.* 15:87-96.
15. Egeblad, M. and Z. Werb. 2002. New functions for the matrix metalloproteinases in cancer progression. *Nat. Rev. Cancer* 2:161-174.
16. Bogenrieder, T. and M. Herlyn. 2003. Axis of evil: molecular mechanisms of cancer metastasis. *Oncogene* 22:6524-6536.
17. Ruoslahti, E. 1996. RGD and other recognition sequences for integrins. *Annu. Rev. Cell Dev. Biol.* 12:697-715.
18. Xiong, J.P., T. Stehle, B. Diefenbach, R. Zhang, R. Dunker, D.L. Scott, A. Joachimiak, S.L. Goodman, and M.A. Arnaut. 2001. Crystal structure of the extracellular segment of integrin  $\alpha_1\beta_3$ . *Science* 294:339-345.
19. Brooks, P.C., R.A. Clark, and D.A. Cheresh. 1994. Requirement of vascular integrin  $\alpha_1\beta_3$  for angiogenesis. *Science* 264:569-571.
20. Kumar, C.C. 2003. Integrin  $\alpha_1\beta_3$  as a therapeutic target for blocking tumor-induced angiogenesis. *Curr. Drug Targets* 4:123-131.
21. Hood, J.D. and D.A. Cheresh. 2002. Role of integrins in cell invasion and migration. *Nat. Rev. Cancer* 2:91-100.
22. Xiong, J.P., T. Stehle, R. Zhang, A. Joachimiak, M. Frech, S.L. Goodman, M.A. Arnaut, B. Diefenbach, et al. 2002. Crystal structure of the extracellular segment of integrin  $\alpha_1\beta_3$  in complex with an Arg-Gly-Asp ligand. *Science* 296:151-155.
23. Jin, H. and J. Varner. 2004. Integrins: roles in cancer development and as treatment targets. *Br. J. Cancer* 90:561-565.
24. Brooks, P.C., S. Stromblad, L.C. Sanders, T.L. von Schalscha, R.T. Aimes, W.G. Stetler-Stevenson, J.P. Quigley, and D.A. Cheresh. 1996. Localization of matrix metalloproteinase MMP-2 to the surface of invasive cells by interaction with integrin  $\alpha_1\beta_3$ . *Cell* 85:683-693.
25. Schmieder, A.H., P.M. Winter, S.D. Caruthers, T.D. Harris, T.A. Williams, J.S. Allen, E.K. Lacy, H. Zhang, et al. 2005. Molecular MR imaging of melanoma angiogenesis with  $\alpha_1\beta_3$ -targeted paramagnetic nanoparticles. *Magn. Reson. Med.* 53:621-627.
26. Chen, X., R. Park, Y. Hou, V. Khankaldyyan, I. Gonzales-Gomez, M. Tohme, J.R. Bading, W.E. Laug, and P.S. Conti. 2004. MicroPET imaging of brain tumor angiogenesis with  $^{18}\text{F}$ -labeled PEGylated RGD peptide. *Eur. J. Nucl. Med. Mol. Imaging* 31:1081-1089.
27. Beck, V., H. Herold, A. Benge, B. Luber, P. Hutzler, H. Tschesche, H. Kessler, M. Schmitt, et al. 2005. ADAM15 decreases integrin  $\alpha_1\beta_3$ /vitronectin-mediated ovarian cancer cell adhesion and motility in an RGD-dependent fashion. *Int. J. Biochem. Cell Biol.* 37:590-603.
28. Chen, X., S. Liu, Y. Hou, M. Tohme, R. Park, J.R. Bading, and P.S. Conti. 2004. MicroPET imaging of breast cancer  $\alpha_1$ -integrin expression with  $^{64}\text{Cu}$ -labeled dimeric RGD peptides. *Mol. Imaging Biol.* 6:350-359.
29. Chen, X., R. Park, M. Tohme, A.H. Shahinian, J.R. Bading, and P.S. Conti. 2004. Micro-PET and autoradiographic imaging of breast cancer  $\alpha_1$ -integrin expression using  $^{18}\text{F}$ - and  $^{64}\text{Cu}$ -labeled RGD peptide. *Bioconjug. Chem.* 15:41-49.
30. Meerovitch, K., F. Bergeron, L. Leblond, B. Groulx, C. Poirier, M. Bubenik, L. Chan, H. Gourdeau, et al. 2003. A novel RGD antagonist that targets both  $\alpha_1\beta_3$  and  $\alpha_5\beta_1$  induces apoptosis of angiogenic endothelial cells on type I collagen. *Vascul. Pharmacol.* 40:77-89.
31. Qiao, R., W. Yan, H. Lum, and A.B. Malik. 1995. Arg-Gly-Asp peptide increases endothelial hydraulic conductivity: comparison with thrombin response. *Am. J. Physiol.* 269:C110-117.
32. Haubner, R.H., H.J. Wester, W.A. Weber, and M. Schwaiger. 2003. Radiotracer-based strategies to image angiogenesis. *Q. J. Nucl. Med.* 47:189-199.
33. Haubner, R. and H.J. Wester. 2004. Radiolabeled tracers for imaging of tumor angiogenesis and evaluation of anti-angiogenic therapies. *Curr. Pharm. Des.* 10:1439-1455.
34. Pathak, A.P., B. Gimel, K. Glunde, E. Ackerstaff, D. Artemov, and Z.M. Bhujwalla. 2004. Molecular and functional imaging of cancer: advances in MRI and MRS. *Methods Enzymol.* 386:3-60.
35. Sipkins, D.A., D.A. Cheresh, M.R. Kazemi, L.M. Nevin, M.D. Bednarski, and K.C. Li. 1998. Detection of tumor angiogenesis in vivo by  $\alpha_1\beta_3$ -targeted magnetic resonance imaging. *Nat. Med.* 4:623-626.
36. Anderson, S.A., R.K. Rader, W.F. Westlin, C. Null, D. Jackson, G.M. Lanza, S.A. Wickline, and J.J. Kotyk. 2000. Magnetic resonance contrast enhancement of neovasculature with  $\alpha_1\beta_3$ -targeted nanoparticles. *Magn. Reson. Med.* 44:433-439.
37. Winter, P.M., S.D. Caruthers, A. Kassner, T.D. Harris, L.K. Chinen, J.S. Allen, E.K. Lacy, H. Zhang, et al. 2003. Molecular imaging of angiogenesis in nascent Vx-2 rabbit tumors using a novel  $\alpha_1\beta_3$ -targeted nanoparticle and 1.5 tesla magnetic resonance imaging. *Cancer Res.* 63:5838-5843.
38. Winter, P.M., A.M. Morawski, S.D. Caruthers, R.W. Fuhrhop, H. Zhang, T.A. Williams, J.S. Allen, E.K. Lacy, et al. 2003. Molecular imaging of angiogenesis in early-stage atherosclerosis with  $\alpha_1\beta_3$ -integrin-targeted nanoparticles. *Circulation* 108:2270-2274.
39. Morawski, A.M., G.A. Lanza, and S.A. Wickline. 2005. Targeted contrast agents for magnetic resonance imaging and ultrasound. *Curr. Opin. Biotechnol.* 16:89-92.
40. Ellegala, D.B., H. Leong-Poi, J.E. Carpenter, A.L. Klibanov, S. Kaul, M.E. Shaffrey, J. Sklenar, and J.R. Lindner. 2003. Imaging tumor angiogenesis with contrast ultrasound and microbubbles targeted to  $\alpha_1\beta_3$ . *Circulation* 108:336-341.
41. Leong-Poi, H., J. Christiansen, A.L. Klibanov, S. Kaul, and J.R. Lindner. 2003. Noninvasive assessment of angiogenesis by ultrasound and microbubbles targeted to  $\alpha_1$ -integrins. *Circulation* 107:455-460.
42. Leong-Poi, H., J. Christiansen, P. Heppner, C.W. Lewis, A.L. Klibanov, S. Kaul, and J.R. Lindner. 2005. Assessment of endogenous and therapeutic arteriogenesis by contrast ultrasound molecular imaging of integrin expression. *Circulation* 111:3248-3254.
43. Shohet, R.V., S. Chen, Y.T. Zhou, Z. Wang, R.S. Meidell, R.H. Unger, and P.A. Grayburn. 2000. Echocardiographic destruction of albumin microbubbles directs gene delivery to the myocardium. *Circulation* 101:2554-2556.
44. Frangioni, J.V. 2003. In vivo near-infrared fluorescence imaging. *Curr. Opin. Chem. Biol.* 7:626-634.
45. Spibey, C.A., P. Jackson, and K. Herick. 2001. A unique charge-coupled device/xenon arc lamp based imaging system for the accurate detection and quantitation of multicolour fluorescence. *Electrophoresis* 22:829-836.
46. Montet, X., V. Ntziachristos, J. Grimm, and R. Weissleder. 2005. Tomographic fluorescence mapping of tumor targets. *Cancer Res.* 65:6330-6336.
47. Chen, X., P.S. Conti, and R.A. Moats. 2004. In vivo near-infrared fluorescence imaging of integrin  $\alpha_1\beta_3$  in brain tumor xenografts. *Cancer Res.* 64:8009-8014.
48. Wang, W., S. Ke, Q. Wu, C. Charansangavej, M. Gurfinkel, J.G. Gelovani, J.L. Abbruzzese, E.M. Sevick-Muraca, and C. Li. 2004. Near-infrared optical imaging of integrin  $\alpha_1\beta_3$  in human tumor xenografts. *Mol. Imaging* 3:343-351.
49. Sunkuk, K., K. Shi, J.P. Houston, W. Wei, W. Qingping, L. Chun, and E.M. Sevick-Muraca. 2005. Imaging dose-dependent pharmacokinetics of an RGD-fluorescent dye conjugate targeted to  $\alpha_1\beta_3$  receptor expressed in Kaposi's sarcoma. *Mol. Imaging* 4:75-87.
50. Burnett, C.A., J. Xie, J. Quijano, Z. Shen, F. Hunter, M. Bur, K.C. Li, and S.N. Danthi. 2005. Synthesis, in vitro, and in vivo characterization of an integrin  $\alpha_1\beta_3$ -targeted molecular probe for optical imaging of tumor. *Bioorg. Med. Chem.* 13:3763-3771.
51. Achilefu, S., S. Bloch, M.A. Markiewicz, T. Zhong, Y. Ye, R.B. Dorshow, B. Chance, and K. Liang. 2005. Synergistic effects of light-emitting probes and peptides for targeting and monitoring integrin expression. *Proc. Natl. Acad. Sci. USA* 102:7976-7981.
52. Michalet, X., F.F. Pinaud, L.A. Bentolila, J.M. Tsay, S. Doose, J.J. Li, G. Sundaresan, A.M. Wu, et al. 2005. Quantum dots for live cells, in vivo imaging, and diagnostics. *Science* 307:538-544.
53. Cai, W., D. Shin, Y. Wu, O. Gheysens, Q. Cao, S.S. Gambhir, S.X. Wang, and X. Chen. 2005. RGD peptide-labeled NIR quantum dot for in vivo cancer imaging. *Nat. Biotechnol.* (Submitted).
54. Rolland, A., B. Collet, R. Le Verge, and L. Toujas. 1989. Blood clearance and organ distribution of intravenously administered polymethacrylic nanoparticles in mice. *J. Pharm. Sci.* 78:481-484.
55. Peremans, K., B. Cornelissen, B. Van Den Bossche, K. Audenaert, and C. Van de Wiele. 2005. A review of small animal imaging planar and pinhole spect Gamma camera imaging. *Vet. Radiol. Ultrasound* 46:162-170.
56. Janssen, M.L., W.J. Oyen, I. Dijkgraaf, L.F. Massuger, C. Frieling, D.S. Edwards, M. Rajopadhye, H. Boonstra, et al. 2002. Tumor targeting with radiolabeled  $\alpha_1\beta_3$  integrin binding peptides in a nude mouse model. *Cancer Res.* 62:6146-6151.

57. Janssen, M., C. Frielink, I. Dijkgraaf, W. Oyen, D.S. Edwards, S. Liu, M. Rajopadhye, L. Massuger, et al. 2004. Improved tumor targeting of radiolabeled RGD peptides using rapid dose fractionation. *Cancer Biother. Radiopharm.* 19:399-404.
58. Janssen, M., W.J. Oyen, L.F. Massuger, C. Frielink, I. Dijkgraaf, D.S. Edwards, M. Rajopadhye, F.H. Corstens, and O.C. Boerman. 2002. Comparison of a monomeric and dimeric radiolabeled RGD-peptide for tumor targeting. *Cancer Biother. Radiopharm.* 17:641-646.
59. Sadeghi, M.M., S. Krassilnikova, J. Zhang, A.A. Gharaei, H.R. Fassaei, L. Esmailzadeh, A. Kooshkabadi, S. Edwards, et al. 2004. Detection of injury-induced vascular remodeling by targeting activated  $\alpha_v\beta_3$  integrin in vivo. *Circulation* 110:84-90.
60. Meoli, D.F., M.M. Sadeghi, S. Krassilnikova, B.N. Bourke, F.J. Giordano, D.P. Dione, H. Su, D.S. Edwards, et al. 2004. Noninvasive imaging of myocardial angiogenesis following experimental myocardial infarction. *J. Clin. Invest.* 113:1684-1691.
61. Haubner, R., H.J. Wester, U. Reuning, R. Senekowitsch-Schmidtke, B. Diefenbach, H. Kessler, G. Stocklin, and M. Schwaiger. 1999. Radiolabeled  $\alpha_v\beta_3$  integrin antagonists: a new class of tracers for tumor targeting. *J. Nucl. Med.* 40:1061-1071.
62. Haubner, R., W.A. Weber, A.J. Beer, E. Vabuliene, D. Reim, M. Sarbia, K.F. Becker, M. Goebel, et al. 2005. Noninvasive visualization of the activated  $\alpha_v\beta_3$  integrin in cancer patients by positron emission tomography and [ $^{18}\text{F}$ ]galacto-RGD. *PLoS Med.* 2:e70.
63. Chen, X., M. Tohme, R. Park, Y. Hou, J.R. Bading, and P.S. Conti. 2004. Micro-PET imaging of  $\alpha_v\beta_3$ -integrin expression with [ $^{18}\text{F}$ ]-labeled dimeric RGD peptide. *Mol. Imaging* 3:96-104.
64. Wu, Y., X. Zhang, Z. Xiong, Z. Cheng, D.R. Fisher, S. Liu, and X. Chen. 2005. MicroPET imaging of glioma  $\alpha_v$ -integrin expression using [ $^{64}\text{Cu}$ ]-labeled tetrameric RGD peptide. *J. Nucl. Med.* 46:1707-1718.
65. Sharma, V., G.D. Luker, and D. Piwnica-Worms. 2002. Molecular imaging of gene expression and protein function in vivo with PET and SPECT. *J. Magn. Reson. Imaging* 16:336-351.
66. Haubner, R., H.J. Wester, F. Burkhart, R. Senekowitsch-Schmidtke, W. Weber, S.L. Goodman, H. Kessler, and M. Schwaiger. 2001. Glycosylated RGD-containing peptides: tracer for tumor targeting and angiogenesis imaging with improved biokinetics. *J. Nucl. Med.* 42:326-336.
67. Haubner, R., H.-J. Wester, W.A. Weber, C. Mang, S.I. Ziegler, S.L. Goodman, R. Senekowitsch-Schmidtke, H. Kessler, and M. Schwaiger. 2001. Noninvasive imaging of  $\alpha_v\beta_3$  integrin expression using [ $^{18}\text{F}$ ]-labeled RGD-containing glycopeptide and positron emission tomography. *Cancer Res.* 61:1781-1785.
68. Haubner, R., B. Kuhnast, C. Mang, W.A. Weber, H. Kessler, H.J. Wester, and M. Schwaiger. 2004. [ $^{18}\text{F}$ ]Galacto-RGD: synthesis, radiolabeling, metabolic stability, and radiation dose estimates. *Bioconjug. Chem.* 15:61-69.
69. Beer, A.J., R. Haubner, M. Goebel, S. Luderschmidt, M.E. Spilker, H.J. Wester, W.A. Weber, and M. Schwaiger. 2005. Biodistribution and pharmacokinetics of the  $\alpha_v\beta_3$ -selective tracer [ $^{18}\text{F}$ ]-galacto-RGD in cancer patients. *J. Nucl. Med.* 46:1333-1341.
70. Sutcliffe-Goulden, J.L., M.J. O'Doherty, P.K. Marsden, I.R. Hart, J.F. Marshall, and S.S. Bansal. 2002. Rapid solid phase synthesis and biodistribution of [ $^{18}\text{F}$ ]-labelled linear peptides. *Eur. J. Nucl. Med. Mol. Imaging* 29:754-759.
71. Ogawa, M., K. Hatano, S. Oishi, Y. Kawasumi, N. Fujii, M. Kawaguchi, R. Doi, M. Imamura, et al. 2003. Direct electrophilic radiofluorination of a cyclic RGD peptide for in vivo  $\alpha_v\beta_3$  integrin related tumor imaging. *Nucl. Med. Biol.* 30:1-9.
72. Chen, X., R. Park, A.H. Shahinian, M. Tohme, V. Khankaldyan, M.H. Bozorgzadeh, J.R. Bading, R.A. Moats, et al. 2004.  $^{18}\text{F}$ -labeled RGD peptide: initial evaluation for imaging brain tumor angiogenesis. *Nucl. Med. Biol.* 31:179-189.
73. Chen, X., R. Park, A.H. Shahinian, J.R. Bading, and P.S. Conti. 2004. Pharmacokinetics and tumor retention of [ $^{125}\text{I}$ ]-labeled RGD peptide are improved by PEGylation. *Nucl. Med. Biol.* 31:11-19.
74. Gottschalk, K.E. and H. Kessler. 2002. The structures of integrins and integrin-ligand complexes: implications for drug design and signal transduction. *Angew. Chem. Int. Ed. Engl.* 41:3767-3774.
75. Chen, X., E. Sievers, Y. Hou, R. Park, M. Tohme, R. Bart, R. Bremner, J.R. Bading, and P.S. Conti. 2005. Integrin  $\alpha_v\beta_3$ -targeted imaging of lung cancer. *Neoplasia* 7:271-279.
76. Chen, X., C. Plasencia, Y. Hou, and N. Neamati. 2005. Synthesis and biological evaluation of dimeric RGD peptide-paclitaxel conjugate as a model for integrin-targeted drug delivery. *J. Med. Chem.* 48:1098-1106.
77. Mammen, M., S. Chio, and G.M. Whitesides. 1998. Polyvalent interactions in biological systems: implications for design and use of multivalent ligands and inhibitors. *Angew. Chem. Int. Ed. Engl.* 37:2755-2794.
78. Zhang, X., Z. Xiong, X. Wu, W. Cai, J.R. Tseng, S.S. Gambhir, and X. Chen. 2005. Quantitative PET imaging of tumor integrin  $\alpha_v\beta_3$  expression with [ $^{18}\text{F}$ ]FRGD2. *J. Nucl. Med.* (In press).
79. Logan, J. 2000. Graphical analysis of PET data applied to reversible and irreversible tracers. *Nucl. Med. Biol.* 27:661-670.
80. Kawatsu, S., T. Kato, A. Nagano-Saito, K. Hatano, K. Ito, and T. Ishigaki. 2003. New insight into the analysis of 6-[ $^{18}\text{F}$ ]fluoro-L-DOPA PET dynamic data in brain tissue without an irreversible compartment: comparative study of the Patlak and Logan analyses. *Radiat. Med.* 21:47-54.
81. Thibault, G. 2000. Sodium dodecyl sulfate-stable complexes of echistatin and RGD-dependent integrins: a novel approach to study integrins. *Mol. Pharmacol.* 58:1137-1145.
82. Anderson, C.J., L.A. Jones, L.A. Bass, E.L. Sherman, D.W. McCarthy, P.D. Cutler, M.V. Lanahan, M.E. Cristel, et al. 1998. Radiotherapy, toxicity and dosimetry of copper-64-TETA-octreotide in tumor-bearing rats. *J. Nucl. Med.* 39:1944-1951.
83. Pauwels, S., R. Barone, S. Walrand, F. Borson-Chazot, R. Valkema, L.K. Kvols, E.P. Krenning, and F. Jamar. 2005. Practical dosimetry of peptide receptor radionuclide therapy with [ $^{90}\text{Y}$ ]-labeled somatostatin analogs. *J. Nucl. Med.* 46(Suppl 1):92S-98S.
84. Chen, X., Y. Hou, M. Tohme, R. Park, V. Khankaldyan, I. Gonzales-Gomez, J.R. Bading, W.E. Laug, and P.S. Conti. 2004. Pegylated Arg-Gly-Asp peptide: [ $^{64}\text{Cu}$ ] labeling and PET imaging of brain tumor  $\alpha_v\beta_3$ -integrin expression. *J. Nucl. Med.* 45:1776-1783.
85. Posey, J.A., M.B. Khazaeli, A. DelGrosso, M.N. Saleh, C.Y. Lin, W. Huse, and A.F. LoBuglio. 2001. A pilot trial of Vitaxin, a humanized anti-vitronectin receptor (anti  $\alpha_v\beta_3$ ) antibody in patients with metastatic cancer. *Cancer Biother. Radiopharm.* 16:125-132.
86. Patel, S.R., J. Jenkins, N. Papadopolous, M.A. Burgess, C. Plager, J. Guterman, and R.S. Benjamin. 2001. Pilot study of vitaxin-an angiogenesis inhibitor-in patients with advanced leiomyosarcomas. *Cancer* 92:1347-1348.
87. Gambhir, S.S., J. Czernin, J. Schwimmer, D.H. Silverman, R.E. Coleman, and M.E. Phelps. 2001. A tabulated summary of the FDG PET literature. *J. Nucl. Med.* 42:1S-93S.

#### Address correspondence to:

Xiaoyuan Chen  
*Molecular Imaging Program at Stanford (MIPS)*  
*Department of Radiology and Bio-X Program*  
*Stanford University School of Medicine*  
*1201 Welch Road, Rm. P095*  
*Stanford, CA 94305-5484, USA*  
*e-mail: shawchen@stanford.edu*

# Quantitative PET Imaging of Tumor Integrin $\alpha_v\beta_3$ Expression with $^{18}\text{F}$ -FRGD2

Xianzhong Zhang, PhD; Zhengming Xiong, MD, PhD; Yun Wu, PhD; Weibo Cai, PhD; Jeffery R. Tseng, MD; Sanjiv S. Gambhir, MD, PhD; and Xiaoyuan Chen, PhD

Molecular Imaging Program at Stanford (MIPS), and Bio-X Program, Department of Radiology, Stanford University, Stanford, California

The development of noninvasive methods to visualize and quantify integrin  $\alpha_v\beta_3$  expression in vivo appears to be crucial for the success of antiangiogenic therapy based on integrin antagonism. Precise documentation of integrin receptor levels will allow appropriate selection of patients who will most likely benefit from an antiintegron treatment regimen. Imaging can also be used to provide an optimal dosage and time course for treatment based on receptor occupancy studies. In addition, imaging integrin expression will be important to evaluate antiintegron treatment efficacy and to develop new therapeutic drugs with favorable tumor targeting and in vivo kinetics. We labeled the dimeric RGD peptide E[c(RGDyK)]<sub>2</sub> with  $^{18}\text{F}$  and evaluated its tumor-targeting efficacy and pharmacokinetics of  $^{18}\text{F}$ -FB-E[c(RGDyK)]<sub>2</sub> ( $^{18}\text{F}$ -FRGD2).

**Methods:** E[c(RGDyK)]<sub>2</sub> was labeled with  $^{18}\text{F}$  by conjugation coupling with *N*-succinimidyl-4- $^{18}\text{F}$ -fluorobenzoate ( $^{18}\text{F}$ -SFB) under a slightly basic condition. The in vivo metabolic stability of  $^{18}\text{F}$ -FRGD2 was determined. The diagnostic value after injection of  $^{18}\text{F}$ -FRGD2 was evaluated in various xenograft models by dynamic microPET followed by ex vivo quantification of tumor integrin level.

**Results:** Starting with  $^{18}\text{F}$ -Kryptofix 2.2.2./K<sub>2</sub>CO<sub>3</sub> solution, the total reaction time for  $^{18}\text{F}$ -FRGD2, including final high-performance liquid chromatography purification, is about  $200 \pm 20$  min. Typical decay-corrected radiochemical yield is  $23\% \pm 2\%$  ( $n = 20$ ).  $^{18}\text{F}$ -FRGD2 is metabolically stable. The binding potential extrapolated from graphical analysis of PET data and Logan plot correlates well with the receptor density measured by sodium dodecyl sulfate polyacrylamide electrophoresis and autoradiography in various xenograft models. The tumor-to-background ratio at 1 h after injection of  $^{18}\text{F}$ -FRGD2 also gives a good linear relationship with the tumor tissue integrin level. **Conclusion:** The dimeric RGD peptide tracer  $^{18}\text{F}$ -FRGD2, with high integrin specificity and favorable excretion profile, may be translated into the clinic for imaging integrin  $\alpha_v\beta_3$  expression. The binding potential calculated from simplified tracer kinetic modeling such as the Logan plot appears to be an excellent indicator of tumor integrin density.

**Key Words:** molecular imaging; integrin  $\alpha_v\beta_3$ ; dimeric RGD peptide; dynamic microPET; Logan plot

**J Nucl Med** 2006; 47:113–121

Cell adhesion receptors of the integrin family, which are responsible for a wide range of cell-extracellular matrix and cell-cell interactions, have been well studied in many tumor types (1). One of the most prominent members of this receptor class is  $\alpha_v\beta_3$  integrin, which is related to several pathologic processes and is being investigated intensively (2). The cell adhesion molecule integrin  $\alpha_v\beta_3$  is highly expressed on activated endothelial cells (endothelial cells undergo angiogenesis and vascular remodeling) and solid tumor cells, particularly in pathways stimulated by vascular endothelial growth factor (3–5). It is not expressed on mature vessels or on nonneoplastic epithelium. The expression of integrin  $\alpha_v\beta_3$  on sprouting capillary cells and its interaction with specific matrix ligands has been shown to play a key role in angiogenesis and metastasis (6). The ability to noninvasively visualize and quantify  $\alpha_v\beta_3$  integrin expression level will provide new opportunities to document tumor (tumor cells and sprouting tumor vasculature) receptor expression, more appropriately select patients considered for antiintegron treatment, and monitor treatment efficacy in integrin-positive patients (7). Contrast-enhanced ultrasound with microbubbles targeted to  $\alpha_v$  integrins expressed on the neovascular endothelium has been used to image tumor integrin status in addition to tumor microvascular blood volume and blood velocity, which can be easily detected with nontargeted microbubbles (8–10). In an animal model, Sipkins et al. (11) recently demonstrated that it is feasible to image  $\alpha_v\beta_3$  expression using MRI and antibody-coated paramagnetic liposomes. It has also been shown that near-infrared fluorescent dye conjugated cyclic RGD peptide was able to visualize subcutaneously inoculated integrin-positive tumors (12,13). To date, most of the studies have been focused on developing suitably radiolabeled small RGD peptide antagonists of  $\alpha_v\beta_3$  as radiopharmaceuticals for SPECT and PET imaging applications (7,14).

For radionuclide imaging of integrin expression in vivo, the tumor-targeting efficacy and in vivo kinetic profile are highly related to the receptor-binding affinity and specificity, hydrophilicity, molecular size, and overall molecular charge of the resulting radiotracer. Initial studies with  $^{18}\text{F}$ -labeled monomeric RGD peptides indicated moderate

Received Jun. 14, 2005; revision accepted Sep. 19, 2005.

For correspondence or reprints contact: Xiaoyuan Chen, PhD, Department of Radiology, 1201 Welch Rd., P095, Stanford University, Stanford, CA 94305-5484.

E-mail: shawchen@stanford.edu

initial uptake in integrin-positive tumors, but the rapid tumor washout and unfavorable hepatobiliary excretion route of this type of tracer limited their further applications, especially in an attempt to detect lesions in the lower abdomen (15,16). The *in vivo* pharmacokinetics of the monomeric RGD peptide tracers was significantly improved by incorporation of a heterofunctional sugar or poly(ethylene glycol) moiety between the RGD peptide and the  $^{18}\text{F}$ -labeling prosthetic group ( $\pm$ )-2- $^{18}\text{F}$ -fluoropropionate for RGD-containing glycopeptide (17–19) and 4- $^{18}\text{F}$ -fluorobenzoyl for PEGylated RGD peptide (20,21). Both compounds had fast blood clearance, rapid and moderate tumor uptake, and moderate tumor washout, resulting in a high tumor-to-background ratio.

We recently found that the receptor-binding characteristics of dimeric and multimeric RGD peptides would be better than that of monomeric RGD peptide based on polyvalency (22–25). The receptor binding of the one RGD domain significantly enhances the local concentration of the other RGD domain in the vicinity of the receptor, which may lead to a faster rate of receptor binding or a slower rate of dissociation from the radiolabeled RGD dimer. The dimeric RGD peptide with almost 1 order of magnitude higher integrin-binding affinity than the monomeric analog is thus labeled with  $^{18}\text{F}$  (24).  $^{18}\text{F}$ -FB-E[c(RGDyK)]<sub>2</sub> ( $^{18}\text{F}$ -FRGD<sub>2</sub>) showed predominant renal excretion and almost twice as much tumor uptake in the same animal model as compared with the monomeric tracer  $^{18}\text{F}$ -FB-c(RGDyK). In this study we further evaluated this tracer in various pre-clinical animal models to measure the metabolic stability and to visualize and quantify integrin  $\alpha_v\beta_3$  expression *in vivo*.

## MATERIALS AND METHODS

### Materials

All chemicals obtained commercially were used without further purification. Dimeric RGD peptide E[c(RGDyK)]<sub>2</sub> was synthesized as previously described (22–25). No-carrier-added  $^{18}\text{F}$ -F<sup>−</sup> was obtained from PETNET Inc. The  $^{18}\text{F}$ -F<sup>−</sup> was trapped on an anion-exchange resin and then eluted with 0.5 mL K<sub>2</sub>CO<sub>3</sub> (2 mg/mL in H<sub>2</sub>O) combined with 1 mL Kryptofix 2.2.2. (Sigma-Aldrich) (10 mg/mL in acetonitrile).

Semipreparative reversed-phase high-performance liquid chromatography (HPLC) was accomplished by using a Dionex P680 chromatography system with a UVD 170U detector and a solid-state radiation detector (model 105S; Carroll & Ramsey Associates). Purification was performed with a Vydac 218TP510 protein and peptide column (5  $\mu\text{m}$ ; 250  $\times$  10 mm). The flow rate was 5 mL/min. The mobile phase was changed from 95% solvent A (0.1% trifluoroacetic acid [TFA] in water) and 5% solvent B (0.1% TFA in acetonitrile) (0–2 min) to 35% solvent A and 65% solvent B at 32 min. The analytic HPLC method was performed with the same gradient system but with a Vydac 218TP54 column (5  $\mu\text{m}$ ; 250  $\times$  4.6 mm) and a flow rate of 1 mL/min. The absorbance was monitored at 218 nm. Reversed-phase extraction C<sub>18</sub> Sep-Pak cartridges (Waters) were pretreated with methanol and water before use.

### Radiochemistry

We have previously reported the synthesis of  $^{18}\text{F}$ -FB-E[c(RGDyK)]<sub>2</sub> ( $^{18}\text{F}$ -FRGD<sub>2</sub>) (24). In this study we systematically investigated the effect of pH, temperature, and reaction time on the coupling yield between *N*-succinimidyl-4- $^{18}\text{F}$ -fluorobenzoate ( $^{18}\text{F}$ -SFB) and dimeric RGD peptide E[c(RGDyK)]<sub>2</sub>. In brief,  $^{18}\text{F}$ -SFB was purified by semipreparative HPLC. The appropriate fractions were collected and diluted with water and trapped by a C<sub>18</sub> cartridge. The cartridge was then washed with water and blown dry with argon.  $^{18}\text{F}$ -SFB was reeluted with acetonitrile and rotary evaporated to dryness. The dried  $^{18}\text{F}$ -SFB was then redissolved in dimethyl sulfoxide (200  $\mu\text{L}$ ) and added to the E[c(RGDyK)]<sub>2</sub> (200  $\mu\text{g}$ , 0.15  $\mu\text{mol}$ ) dissolved in sodium phosphate buffer (800  $\mu\text{L}$ ). Final purification was accomplished by semipreparative HPLC. The HPLC fractions containing the activity was then combined and evaporated with a stream of argon to remove acetonitrile. The pH of the resulting aqueous solution was adjusted to 7.0 with 0.1N NaOH and passed through an activated Waters C<sub>18</sub> Sep-Pak cartridge, washed with water, and eluted with 200- $\mu\text{L}$  portions of 80% ethanol. The ethanol fractions were pooled and evaporated to a small volume. The activity was finally reconstituted in phosphate-buffered saline (PBS) and passed through a 0.22- $\mu\text{m}$  Millipore filter into a sterile multidose vial for *in vivo* applications.

### Cell Lines

Six cell lines were used for *in vitro* and *in vivo* experiments. All cells were obtained from the American Type Culture Collection and all culture media were obtained from Invitrogen Co. (GIBCO). U87MG glioblastoma cells were grown in Dulbecco's modified Eagle medium (DMEM, low glucose), MDA-MB-435 breast cancer carcinoma cells were grown in Leibovitz's L15 medium, C6 rat glioma cells were grown in DMEM (high glucose), PC-3 prostate adenocarcinoma and A549 lung carcinoma cells were grown in F-12K nutrient mixture (Kaighn's modification), and NCI-H1975 non-small cell lung cancer cells were grown in RPMI 1640 medium. All cell lines were cultured in the medium supplemented with 10% (v/v) fetal bovine serum at 37°C.

### Radioligand-Binding Measurements

U87MG, MDA-MB-435, C6, PC-3, A549, and NCI-H1975 cell lines were grown as described.  $^{125}\text{I}$ -Echistatin (specific activity, 74 TBq/mmol) was purchased from Amersham. For cell receptor assay studies, Millipore 96-well filter plates were added with different concentrations (0–100 nmol/L) of echistatin in binding buffer (20 mmol/L Tris, 150 mmol/L NaCl, 2 mmol/L CaCl<sub>2</sub>, 1 mmol/L MgCl<sub>2</sub>, 1 mmol/L MnCl<sub>2</sub>, 0.10% bovine serum albumin, pH 7.4), and 555 Bq  $^{125}\text{I}$ -echistatin (in 50  $\mu\text{L}$  binding buffer) in each well. The cells in 50- $\mu\text{L}$  suspension (2  $\times$  10<sup>5</sup> cells/well) were seeded and the total volume for each well was adjusted to 200  $\mu\text{L}$  with binding buffer. The mixture was incubated for 2 h by shaking at room temperature. At the end of the incubation period, the cells were filtered with the use of a Millipore Multiscreen vacuum manifold and washed twice with cold binding buffer. The hydrophilic polyvinylidene difluoride (PVDF) filters were then collected and the radioactivity was determined using a NaI(Tl)  $\gamma$ -counter (Packard Instruments Co.). Nonspecific binding was determined with 100 nmol/L of echistatin. Scatchard plots were derived by plotting bound/free ligand versus. bound ligand and the maximum number of binding sites (B<sub>max</sub>) were

calculated by analyzing the data with nonlinear regression by use of GraphPad Prism software (version 4).

## Animals Models

All animal experiments were performed under a protocol approved by Stanford's Administrative Panel on Laboratory Animal Care. The MDA-MB-435 breast cancer model was established by orthotopic injection of  $5 \times 10^6$  cells into the left mammary fat pad. The PC-3 prostate cancer model was obtained by injecting a mixture of  $5 \times 10^6$  cells suspended in 50  $\mu\text{L}$  F-12K medium and 50  $\mu\text{L}$  Matrigel (BD BioSciences) into the right front leg of male athymic nude mice. The other 4 tumor models (U87MG, C6, NCI-H1975, and A549) were established in a way similar to that of the PC-3 model except that female nude mice were used. The mice were used for microPET studies when the tumor volume reached 300–400  $\text{mm}^3$  (2–3 wk after inoculation for NCI-H1975 and C6; 3–4 wk after inoculation for U87MG, MDA-MB-435, PC-3, and A549). Three mice were used for each tumor models.

## Metabolic Stability

Nude mice bearing U87MG tumors were intravenously injected with 37 MBq of  $^{18}\text{F}$ -FRGD2. The animals were sacrificed and dissected 60 min after tracer injection. Blood, urine, liver, kidneys, and tumor were collected. Blood was immediately centrifuged for 5 min at 13,200 rpm. Organs were homogenized using an IKA Ultra-Turrax T8 (IKA Works Inc.), suspended in 1 mL of PBS, pH 7.4, and centrifuged for 5 min at 13,200 rpm. After removal of the supernatants, the pellets were washed with 500  $\mu\text{L}$  of PBS. For each sample supernatants of both centrifugation steps were combined and passed through Sep-Pak C<sub>18</sub> cartridges. The urine sample was directly diluted with 1 mL of PBS and then passed through a Sep-Pak C<sub>18</sub> cartridge. The cartridges were washed with 2 mL of water and eluted with 2 mL of acetonitrile containing 0.1% TFA. The combined aqueous and organic solutions were concentrated to about 1 mL by rotary evaporation. The residues were passed through a 0.22- $\mu\text{m}$  Millipore filter and then injected onto an analytic HPLC column using a flow rate of 1 mL/min and a gradient as described. Radioactivity was monitored using a solid-state radiation detector. At the same time, the eluent was also collected by a fraction collector (0.5 min/fraction) and the activity of each fraction was measured with the  $\gamma$ -counter. The HPLC analysis was performed in duplicate and the extraction efficiency was determined in triplicate.

## microPET

PET was performed using a microPET R4 rodent model scanner (Concorde Microsystems Inc.). The scanner has a computer-controlled bed and 10.8-cm transaxial and 8-cm axial fields of view (FOVs). It has no septa and operates exclusively in the 3-dimensional list mode. Animals were placed near the center of the FOV of the microPET scanner, where the highest image resolution and sensitivity are available. The microPET studies were performed by tail-vein injection of 3.7 MBq (100  $\mu\text{Ci}$ ) of  $^{18}\text{F}$ -FRGD2 under isoflurane anesthesia. The 60-min dynamic ( $5 \times 60$  s,  $5 \times 120$  s,  $5 \times 180$  s,  $6 \times 300$  s) microPET data acquisition (total of 21 frames) was started 3 min after radiotracer injection. Static images at 2- and 3-h time points were also acquired as 10-min static images. The images were reconstructed by a 2-dimensional ordered-subsets expectation maximum (OSEM) algorithm. No correction was necessary for attenuation or scatter.

## Image Analysis

For each microPET scan, regions of interest (ROIs) were drawn over each tumor, normal tissue, and major organs by using the ASI Pro 5.2.4.0 program (Concorde Microsystems Inc.) on decay-corrected, whole-body coronal images. The maximum radioactivity concentration (accumulation) within a tumor or an organ was obtained from mean pixel values within the multiple ROI volume, which were converted to  $\mu\text{Ci}/\text{mL}/\text{min}$  by using a calibration constant (26). Assuming a tissue density of 1 g/mL, the ROIs were converted to  $\mu\text{Ci}/\text{g}/\text{min}$  and then divided by the administered activity to obtain an imaging ROI-derived percentage administered activity per gram of tissue (%ID/g).

The dynamic PET data were used for both tracer kinetic modeling and human dosimetry estimation. Graphical analysis (27,28) of the PET data used normalized integrated activity in the tumor versus the normalized integrated activity in the muscle (Equation 1). The ratio of integrated tumor uptake divided by tumor uptake was set as the  $y$ -axis. The ratio of integrated reference tissue uptake divided tumor uptake was set as the  $x$ -axis of a Logan plot (here we select muscle as reference tissue because of its low integrin expression). The slope of the linear portion of the Logan plot was distribution volume ratio (DVR). The binding potential (BP) = DVR – 1.

$$\frac{\int_0^T C_t(t) dt}{C_t(T)} = \text{DVR} \times \frac{\int_0^T C_r(t) dt}{C_r(T)} + C. \quad \text{Eq. 1}$$

## Quantitation of Tumor Integrin Level

Tumor-bearing mice were sacrificed 24 h after dynamic microPET. The quantitation of tumor tissue integrin level was performed by incubating Nonidet P-40 (NP-40; GE Healthcare)-solubilized tumor tissue lysate with  $^{125}\text{I}$ -echistatin in the presence of increasing concentrations of nonradiolabeled echistatin (29). Tumor tissue integrin expressions were then quantified by sodium dodecyl sulfate polyacrylamide gel electrophoresis (SDS-PAGE) and autoradiography. Briefly, solubilized tumor tissues were obtained by addition of 0.1 mL/cm<sup>2</sup> of lysis buffer (0.05 mol/L HEPES [pH 7.4], 1% NP-40, 1 mmol/L CaCl<sub>2</sub>, and 1 mmol/L MgCl<sub>2</sub>). After incubating on ice for 10–20 min, the samples were collected and centrifuged at 15,000 rpm for 3 min. The resulting solution was then analyzed for total protein content by a Micro BCA (bicinchoninic acid) protein assay (Pierce Biotechnologies). Samples were assayed in triplicate. Twenty micrograms of proteins were incubated in a final volume of 25  $\mu\text{L}$  in binding buffer in the presence of 1.85 kBq of  $^{125}\text{I}$ -echistatin and various amounts of echistatin (1–100 nmol/L). After a 2-h incubation at room temperature, the mixtures were loaded onto 4%–10% SDS-PAGE gels. After electrophoresis, the gels were dried and subjected to autoradiography overnight. Radioactive bands were developed and quantified in a Cyclone PhosphoImager system (Perkin-Elmer Inc.). The same dose of  $^{125}\text{I}$ -echistatin without forming a complex with integrin was used as a standard, and 15 ng of purified integrin  $\alpha_v\beta_3$  (Chemicon) was used as a positive control and molecular marker. Each competition curve was then fitted by the Hill equation (GraphPad). The linear portion of the sigmoid curve was used to generate a Scatchard transformation and  $B_{\max}$  (number of receptors/mg protein).

## Statistical Analysis

Quantitative data were expressed as mean  $\pm$  SD. Means were compared using 1-way ANOVA. The relationship between BP

values and receptor density calculated from SDS-PAGE/auto-radiography was evaluated by linear regression and Pearson correlation analyses.

## RESULTS

### Radiosynthesis

<sup>18</sup>F-Fluorination of dimeric RGD ( $\text{E}[\text{c}(\text{RGDyK})_2]$ ) was performed using <sup>18</sup>F-SFB (Fig. 1). Synthesis of <sup>18</sup>F-SFB followed a previously reported procedure except that <sup>18</sup>F-SFB was purified before coupling with an RGD dimer. It was found that the specific activity of <sup>18</sup>F-SFB with HPLC purification was higher than that with simple cartridge desalting. The subsequent purification of <sup>18</sup>F-FRGD2 was also made easier. The yield of radiochemical acylation was dependent on peptide concentration, temperature, pH, and reaction time. Starting with a <sup>18</sup>F<sup>-</sup> Kryptofix 2.2.2./ $\text{K}_2\text{CO}_3$  solution, the total reaction time, including final HPLC purification, was about  $200 \pm 20$  min. The maximum overall radiochemical yield with decay correction was  $23\% \pm 2\%$  ( $n = 20$ ). The radiochemical purity of the labeled peptide was  $>98\%$  according to analytic HPLC analysis. The specific radioactivity of <sup>18</sup>F-SFB was estimated by radio-HPLC to be 200–250 TBq/mmol. Such yield was reached by using 200  $\mu\text{g}$  of  $\text{E}[\text{c}(\text{RGDyK})_2]$  at pH 8.0 and 40°C within 20 min. Note that this yield was significantly lower than that reported for monomeric RGD peptide c(RGDyK), which was  $>40\%$  (15,16).

### Quantitation of Tumor Integrin Level

The sigmoid curves for the whole-cell binding assay using <sup>125</sup>I-echistatin as radioligand and unlabeled echistatin as competitor were obtained by nonlinear regression fitting of the data using GraphPad Prism. The density of integrin  $\alpha_v\beta_3$  receptors on the cell surface was found to be U87MG  $\gg$  NCI-H1975  $>$  MDA-MB-435  $>$  A549  $>$  PC-3  $>$  C6 (Table 1). Quantitation of tumor tissue integrin level by SDS-PAGE/autoradiography, on the other hand, revealed a different order: U87MG  $>$  MDA-MB-435  $\gg$  PC-3  $>$  C6  $>$  NCI-H1975  $>$  A549 (Table 1). A representative autoradio-

TABLE 1

Receptor Density for U87MG, MDA-MB-435, C6, PC-3, NCI-H1975, and A549 Tumor Cells Determined by Cell-Binding Assay ( $n = 3$ ) and Corresponding Tumor Tissues Measured by Ex Vivo SDS-PAGE/Autoradiography

Tumor type	Cell receptor density (no. of receptors/cell)	Tumor receptor density (no. of receptors/mg protein)
U87MG	$(1.28 \pm 0.46) \times 10^5$	$4.24 \times 10^{12}$
MDA-MB-435	$(1.99 \pm 0.26) \times 10^4$	$2.80 \times 10^{12}$
C6	$(1.48 \pm 0.28) \times 10^3$	$1.51 \times 10^{11}$
PC-3	$(2.76 \pm 0.95) \times 10^3$	$3.58 \times 10^{11}$
NCI-H1975	$(4.42 \pm 0.59) \times 10^4$	$2.35 \times 10^{10}$
A549	$(1.34 \pm 1.25) \times 10^4$	$1.75 \times 10^{10}$

gram of a competition experiment for A549 tumor is shown in Figure 2A. The linear portion of the sigmoid curve (Fig. 2B) was used to generate the Scatchard transformation and the  $B_{\max}$  (Fig. 2C).

### Metabolism of <sup>18</sup>F-FRGD2

The metabolic stability of <sup>18</sup>F-FRGD2 was determined in mouse blood and urine samples and in liver, kidneys, and tumor homogenates 60 min after tracer injection. For all organs, extraction efficiency was between 78% and 93% (Table 2). Between 0.2% and 20% of the total activity could not be trapped on the  $\text{C}_{18}$  cartridges, which might be attributed to very hydrophilic metabolites or protein-bound activity. The lowest extraction efficiency was found for the U87MG tumor and the highest was found for the blood. HPLC analysis results of the soluble fractions of the different samples are shown in Figure 3. The average fraction of intact tracer was between 80% and 95% (Table 2). The highest metabolic stability of <sup>18</sup>F-FRGD2 was found in urine (95.5% intact tracer). Although we did not identify the composition of the metabolites, we found that all of the metabolites eluted earlier from the HPLC column than the parent compound. A minor peak was found at 12 min for all samples. Another metabolite peak was found at about 4 min for the tumor. No defluoridation of <sup>18</sup>F-FRGD2 was observed.

### PET Study

The dynamic microPET scans were performed for all 6 tumor models. Selected coronal images at different time points after injection of <sup>18</sup>F-FRGD2 in a U87MG tumor mouse are shown in Figure 4. High tumor activity accumulation was observed as early as 5 min after injection. Most radioactivity in nontarget tissues was cleared at 70 min after injection. Uptake in the U87MG tumor, kidneys, liver, and lung was  $3.81 \pm 0.80$ ,  $2.25 \pm 0.43$ ,  $1.10 \pm 0.22$ , and  $0.59 \pm 0.18$  %ID/g, respectively. Time–activity curves showed that this tracer excreted predominantly through the renal route (Fig. 5A). Diversified tumor uptake patterns of <sup>18</sup>F-FRGD2 were found in different xenograft models

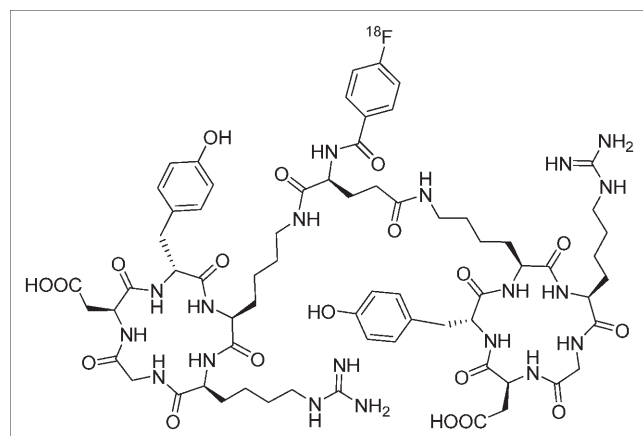
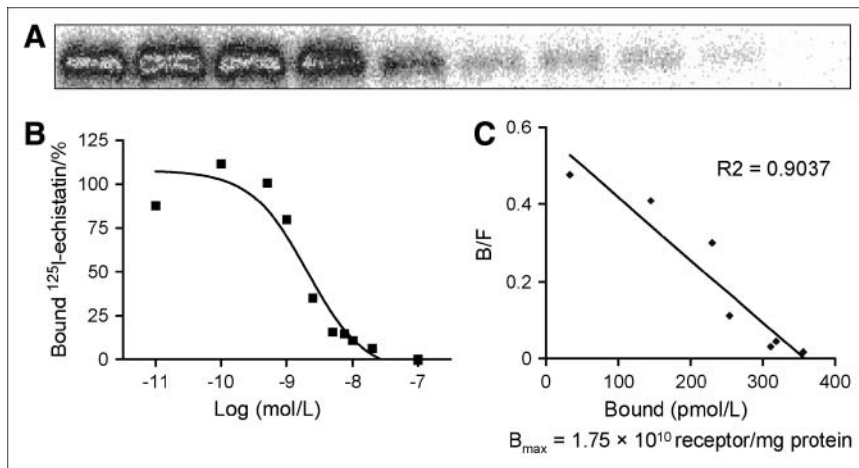


FIGURE 1. Schematic structure of <sup>18</sup>F-FB-E[c(RGDyK)]<sub>2</sub> (<sup>18</sup>F-FRGD2).



**FIGURE 2.** Analysis of non-small cell lung cancer A549 tumor tissue integrin level by SDS-PAGE/autoradiography. NP-40-solubilized tumor tissue lysate (30 µg) was incubated with  $1 \times 10^5$  cpm of <sup>125</sup>I-echistatin for 2 h and increasing concentrations of echistatin. After separation on 0.6% SDS-PAGE, an autoradiogram was obtained (A) and each radioactivity band was quantified by using a Phospholmager system (B). Scatchard transformation of the sigmoid curve generated tissue receptor density (number of receptors/mg tissue) (C).

(Fig. 5B). The U87MG tumor had the highest tumor tissue integrin and tumor cell integrin levels and also had the highest initial tumor uptake but also had the most rapid tumor washout, reaching a plateau after 50 min following injection. The tumors with low magnitude of tumor uptake had minimal tumor washout, providing reasonably high tumor contrast at late time points when nonspecific activity accumulation in the normal organs had been mostly cleared.

#### Tracer Kinetic Modeling and Correlation Analysis

The Logan plot is a graphical method of analysis, applicable to ligands that bind reversibly to receptors or enzymes (27,28). This method can calculate the distribution

volume for dynamic PET data before steady state is actually reached. We used 26.5 min as the starting point for linear regression of the dynamic microPET studies because all graphs became linear after that point, with the slope being DVR (Fig. 5C). The calculated BP ( $B_{max}/K_d$ ) ( $K_d$  is dissociation constant) for <sup>18</sup>F-FRGD2 in the U87MG, MDA-MB-435, C6, PC-3, NCI-H1975, and A549 tumors using muscle as reference tissue was found to be 29.5, 17.5, 5.8, 1.9, 4.1, and 3.8, respectively.

A linear relationship was found between the BP values calculated from graphical analysis of dynamic microPET and the  $B_{max}$  values measured from SDS-PAGE/autoradiograms ( $R^2 = 0.96$ ;  $P = 0.005$ ) (Fig. 6A). The tumor-to-contralateral background ratios did not provide the same level of correlation with the tumor tissue integrin density at early time points (e.g., Pearson correlation coefficient  $R^2$  was 0.86 at 5 min and 0.88 at 30 min after injection.) (Figs. 6C and 6D). At 1 h after injection, a good linear relationship was found between the tumor-to-background ratio and the tumor integrin level (Fig. 6E). Interestingly, the tumor cell integrin level did not have the same level of correlation with tumor contrast or BP (Figs. 6B and 6F).

#### DISCUSSION

Monomeric RGD peptide c(RGDyV) was first labeled by Haubner et al. with <sup>125</sup>I (30). This relatively lipophilic compound had rapid tumor washout and unfavorable hepatobiliary excretion. The resulting high liver and intestinal activity accumulation limited its further application. Glycosylation of the RGD peptide decreased the lipophilicity and, consequently, the hepatic uptake (31). The same glycopeptide was then labeled with <sup>18</sup>F via the ( $\pm$ )-2-<sup>18</sup>F-fluoropropionate prosthetic group (17–19). The so-called <sup>18</sup>F-galacto-RGD demonstrated integrin  $\alpha_v\beta_3$ -specific tumor uptake in the integrin-positive M21 melanoma xenograft model. Initial clinical trials in healthy volunteers and a limited number of cancer patients revealed that this tracer can be administered safely to patients and is capable of delineating certain lesions that are integrin positive (19). The

**TABLE 2**  
Extraction Efficiency and Elution Efficiency Data and HPLC Analysis of Soluble Fraction of Tissue Samples at 60 Minutes After Injection

Fraction	Blood	Urine	Liver	Kidney	U87MG
Extraction efficiency (%)					
Unsoluble fraction*	6.9	ND	12.6	16.5	21.7
Soluble fraction†	93.1	ND	87.4	83.5	78.3
Elution efficiency (%)					
Nonretained fraction‡	2.1	0.2	37.1	14.5	15.2
Wash water§	0.6	0.7	3.0	1.6	3.0
Acetonitrile eluent¶	97.2	99.1	59.9	83.8	81.8
HPLC analysis (%)					
Intact tracer	90.6	95.5	93.5	87.8	79.9

\*Amount of activity that was retained in pellets.

†Amount of activity that was extracted to PBS solution.

‡Amount of activity that could not be trapped on C<sub>18</sub> cartridge.

§Amount of activity that was eluted from C<sub>18</sub> cartridge using 2 mL water.

¶Amount of activity that was eluted from C<sub>18</sub> cartridge using 2 mL acetonitrile with 0.1% TFA.

ND = not determined.

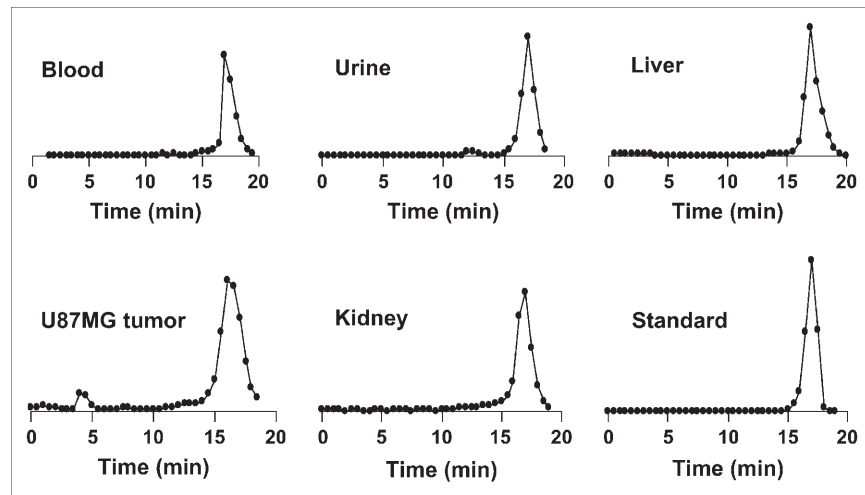


**FIGURE 3.** Representative HPLC profiles of the reference compound  $^{18}\text{F}$ -FRGD2, the soluble fractions of blood and urine samples, tumor, kidney, and liver homogenates collected 1 h after tracer injection. Dimeric RGD peptide tracer is metabolically stable in most organs and tissues.

Wilcoxon signed rank test showed that RGD/PET standardized uptake value (SUV) analysis might be related to tumor vessel density (CD31 staining). Despite the initial success of this tracer in preclinical and clinical studies, several unresolved issues diminished the enthusiasm. A more appropriate RGD peptide probe will almost certainly be required. As a monomeric RGD peptide tracer,  $^{18}\text{F}$ -galacto-RGD had relatively low integrin-binding affinity and, thus, only moderate tumor SUVs (18,19). Although glycosylation improved the pharmacokinetic behavior of an otherwise hydrophobic RGD peptide tracer, prominent activity accumulation in the kidneys, spleen, liver, and intestines was still found in both preclinical animal models and human studies. Furthermore, it is not clear whether the tumor contrast from  $^{18}\text{F}$ -galacto-RGD/PET is a true reflection of the level of tumor integrin  $\alpha_v\beta_3$  expression *in vivo*.

To correlate  $\alpha_v\beta_3$  expression and tumor uptake of  $^{18}\text{F}$ -galacto-RGD, subcutaneous tumor models were produced by inoculating a mixed population of M21 (integrin positive) and M21-L (integrin negative) cells. The tumor-to-background ratios obtained from PET and the tumor-to-muscle ratios obtained from direct tissue sampling were then compared with relative  $\alpha_v$  integrin expression measured by Western blot analysis under a reducing condition. Relatively poor correlation was found (Pearson correlation coefficient  $R^2$  was around 0.56). Initial clinical translation of this tracer also gave mixed

results. A patient with a stage IV malignancy and multiple metastases in liver, skin, and lower abdomen had marked uptake of  $^{18}\text{F}$ -FDG but failed to have any  $^{18}\text{F}$ -galacto-RGD (19). Because the tumor sections were not validated by immunohistochemical staining, it is unclear whether these lesions are integrin negative or the tracer is insensitive.

Because the monomeric RGD pentapeptide in a bent conformation has been optimized to fit into the deep cleft between the  $\alpha$ - and  $\beta$ -units of integrin  $\alpha_v\beta_3$  (32), it is very unlikely that one can significantly improve integrin affinity and selectivity of the monomeric RGD peptide by fine tuning the pentapeptide configuration. Thus, we and others applied a polyvalency effect (22–25,33,34) to develop dimeric and multimeric RGD peptides, with repeating cyclic pentapeptide units connected by glutamates. Initial evaluation of the dimeric RGD peptide tracer  $^{18}\text{F}$ -FRGD2 in the subcutaneous U87MG glioma model showed excellent tumor integrin-targeting efficacy and favorable *in vivo* kinetics of this tracer. Although a receptor-blocking experiment demonstrated integrin specificity of the tracer, it is unknown whether the magnitude of tumor uptake is able to document tumor integrin density *in vivo*. In this study we evaluated the ability of noninvasive PET to quantify the tumor integrin level.

Quantification of cell or tissue integrin  $\alpha_v\beta_3$  expression by immunoblotting is technically challenging because of

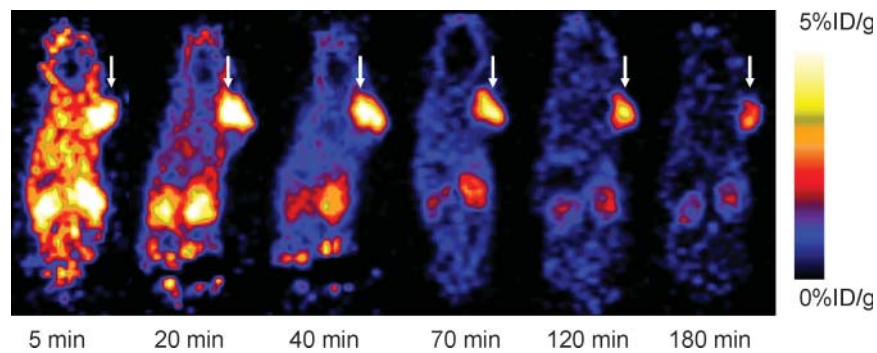


**FIGURE 4.** Dynamic microPET study of U87MG tumor-bearing mouse over 60 min after injection of  $^{18}\text{F}$ -FRGD2 (3.7 MBq [100  $\mu\text{Ci}$ ]), static scans at 2- and 3-h time points were also conducted to complete the tracer kinetic study. Decay-corrected, whole-body coronal images that contain the tumor are shown. (Reprinted with permission of BioTechniques to reproduce parts of Figure 6.)

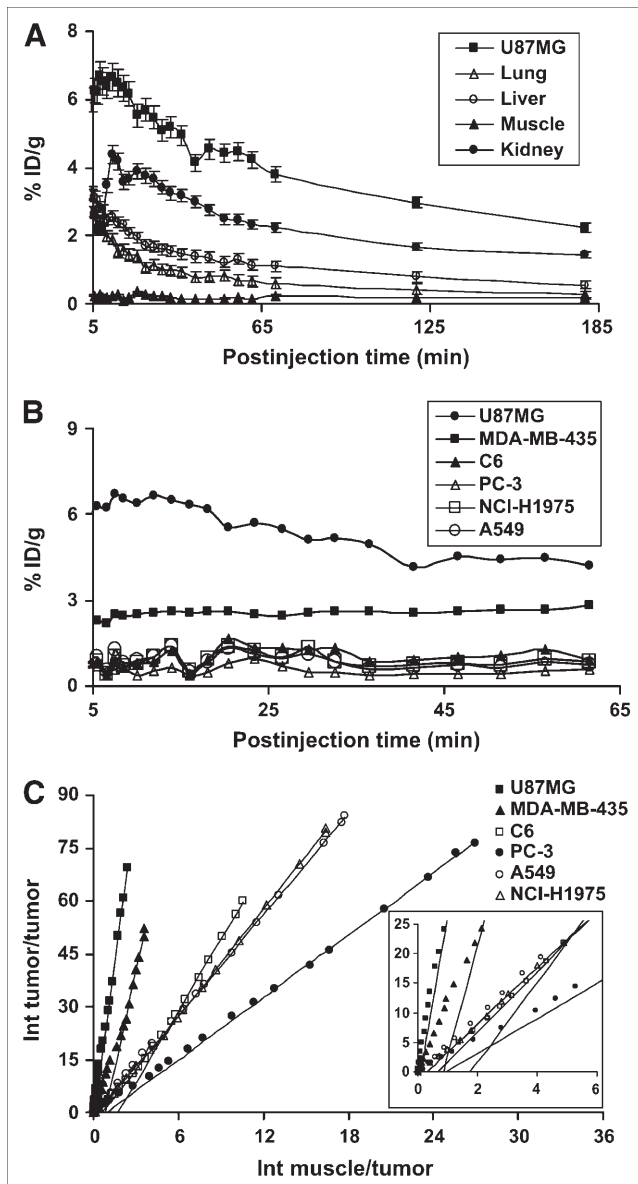


**FIGURE 5.** (A) Time-activity curves derived from 60-min dynamic and 70-min, 120-min, and 180-min static microPET study. ROIs are shown as mean %ID/g  $\pm$  SD ( $n = 3$ ). (B) Comparison of tumor uptake in nude mice derived from 60-min dynamic microPET scans. (C) Logan plots derived from 60-min dynamic microPET data, which showed excellent linearity of normalized integrated (Int) tumor activity vs. normalized integrated muscle tissue activity effective for time  $>25$  min. Slopes of fits represent DVRs. (Reprinted with permission of BioTechniques to reproduce parts of Figure 6.)

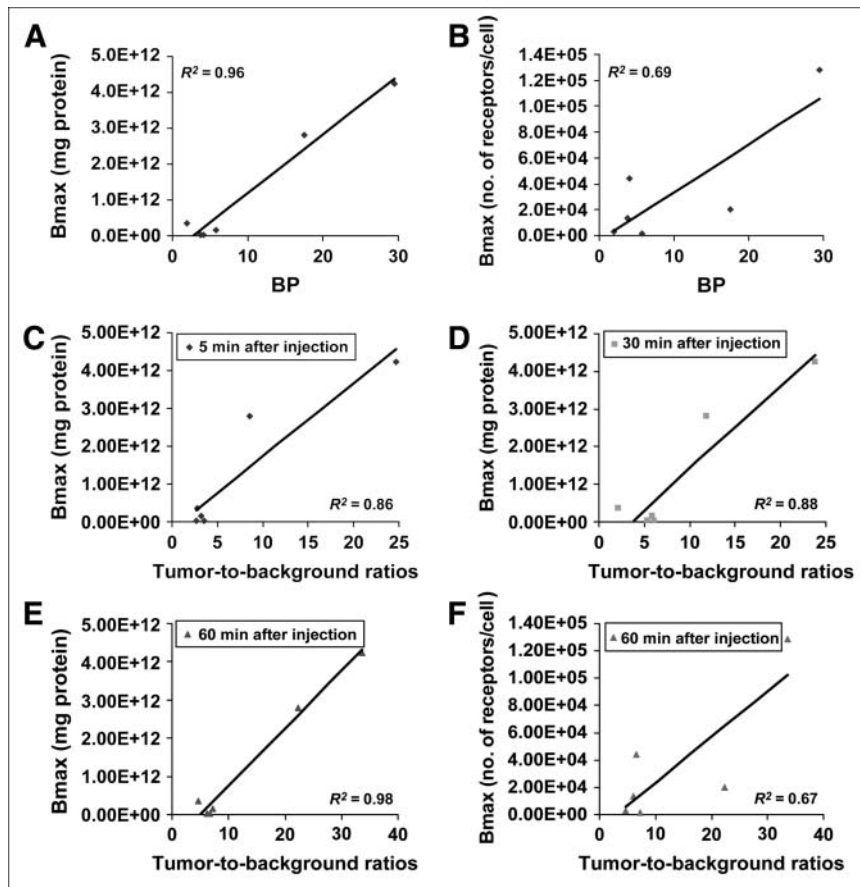
the heterodimeric feature of this G-protein receptor. Both anti- $\alpha_v$  and anti- $\beta_3$  antibodies are thus needed to confirm the presence of integrin  $\alpha_v\beta_3$  and, yet, it is difficult to be quantitative (35). It was recently reported that  $^{125}\text{I}$ -echistatin forms an SDS-stable complex with certain integrins (resistant to 0.6% SDS) in the absence of chemical cross-linkers, reducing conditions, and heating (29). We only detected a single radioactive band for all of the tumor tissue lysates tested. On the basis of the cross-reactivity of

this band with selective anti- $\alpha$ - and  $\beta$ -subunit antibodies, it is suggested that  $^{125}\text{I}$ -echistatin binds to  $\alpha_v\beta_3$ . A control experiment with pure integrin  $\alpha_v\beta_3$ ,  $\alpha_v\beta_5$ , and  $\alpha_5\beta_1$  proteins also indicated that the single band detected from cell and tissue lysates is  $\alpha_v\beta_3$  (data not shown). Based on the 6 tumor models tested, the BP derived from tracer kinetic analysis correlated well with the tumor integrin expression level measured by SDS-PAGE/autoradiography. To our knowledge, this is the first report that one can quantify integrin expression *in vivo* by noninvasive PET, which provides the basis for precise documentation of tumor integrin levels without biopsy. It is also worth mentioning that the tumor-to-background ratio at 60 min after injection had better correlation with tumor integrin levels than those at 5 and 30 min after injection. (Figs. 6C–6E), presumably due to the presence of nonspecific uptake, such as perfusion and vascular permeability at early time points. Tumor contrast had a considerable correlation with the tumor tissue integrin level at late time points. Overall, tracer kinetic modeling allows a better quantitative measurement of  $\alpha_v\beta_3$  expression by PET. It is likely that the tumor-to-background or tumor-to-muscle ratios reported by Haubner et al. in their melanoma tumor model with mixed population of M21 and M21-L cells might have been more positively correlated with tumor integrin levels if the dissected tumors were quantified by SDS-PAGE/autoradiography instead of Western blots. The sample size in this study is rather low. We tested only 6 tumor models. More animal models (subcutaneous, orthotopic, and even transgenic) at different stages of tumor growth are needed to further validate the Pearson correlation analysis and to determine whether tracer kinetic modeling is superior to tumor-to-background contrast. It would be clinically more advantageous to have a good correlation between tumor-to-background ratios or SUVs and tumor integrin expression level quantified by receptor autoradiography, as documentation of the patient integrin level may be obtained without dynamic scans.

We also note that neither the BP values calculated from the Logan plot nor the tumor-to-background contrast quantified from microPET had a good linear relationship with tumor cell integrin levels measured by the receptor-binding assay. It is well-documented that integrin  $\alpha_v\beta_3$  is expressed not only on a variety of tumor cells but also is present at a high level on activated endothelial cells during angiogenesis. The integrin expression on tumor cells grown in tissue culture does not necessarily reflect the tumor tissue integrin level. For example, SDS-PAGE/autoradiography analysis of MDA-MB-435 breast cancer cell lysates and tissue lysates found that the tumor tissue integrin level is about 4- to 5-fold higher than that of tumor cells, indicating that integrin  $\alpha_v\beta_3$  expressed on newly developed neovasculatures tends to be much higher than that on the tumor cells (data not shown).

The Logan plot is applicable to the tracers that are reversible, whereas Patlak analysis (36) is good for tracers

**FIGURE 6.** Correlation analysis is shown between tumor tissue receptor density (number of receptors/mg protein measured from SDS-PAGE/autoradiography using  $^{125}\text{I}$ -echistatin as radioligand) vs. BP (calculated from Logan plot transformation of dynamic microPET data) ( $R^2 = 0.96$ ) (A); tumor cell integrin expression (number of receptors/cell measured from whole-cell receptor-binding assay) vs. BP ( $R^2 = 0.69$ ) (B); tumor tissue receptor density vs. tumor-to-background ratios (calculated from time-activity curves derived from dynamic microPET). Coefficient of determination  $R^2$  is about 0.86, 0.87, and 0.98 at 5, 30, and 60 min after injection of  $^{18}\text{F}$ -FRGD2, respectively (C–E); tumor cell receptor density vs. tumor-to-background ratio at 60 min after injection of  $^{18}\text{F}$ -FRGD2. Coefficient of determination  $R^2$  is 0.67 (F). Data derived from 6 tumor models (U87MG, C6, MDA-MB-435, PC-3, NCI-H1975, and A549) illustrate excellent linear relationship between tumor tissue receptor density vs. BP and tumor tissue receptor density vs. tumor-to-background ratio at 1 h after injection. (Reprinted with permission of BioTechniques to reproduce parts of Figure 6.)



that are irreversible. We actually performed both Logan plot and Patlak analysis for all dynamic PET data. The Patlak curves deflected downward for the later time points, which is probably a good indication that the tracer is actually reversible. The effectiveness of the blocking of tracer uptake by unlabeled RGD peptide in a dose-dependent manner provides further evidence of the reversible receptor binding of this tracer. A flat curve of some tumor types shown in Figure 5B may still be slowly reversible, in which it may not be so evident by visual inspection of the curve shapes over 60 min. Therefore, quantification of integrin expression level by noninvasive PET may provide a unique way of documenting tumor angiogenesis, in analogy to other established tracers such as FDG for tumor metabolism, radiolabeled antibodies for cell-surface antigen, and suitably labeled annexin V for apoptosis imaging studies.

The optimized coupling yield for the dimeric RGD peptide is significantly lower than that for the monomeric RGD peptide and other peptides reported in the literature using  $^{18}\text{F}$ -SFB as synthon. The monomer with a lysine side-chain  $\epsilon$ -amino group has much less steric hindrance and a higher  $\text{pK}_a$  value than a glutamate  $\alpha$ -amino group and is, thus, more easily derivatized. Introduction of a linker to the glutamate amine will not only serve as a pharmacokinetic modifier but also modifies the flexibility and acidity of the terminal amine group for  $^{18}\text{F}$ -SFB incorporation. A further

structure–activity study is required to determine whether an appropriate amino acid linker to  $\text{E}[\text{c(RGDyK)}]_2$  will improve the radiolabeling yield without compromising the tumor targeting efficacy and in vivo kinetics of  $^{18}\text{F}$ -FRGD2.

## CONCLUSION

This study demonstrates that  $^{18}\text{F}$ -labeled dimeric RGD peptide  $^{18}\text{F}$ -FRGD2 has initial high activity accumulation in  $\alpha_v\beta_3$ -integrin-rich tumors and has some washout with time, providing high tumor-to-background ratio even at early time points.  $^{18}\text{F}$ -FRGD2 uptake in tumors with medium or low  $\alpha_v\beta_3$  levels was also low but minimal tumor washout was observed, and consequently clear tumor contrast is observable at late time points. The binding potential calculated from graphical analysis of dynamic PET data is a better indicator than the tumor-to-background contrast for tumor integrin level in various preclinical tumor models.

## ACKNOWLEDGMENTS

This work was supported, in part, by National Institute of Biomedical Imaging and Bioengineering grant R21 EB001785, Department of Defense (DOD) Breast Cancer Research Program (BCRP) Concept award DAMD17-03-1-0752, DOD BCRP IDEA award W81XWH-04-1-0697, DOD Prostate Cancer Research Program New Investigator

award DAMD1717-03-1-0143, the American Lung Association California, the Society of Nuclear Medicine Education and Research Foundation, National Cancer Institute (NCI) Small Animal Imaging Resource Program grant R24 CA93862, and NCI In Vivo Cellular Molecular Imaging Center grant P50 CA114747.

## REFERENCES

- Danen EH. Integrins: regulators of tissue function and cancer progression. *Curr Pharm Des.* 2005;11:881–891.
- Hynes RO. Integrins: bidirectional, allosteric signaling machines. *Cell.* 2002;110:673–687.
- De S, Razorenova O, McCabe NP, et al. VEGF-integrin interplay controls tumor growth and vascularization. *Proc Natl Acad Sci U S A.* 2005;102:7589–7594.
- Robinson SD, Reynolds LE, Wyder L, et al.  $\beta_3$ -Integrin regulates vascular endothelial growth factor-A-dependent permeability. *Arterioscler Thromb Vasc Biol.* 2004;24:2108–2114.
- Friedlander M, Brooks PC, Shaffer RW, et al. Definition of two angiogenic pathways by distinct  $\alpha_v$  integrins. *Science.* 1995;270:1500–1502.
- Kumar CC. Integrin  $\alpha_v\beta_3$  as a therapeutic target for blocking tumor-induced angiogenesis. *Curr Drug Targets.* 2003;4:123–131.
- Haubner R, Wester HJ. Radiolabeled tracers for imaging of tumor angiogenesis and evaluation of anti-angiogenic therapies. *Curr Pharm Des.* 2004;10:1439–1455.
- Dayton PA, Pearson D, Clark J, et al. Ultrasonic analysis of peptide- and antibody-targeted microbubble contrast agents for molecular imaging of  $\alpha_v\beta_3$ -expressing cells. *Mol Imaging.* 2004;3:125–134.
- Ellegala DB, Leong-Poi H, Carpenter JE, et al. Imaging tumor angiogenesis with contrast ultrasound and microbubbles targeted to  $\alpha_v\beta_3$ . *Circulation.* 2003;108:336–341.
- Leong-Poi H, Christiansen J, Klibanov AL, et al. Noninvasive assessment of angiogenesis by ultrasound and microbubbles targeted to  $\alpha_v$ -integrins. *Circulation.* 2003;107:455–460.
- Sipkins DA, Cheresh DA, Kazemi MR, et al. Detection of tumor angiogenesis in vivo by  $\alpha_v\beta_3$ -targeted magnetic resonance imaging. *Nat Med.* 1998;4:623–626.
- Wang W, Ke S, Wu Q, et al. Near-infrared optical imaging of integrin  $\alpha_v\beta_3$  in human tumor xenografts. *Mol Imaging.* 2004;3:343–351.
- Chen X, Conti PS, Moats RA. In vivo near-infrared fluorescence imaging of integrin  $\alpha_v\beta_3$  in brain tumor xenografts. *Cancer Res.* 2004;64:8009–8014.
- Chen X. Multimodality imaging of tumor integrin expression. *Mini Rev Med Chem.* In press.
- Chen X, Park R, Shahinian AH, et al.  $^{18}\text{F}$ -Labeled RGD peptide: initial evaluation for imaging brain tumor angiogenesis. *Nucl Med Biol.* 2004;31:179–189.
- Chen X, Park R, Tohme M, et al. MicroPET and autoradiographic imaging of breast cancer  $\alpha_v$ -integrin expression using  $^{18}\text{F}$ - and  $^{64}\text{Cu}$ -labeled RGD peptide. *Bioconjug Chem.* 2004;15:41–49.
- Haubner R, Wester HJ, Weber WA, et al. Noninvasive imaging of  $\alpha_v\beta_3$  integrin expression using  $^{18}\text{F}$ -labeled RGD-containing glycopeptide and positron emission tomography. *Cancer Res.* 2001;61:1781–1785.
- Haubner R, Kuhnast B, Mang C, et al.  $[^{18}\text{F}]$ Galacto-RGD: synthesis, radio-labeling, metabolic stability, and radiation dose estimates. *Bioconjug Chem.* 2004;15:61–69.
- Haubner R, Weber WA, Beer AJ, et al. Noninvasive visualization of the activated  $\alpha_v\beta_3$  integrin in cancer patients by positron emission tomography and  $[^{18}\text{F}]$ galacto-RGD. *PLOS Med.* [serial online]. 2005;2:e70. Accessed March 29, 2005.
- Chen X, Park R, Shahinian AH, et al. Pharmacokinetics and tumor retention of  $^{125}\text{I}$ -labeled RGD peptide are improved by PEGylation. *Nucl Med Biol.* 2004;31:11–19.
- Chen X, Park R, Hou Y, et al. MicroPET imaging of brain tumor angiogenesis with  $^{18}\text{F}$ -labeled PEGylated RGD peptide. *Eur J Nucl Med Mol Imaging.* 2004;31:1081–1089.
- Chen X, Plasencia C, Hou Y, et al. Synthesis and biological evaluation of dimeric RGD peptide-paclitaxel conjugate as a model for integrin-targeted drug delivery. *J Med Chem.* 2005;48:1098–1106.
- Chen X, Sievers E, Hou Y, et al. Integrin  $\alpha_v\beta_3$ -targeted imaging of lung cancer. *Neoplasia.* 2005;7:271–279.
- Chen X, Tohme M, Park R, et al. Micro-PET imaging of  $\alpha_v\beta_3$ -integrin expression with  $^{18}\text{F}$ -labeled dimeric RGD peptide. *Mol Imaging.* 2004;3:96–104.
- Chen X, Liu S, Hou Y, et al. MicroPET imaging of breast cancer  $\alpha_v$ -integrin expression with  $^{64}\text{Cu}$ -labeled dimeric RGD peptides. *Mol Imaging Biol.* 2004;6:350–359.
- Wu Y, Zhang X, Xiong Z, et al. microPET imaging of glioma integrin  $\alpha_v\beta_3$  expression using  $^{64}\text{Cu}$ -labeled tetrameric RGD peptide. *J Nucl Med.* 2005;46:1707–1718.
- Logan J. Graphical analysis of PET data applied to reversible and irreversible tracers. *Nucl Med Biol.* 2000;27:661–670.
- Logan J. A review of graphical methods for tracer studies and strategies to reduce bias. *Nucl Med Biol.* 2003;30:833–844.
- Thibault G. Sodium dodecyl sulfate-stable complexes of echistatin and RGD-dependent integrins: a novel approach to study integrins. *Mol Pharmacol.* 2000;58:1137–1145.
- Haubner R, Wester HJ, Reuning U, et al. Radiolabeled  $\alpha_v\beta_3$  integrin antagonists: a new class of tracers for tumor targeting. *J Nucl Med.* 1999;40:1061–1071.
- Haubner R, Wester HJ, Burkhardt F, et al. Glycosylated RGD-containing peptides: tracer for tumor targeting and angiogenesis imaging with improved biokinetics. *J Nucl Med.* 2001;42:326–336.
- Xiong JP, Stehle T, Zhang R, et al. Crystal structure of the extracellular segment of integrin  $\alpha_v\beta_3$  in complex with an Arg-Gly-Asp ligand. *Science.* 2002;296:151–155.
- Janssen ML, Oyen WJ, Dijkgraaf I, et al. Tumor targeting with radiolabeled  $\alpha_v\beta_3$  integrin binding peptides in a nude mouse model. *Cancer Res.* 2002;62:6146–6151.
- Janssen M, Oyen WJ, Massuger LF, et al. Comparison of a monomeric and dimeric radiolabeled RGD-peptide for tumor targeting. *Cancer Biother Radiopharm.* 2002;17:641–646.
- Wong NC, Mueller BM, Barbas CF, et al. Alphav integrins mediate adhesion and migration of breast carcinoma cell lines. *Clin Exp Metastasis.* 1998;16:50–61.
- Kawatsu S, Kato T, Nagano-Saito A, Hatano K, Ito K, Ishigaki T. New insight into the analysis of  $6-[^{18}\text{F}]$ fluoro-L-DOPA PET dynamic data in brain tissue without an irreversible compartment: comparative study of the Patlak and Logan analyses. *Radiat Med.* 2003;21:47–54.